Department of Physics and Astronomy

University of Heidelberg

Master thesis

in Physics

submitted by

Jan Patrick Hammerich

born in Heidelberg

2018

Analog Characterization

and Time Resolution

of a large scale HV-MAPS Prototype

This Master thesis has been carried out by

Jan Patrick Hammerich

at the

Physikalisches Institut

under the supervision of

Prof. André Schöning

Abstract

The Mu3e experiment is planing to search for the charged lepton flavor violating decay $\mu^+ \to e^+e^-e^+$ with a branching ratio sensitivity of 2×10^{-15} in its first phase. This requires an intense muon beam and a detector which can measure the decay products precisely.
Multiple Coulomb scattering imposes strict limitations on the material budget of the detector. For the silicon pixel tracker High-Voltage Monolithic Active Pixel Sensors are chosen. This technology allows for a combination of readout electronics and depleted sensor diode in one chip, which can be thinned to a total thickness of 50 µm. In this thesis, the first large scale HV-MAPS prototype for the Mu3e experiment, the MuPix8, is characterized. The pulse shaping of the amplifier is investigated and the impact of the configuration of the circuit studied.
Three time-walk correction methods are implemented in the MuPix8. These modes are tested and compared. A time resolution of below 7 ns is achieved for the complete sensor. For a subset of pixel a resolution below 6.25 ns is measured.

Zusammenfassung

Das Mu3e Experiment plant die Suche nach dem geladenen Leptonfamilienzahl verletzenden Zerfall Mu3e mit einer Sensitivität des Verzweigungsverhältnisses von 2×10^{-15} der ersten Phase. Dies erfordert einen intensiven Myonenstrahl und einen Detektor, der den Zerfallsprodukte präzise messen kann.
Die Mehrfachstreuung setzt strenge Grenzen für das Materialbudget des Detektors. Für den Silizium-Pixel-Spurdetektor wurden Hochspannungsbetriebe-Monolithische Aktive Pixel Sensoren ausgewählt.Diese Technologie ermöglicht eine Kombination von Ausleseelektronik und verarmter Sensordiode in einem Chip, der auf eine Gesamtdicke von 50 µm gedünnt werden kann.
In dieser Arbeit ist der erste große HV-MAPS-Prototyp für das Mu3e Experiment charakterisiert. Die Pulsform des Verstärkers wird untersucht und die Auswirkungen der Konfiguration der Schaltung analysiert.
Drei *time-walk*-Korrekturverfahren sind im MuPix8 implementiert. Diese Modi werden getestet und verglichen. Eine Zeitauflösung von unter 7 ns wird für den gesamten Sensor erreicht. Für eine Teilmenge von Pixeln wird eine Auflösung unter 6.25 ns gemessen.

Für meine Großeltern

Contents

Part I

Introduction

1 Introduction

Since the advent of quantum physics, the knowledge of fundamental processes on particle level has increased significantly. What is known today as Standard Model of particle physics is a theoretical framework which describes all known particles and their interactions. Despite the precision at which the predictions derived from this model have been confirmed, many phenomena are not covered in the Standard Model like the observed matter-antimatter asymmetry in the universe, the quantum nature of gravity and dark matter. These observations have motivated many theories beyond the Standard Model, which are tested in modern particle physics experiments.
Conceptually, there are two methods of searching for new physics. The search at the energy frontier is the approach taken at large colliders like the Large Hadron Collider (LHC). The energy of the collided particles is increased to higher values to directly produce undiscovered particles at higher masses. Probing the Standard Model at the intensity frontier allows to search for the footprints of unknown particles which contribute via quantum loops. These loops induce tiny deviations from the theory prediction or allow processes otherwise forbidden or unobservable.
One of these precision experiments is the Mu3e experiment [1] which is planned to search for the charged lepton flavor violating decay $\mu^+ \to e^+e^-e^+$ with a branching ratio sensitivity of 2×10^{-15} at 90% confidence level in its first phase.
The target sensitivity of phase I requires a high rate muon beam of $1 \times 10^8 \mu/\mathrm{s}$ to measure enough muon decays in a reasonable time frame. A facility which can provide this muon rate is the High Intensity Proton Accelerator (HIPA) at the Paul Scherrer Institut (PSI) in Switzerland. The detector is composed of cylindrical stations around the beam axis with a stopping target in the center. Silicon pixel layers track the decay products bent by a magnetic field to precisely measure their momentum. Scintillating fibers and tiles add high resolution time information to improve the event reconstruction.
The maximum momentum of the particles produced in the decay of a stopped muon is kinematically limited to $< 53\,\mathrm{MeV/c}$, which is half the muon mass. This imposes strict limits on the material budget of the detector to reduce the loss of momentum resolution due to multiple Coulomb scattering.
A technology which can meet this constraint is the High Voltage Monolithic Active Pixel Sensor (HV-MAPS) technology. Fully monolithic pixel sensors have been fabricated in this technology using a commercial HV-CMOS process. A depletion zone in the range of 20 µm to 30 µm, depending on the substrate resistivity, collects charges rapidly via drift. The sensor is pixelated into $81 \times 80\,\mu\mathrm{m}^2$ cells. The inactive substrate can be thinned down to a total thickness of 50 µm. Each pixel cell has a dedicated readout cell where the hit is digitized. The process allows the integration of the readout on the same chip without additional material for a readout chip.

In this thesis the first large scale HV-MAPS prototype for the Mu3e experiment, the MuPix8, is characterized. Measurements of the pulse shape of the amplifier in the pixel and the impact of the amplifier settings on the sensor performance are investigated to validate the design of the circuit. Measurements of the time resolution are performed in the laboratory using a radioactive source and a scintillator as reference. New features to the MuPix series in the MuPix8 in the form of time-walk compensating circuits are tested and the improved resolution using these methods is presented.

2 Theory

2.1 The Standard Model of Particle Physics

The theoretical framework of particle physics is the so called Standard Model (SM). It describes the known particles and their interactions on quantum level. It breaks the multitude of particles down to twelve fermions with spin 1/2, four gauge bosons with spin 1, the Higgs boson with spin 0 and their interplay. The fundamental SM particles (Fig. 2.1) can be distinguished by quantum numbers and interactions.
The fermions and their respective antiparticles are organized in quarks who interact via the strong force and leptons who do not. Quarks are divided in three generations and two types. The up-type quarks, up (u), charm (c) and top (t), carry +2/3 elementary charges while the down-type quarks, down (d), strange (s) and bottom (b), have -1/3 elementary charge. They are the only fermions who participate in the strong interaction. Leptons are also split into three generations, electron (e), muon (μ) and tau (τ), with each generation consisting of a particle with negative electric charge and a neutrino (ν) which carries no electric charge. Neutrinos are treated as massless in the SM. Since the neutrinos are electrically neutral, they can only interact weakly while the charged leptons also couple to the electromagnetic force.
The gauge bosons are the force carriers of the SM. The massless photon (γ) mediates the electromagnetic interaction. The weak force carriers are the $W^{+/-}$-bosons with ± 1 elementary charges and $80.4\,\mathrm{GeV/c^2}$ mass and the neutral Z^0 which has a mass of $91.2\,\mathrm{GeV/c^2}$ [2]. The weak and the electromagnetic force can be unified into a single force [3].
As gravity is not included in the SM, the last remaining force is the strong interaction. It is mediated by massless gluons (g). Unlike photons who do not carry any charges, the gluon has so called color charge which is the charge of the strong force. That means gluons not only interact with quarks, which carry color charge, but also with each other. This self-interaction limits the range of the strong force to the scale of atomic nuclei and confines quarks and gluons to color neutral objects called hadrons.
With the discovery of the Higgs boson [4, 5] another missing piece could be added to the SM. The Higgs boson is the result of a spontaneous symmetry breaking in the electroweak force which gives mass to the W and Z bosons. Recent results indicate that the coupling of fermions to the Higgs could also give mass to the fermions [6, 7].
Because the SM is a quantum field theory, the eigenstates of different interactions do not have to be the same. Prime example is the W decay which violates quark flavor because the weak eigenstates are superpositions of flavor eigenstates. This relation is described by the Cabibbo-Kobayashi-Maskawa-Matrix (CKM-Matrix).

In the lepton sector flavor violation was not discovered until the observation of neutrino oscillation [8–10]. The simplest way of explaining this phenomenon is to introduce non-zero neutrino masses with mass eigenstates different from the flavor eigenstates. The analogon for the CKM mixing matrix in the neutrino sector is called Pontecorvo–Maki–Nakagawa–Sakata matrix (PMNS matrix). So far, no charged lepton flavor violation (cLFV) has been observed. Although the inclusion of neutrino oscillations allows for a way to create cLFV, the theoretical branching fractions are so small that they are beyond experimental reach [11].
While the SM has been confirmed to a stunning precision, clear evidence for new physics required to explain observations incompatible with the SM is absent. Dark matter, gravitation on quantum level and the observed matter/anti-matter asymmetry in the universe can not be explained with the help of the SM, giving rise to wide fields of theories beyond the SM.

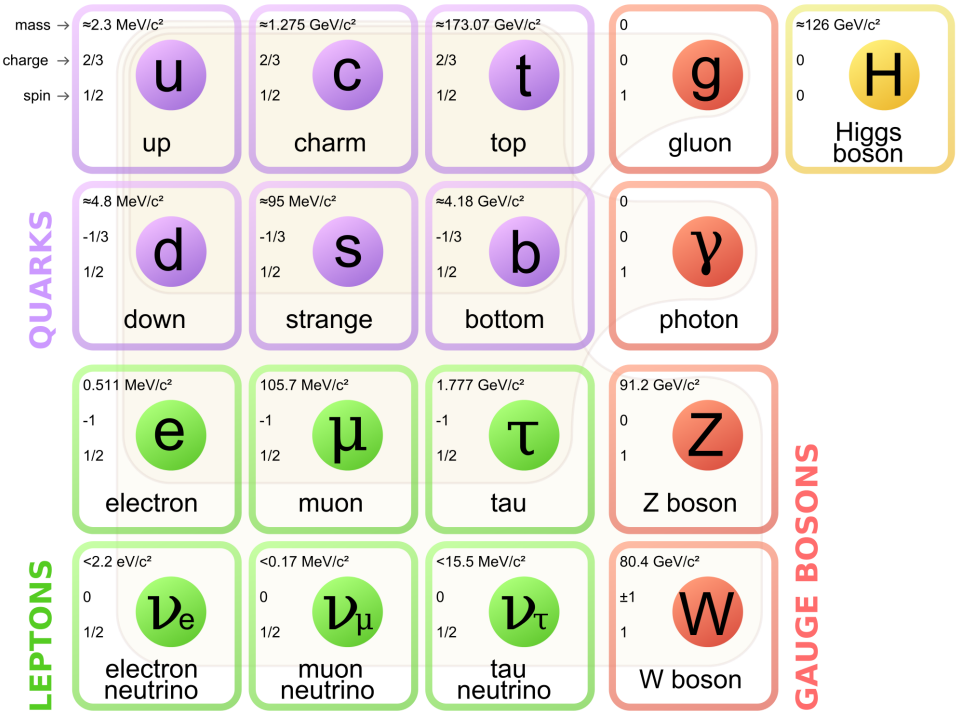

Figure 2.1: Particle content of the Standard Model of particle physics [12].

2.2 The Muon Decay

2.2.1 Standard Model Modes

In the Standard Model the muon decays at leading order via the Michel decay $\mu^- \to e^- \nu_\mu \bar{\nu}_e$, shown in Fig. 2.2. The next to leading order radiative decay $\mu^- \to \gamma e^- \nu_\mu \bar{\nu}_e$ has a branching fraction of $(3.4 \pm 0.4)\,\%$ [2]. Related to the radiative decay is the internal conversion decay $\mu^+ \to e^+ e^- e^+ \bar{\nu}_\mu \nu_e$ with a branching ratio of $(1.4 \pm 0.4) \times 10^{-5}$ [2] in which the photon converts into an electron-positron pair. In this thesis, electrons and positrons are referred to as electrons for brevity unless explicitly stated otherwise. Charge conservation is assumed.

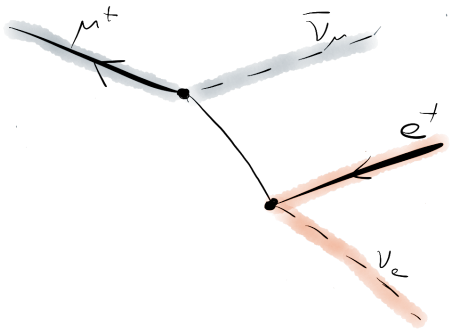

Figure 2.2: Michel decay of the muon.

Without neutrino oscillations, the decay $\mu^+ \to e^+ e^- e^+$ is forbidden since lepton flavor is conserved in the SM. With the addition of neutrino oscillations, the decay becomes possible via the loop diagram in Fig. 2.3 although the theoretical branching ratio is 2.1×10^{-55} [11] which can not be observed experimentally. The cause for this suppression is the huge mass difference between the W-boson and the mass differences of the neutrinos as the branching ratio of the decay is approximately proportional to $(\Delta m_\nu^2)^2 / m_w^4$.

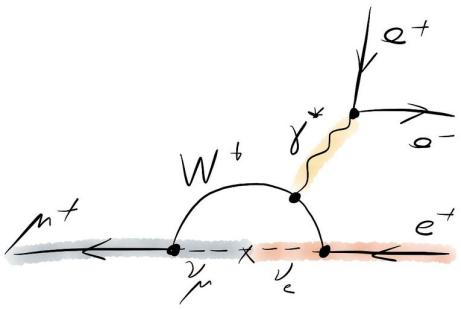

Figure 2.3: $\mu^+ \to e^+ e^- e^+$ via neutrino oscillation.

2.2.2 Beyond the Standard Model Decay Modes

Beyond the SM, a plethora of theories predict cLFV at branching ratios which are experimentally accessible. For example, $\mu \to eee$ would be possible in the Super Symmetry (SUSY) framework [13] by a quantum loop as seen in Fig. 2.4a or via heavy mediators which could violate lepton flavor like a Z′ [14] on tree level shown in Fig. 2.4b.
These theories are constrained by the experimental limits, like the $\mu \to e\gamma$ decay which has a branching ratio below 4.2×10^{-13} [15], or $\mu^+ \to e^+e^-e^+$ with a branching fraction smaller than 1.0×10^{-12} [16].
Any observation of these processes would be a clear sign of new physics beyond the Standard Model.

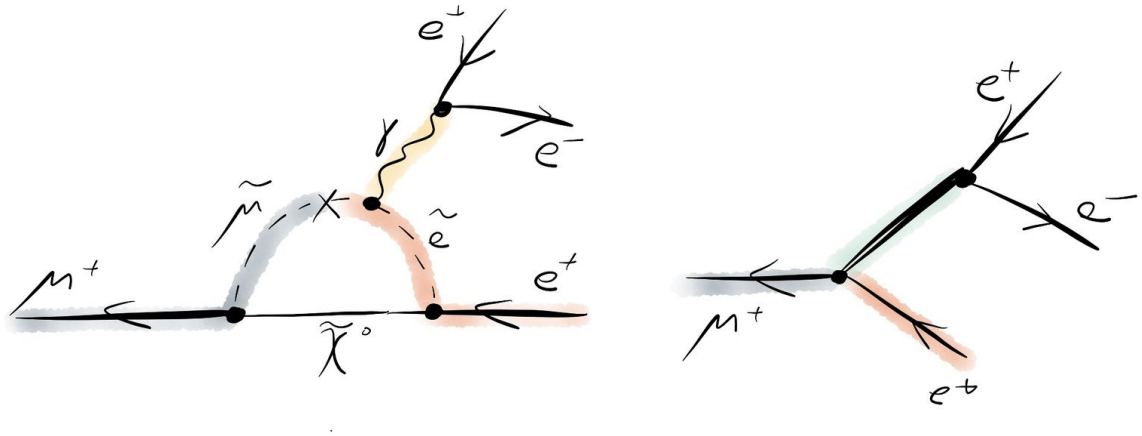

(a) Decay via SUSY particles.

(b) Decay on tree level.

Figure 2.4: $\mu \to eee$ decays beyond the Standard Model.

3 The Mu3e Experiment

The Mu3e experiment [1] plans to search for the cLFV decay $\mu^+ \to e^+e^-e^+$ with a branching ratio sensitivity of 2×10^{-15} in its first phase which is foreseen to be increased to 10^{-16} in phase II. This requires an intense muon beam to observe this many muon decays in a reasonable amount of time. The last dedicated experiment to search for this decay was the SINDRUM experiment [16] in 1988. Since then, other experiments have searched in other channels for cLFV or plan to do so with increasing precision shown in Fig. 3.1.

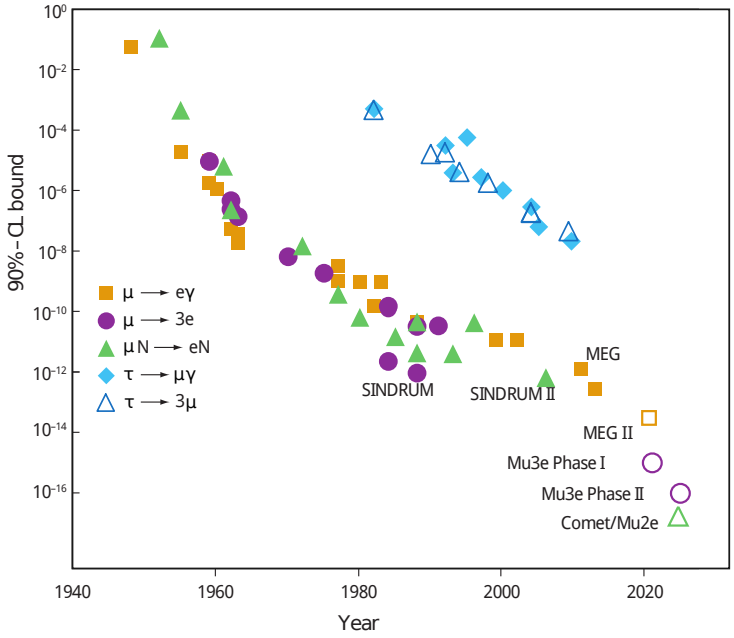

Figure 3.1: Past and planned experiments searching for cLFV and their sensitivities [17].

3.1 Signal Decay

Due to energy and momentum conservation the following relations describe the decay products in the rest frame of the muon. The index denotes the different decay products.

$$\vec{p}_{tot} = \sum_{i=1}^{3} \vec{p}_i = \vec{0} \tag{3.1a}$$

$$E_{tot} = \sum_{i=1}^{3} E_i = m_\mu c^2 \tag{3.1b}$$

Due to these constraints, the energies of the decay products are limited by half the muon mass to smaller than $53\,\mathrm{MeV/c^2}$. Since no light mediator has been found which could allow the $\mu \to eee$ process, the particle is expected to be heavier than the muon. This means the mediator is only virtual and has no free path length. For this reason, the three electrons from the decay have to originate from the same point in space-time. These constraints are used to suppress background.

3.2 Background

Background events for the $\mu^+ \to e^+e^-e^+$ process can be categorized in two groups. The irreducible physics background is given by the internal conversion decay $\mu^+ \to e^+e^-e^+\bar{\nu_\mu}\nu_e$. Due to the neutrinos carrying away momentum and energy undetected as pictured in Fig. 3.2, Eq. 3.1a & 3.1b would be violated. Limits in the detector resolution aloow internal conversion events with low momentum neutrinos to mimic a $\mu^+ \to e^+e^-e^+$ event. To suppress this background a momentum resolution of below $1\,\mathrm{MeV/c}$ is required [1].
The other source of background are accidental combinations of electrons due to the high muon beam rate. With an imperfect resolution in both time and space, electrons from different muon decays can be grouped together. Examples are shown in Fig. 3.3a where two positrons from muon decays and an electron from Bhabha scattering in the detector material can mimic a $\mu^+ \to e^+e^-e^+$ signal. Likewise, internal conversion decays can contribute if, as shown in Fig. 3.3b, one of the positrons has too little momentum to be detected and the other decay products are grouped with a positron from another muon decay. This background is reduced by the detector resolution.

Figure 3.2: Internal conversion decay of the muon.

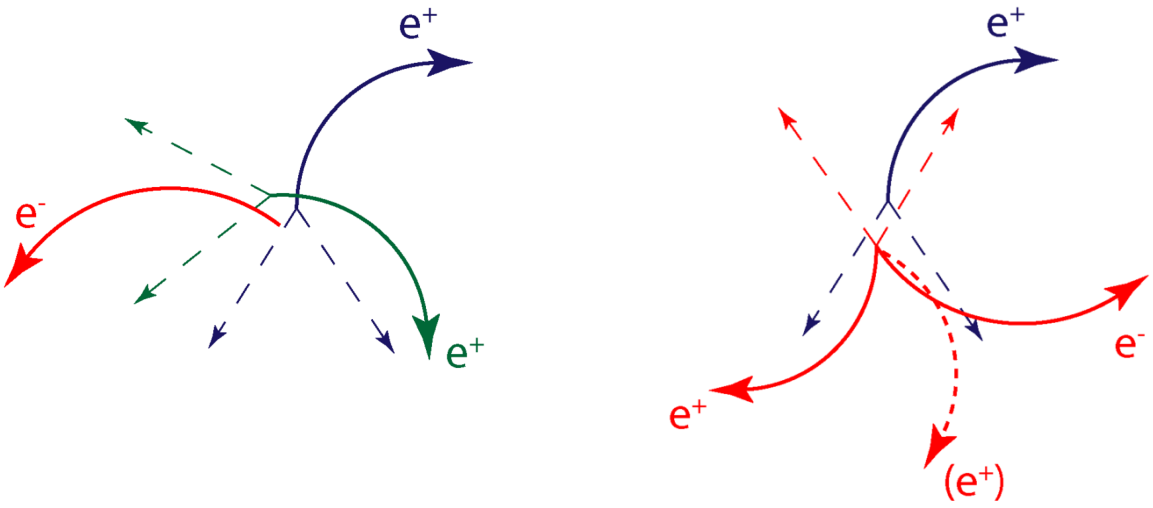

(a) Accidental background from Bhabha scattering.

(b) Accidental background from internal conversion.

Figure 3.3: Accidental backgrounds.

3.3 The Mu3e Detector

The Mu3e detector [18] for phase I consists of a central barrel in which a hollow double cone target stops the muons of a high intensity beam. An additional barrel is placed upstream and downstream of the target. Because the muons decay at rest, the rest frame of the muon is identical to the lab frame so the relations Eq. 3.1a & 3.1b can be applied without the need to transform coordinate systems. Thin silicon pixel sensors fabricated in the HV-MAPS technology form the core of the detector. These sensors are mounted on polyimide foil with aluminum traces for power and signal transmission. Scintillating fibers add an additional time measurement to reduce combinatorics. The experiment is placed in a 1 T magnetic field which bends the decay products to allow momentum measurement and discrimination between positrons and electrons. Due to the low momentum of the decay products, the bending radius is small enough that particles return to the detector so that they can be measured again which increases the momentum resolution. Multiple Coulomb scattering is canceled at first order after one half turn.
If the particles have enough momentum along the beam axis, they reenter the upstream or downstream stations called "recurl stations", where they are again measured by pixel tracking layers and scintillating tiles for a high precision timing measurement. The active detector components are cooled by a gaseous helium flow to reduce multiple Coulomb scattering at sufficient cooling capability. The material budget is foreseen to be 0.1 % radiation lengths per silicon tracking layer and around 0.3 % radiation lengths for the fiber layer.
The only currently available beam line which fulfills the required rate of $1 \times 10^8 \mu^+/s$ is the Compact Muon Beamline (CMBL) [19] at the Paul Scherrer Institut in Switzerland. The beam is produced by colliding the intense beam of the HIPA [20] with a carbon target from which 28 MeV/c surface muons are extracted to the beam line.

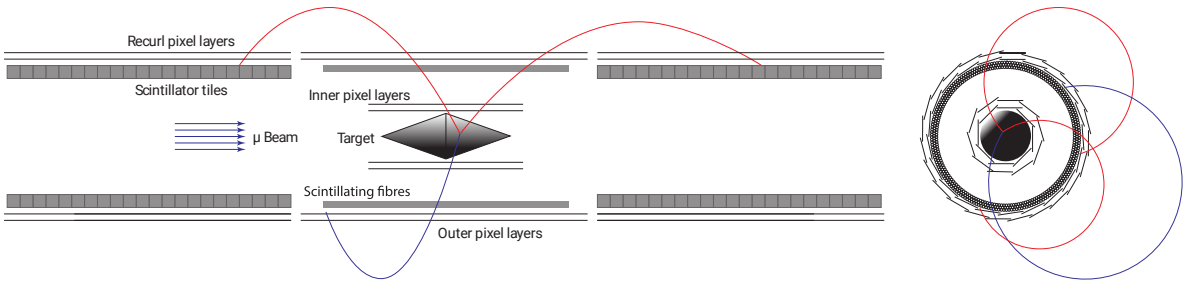

Figure 3.4: The Mu3e detector in longitudinal and transverse view with a $\mu \to eee$ event.

4 Particle Detection

Various vastly different approaches have been made to measure the properties of elementary particles. Due to their quantum nature, an interaction with the detector material is required to deduce their properties. This in turn influences the measured particle which enforces a balance of precision of the measurement and interference with the particle. In the simplest distinction, particle detectors can be categorized in timing detectors, tracking detectors and calorimeters.
Calorimeters, measure the energy of a particle by stopping the particle and observing the energy deposition in the material. This allows for high energy resolution but comes at the loss of the particle. Tracking detectors are very granular instruments which measure traversing particles. In a magnetic field, the combination of multiple points is used to determine the curvature due to the bending radius and with this, the momentum of the particle. For this approach limited interaction with the particle is key as disturbances of the path decrease the precision of the measurement. Timing detectors are very fast sensors which allow separation of particles and the measurement of the particle time of flight.
The knowledge of these behaviors is vital in constructing and operating any particle physics experiment.

4.1 Interaction of Charged Particles with Matter

Particles which carry an electric charge interact with the atoms of the detector material via the electromagnetic force. This means that the interaction is dependent on the charge z of the incident particle. Since only leptons are measured in the Mu3e experiment strong interactions are neglected and not discussed here.

4.1.1 Heavy Particles

The term "heavy particle" is usually used for all particles which are heavier than electrons. For those particles, energy loss via ionization is the significant contribution over many orders of magnitude in energy. The Bethe-Bloch-formula [21] in Eq. 4.1 describes the mean energy loss $\left\langle \frac{dE}{dx} \right\rangle$ of a particle due to ionization when traversing a material.

$$-\left\langle \frac{dE}{dx} \right\rangle = \frac{4\pi n z^2}{m_e c^2 \beta^2} \left(\frac{e^2}{4\pi\epsilon_0} \right)^2 \left[\log\left(\frac{2 m_e c^2 \beta^2}{I(1-\beta^2)} \right) - \beta^2 - \frac{\delta(\beta\gamma)}{2} \right] \tag{4.1}$$

It is parametrized by the relative velocity of the particle $\beta = \frac{v}{c}$, the charge of the particle z, the density-effect correction $\delta(\beta\gamma)$, the electron density n and the mean excitation energy I of the material. Constants are electron mass m_e, the vacuum speed of light c and the vacuum permittivity ϵ_0. The shape of the function for different materials is shown in Fig. 4.1. Characteristic is the minimum at around $\beta\gamma = \frac{p}{mc} \approx 3$ at which all particles lose the least amount of energy. Particles in this region are called Minimum Ionizing Particles (MIP). For lower momenta, the interaction time increases drastically which causes an increased loss roughly proportional to β^{-2}. For higher momenta, relativistic effects become more significant which cause the electric field to compress along the longitudinal direction. This density-effect suppresses the logarithmic rise at higher momenta.
Eq. 4.1 only considers the mean energy loss. In practice, the energy deposition can vary over a large range due to statistical fluctuations. Events where a large amount of energy is transferred, electrons can be knocked out of the material, so called δ-electrons. The distribution of the energy loss given a specific particle, momentum and material is often approximated by a Landau function.

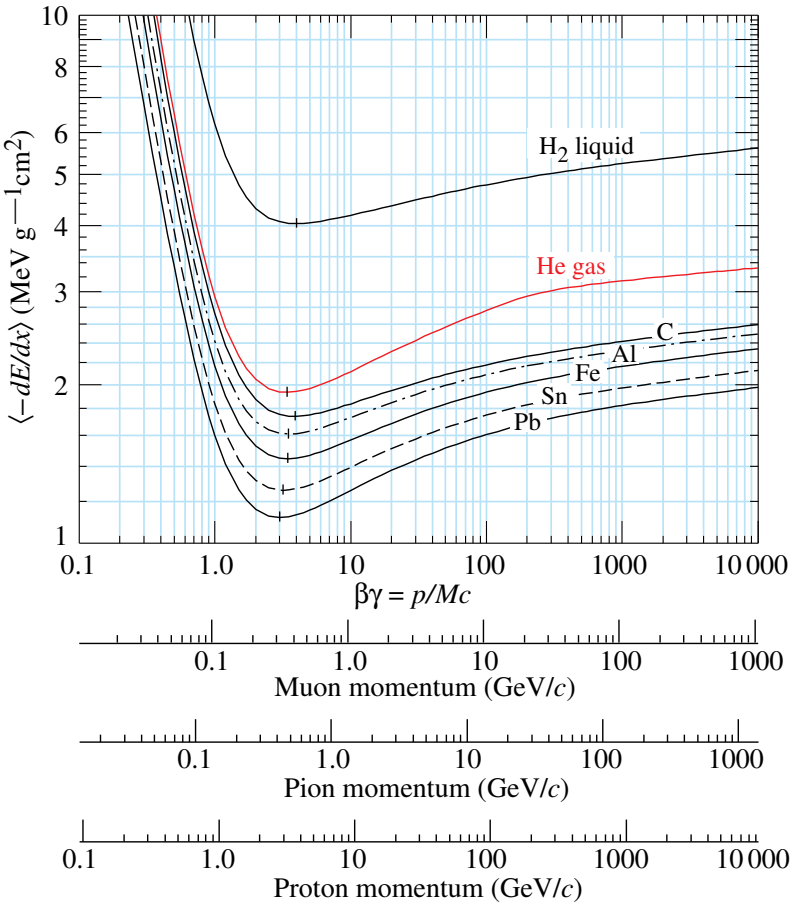

Figure 4.1: Mean energy loss of heavy particles described by the Bethe-Bloch formula for different materials and particle species [2].

4.2 Electrons and Positrons

Electrons and positrons have to be described separately for two reasons. First, they are much lighter than all other known charged particles which causes an increased bremstrahlung contribution to the energy loss at low momenta. Second, the detector material itself contains electrons. Quantum effects like annihilation for positrons and repulsion due to the electrons of the material and the incident electrons being indistinguishable require a dedicated treatment. These considerations lead to the Berger-Seltzer-formula Eq. 4.2 [22], which describes the mean energy loss for electrons and positrons through ionization. The parameters for this equation are the momentum dependent stopping power $B_0(T)$ of the material, the density correction δ for electrons or positrons, the mean excitation energy I of the material, the ratio of protons to nucleons of the material $\frac{Z}{A}$ and the material density ρ. As example, the energy loss for electrons and positrons in silicon is drawn in Fig. 4.2 where the repulsion due to the Pauli principle induces a higher energy loss for electrons.

$$-\left\langle \frac{dE}{dx} \right\rangle = \rho \frac{0.153536}{\beta^2} \frac{Z}{A} \left(B_0(T) - 2\log(\frac{I}{m_e c^2}) - \delta \right) \tag{4.2}$$

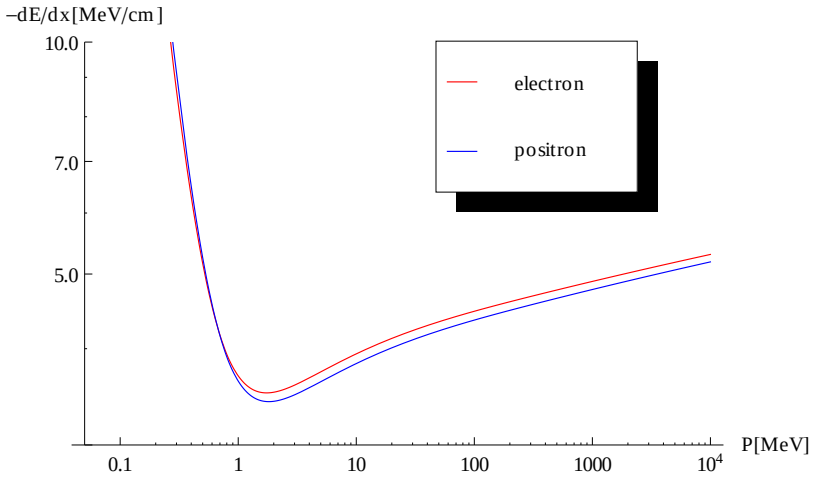

Figure 4.2: Mean energy loss of electrons and positrons in silicon for 50 keV to 10 GeV. Taken from [23] and drawn using data from [22].

4.3 Bremsstrahlung

Bremsstrahlung describes the phenomenon of energy loss by the emission of free photons instead of photon exchange by ionization. If the charged particles are highly relativistic ($\beta \approx 1$) and their momentum is above 10 MeV/c, the energy loss due to bremsstrahlung is given by Eq. 4.3 [2] which depends on the radiation length X_0 of the material. The radiation length of a material can be calculated according to Eq. 4.4 [2] which only depends on the number of protons Z and the density ρ of the material.

$$-\frac{dE}{dx} = -\frac{E}{X_0} \tag{4.3}$$

$$X_0 = \frac{716.4 \cdot A}{Z(Z+1) \cdot \log(287/\sqrt{Z})} \frac{1}{\rho} \tag{4.4}$$

4.4 Multiple Coulomb Scattering

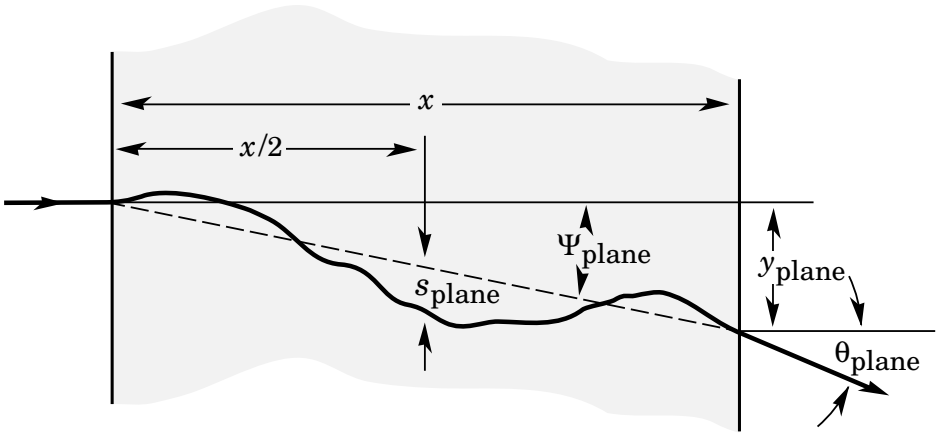

Figure 4.3: Drawing of a particle entering a material and scattering multiple times [2].

Traversing matter does not only cause energy loss via ionization but also a deflection of the path of the particle. Charged particles will scatter off the Coulomb fields of the detector nuclei multiple times which produces an offset and an angle to the undisturbed path as shown in Fig. 4.3. For very thin detector layers the offset can be neglected but the angular scatting component remains. The central 98% of the angular distribution can be described by a Gaussian approximation with an RMS according to the Highland equation in Eq. 4.5 [2].

$$\Theta_{rms} = \frac{13.6\,\text{MeV}}{\beta cp}\, z\sqrt{\frac{x}{X_0}}\left[1 + 0.038\log\Big(\frac{x}{X_0}\Big)\right] \tag{4.5}$$

This formula shows a dependence on both the momentum p and the velocity βc of the particles which is important for the Mu3e experiment. Due to the fixed charge z of the electrons, the only parameter left is the radiation length x. To achieve a good momentum resolution the multiple scattering angle has to be as small as possible which imposes tight constraints on the material budget.

4.5 Scintillation Light

Scintillation light is caused by the excitation of material electrons to higher shells. The deexcitation releases photons which can be observed. To reduce the self-absorption of these photons in the material, inorganic scintillators are doped with other atoms or small molecules which emit light the bulk material is transparent to. Organic scintillators consist of special molecules which deexcite such that the radiation can not excite the other molecules. The excited states of organic scintillators usually have very short mean life times, making them ideal tools for timing measurements.

5 Semiconductor Physics

5.1 Semiconductors

Semiconductors can be defined as material in which all electron states in the valence band, the highest occupied band, are occupied at temperature $T = 0\,\mathrm{K}$. The conduction band above the valence band is empty and the material is insulating. For semiconductors the gap between both bands is small so that above absolute zero temperature, electrons can be thermally excited into the conduction band leaving behind a positive charged ion. The transfer from electrons of a neutral atom to a neighboring ion acts as positive space charge called "hole". Conduction band electrons moving to an ion can recombine into a neutral lattice atom.

5.2 Silicon

Like carbon, silicon has 4 valence electrons forming a covalent bond with its neighboring atoms which results in a diamond lattice. Silicon is the most common semiconductor and is employed in a large variety of applications. The size of the gap between the conduction and the valence band allows to operate silicon devices at room temperature unlike germanium devices for example.
Important silicon properties are listed in the appendix in Tab. A.1.

5.3 Doping

Comparing the intrinsic charge carrier density to the atomic density, pure silicon acts like an insulator. The number of free charges can be increased by introducing impurities to the lattice which is called doping. Donors, elements like phosphorous with 5 valence electrons, release one of their electrons in the conduction band, leaving behind a localized charge, while acceptors like boron capture one of the valence electrons of a neighboring silicon atom which creates a hole. Implanting elements which release positive charge carriers is called p-doping, while adding elements which contribute negative charge carriers is called n-doping.

5.4 p-n-junction Diode

If a p-doped and an n-doped material are brought into contact, the junction acts as a diode. Positive charges will diffuse into the n-doped region while electrons diffuse into the p-doped bulk. Equilibrium is reached when drift induced by the field from the immobile ions of the dopants and diffusion cancel out which is pictured in Fig. 5.1.
The region free of free charge carriers between the doping regions is called depletion zone. An external voltage between the different doping regions allows to manipulate the width of this region due to the change in the drift field.
The width of the depletion zone w is given by Eq. 5.1 [24], where ϵ is the dielectric constant of silicon, $U - U_0$ the bias voltage minus the build-in voltage of the diode and N_i the density of donators or acceptors.

$$w = \sqrt{\frac{2\epsilon_0\epsilon(U - U_0)}{e}\frac{N_A + N_D}{N_A N_D}} \tag{5.1}$$

In the case of $U \gg U_0$ and $N_D \gg N_A$ the equation simplifies to Eq. 5.2.

$$w = \sqrt{\frac{2\epsilon_0\epsilon U}{eN_A}} \tag{5.2}$$

For the capacitance, the depletion zone can be approximated by a parallel plate capacitor and is then given by the area of the interface A divided by the depletion width, described in Eq. 5.3.

$$C = \frac{A\epsilon_0\epsilon}{w} = A\sqrt{\frac{eN_A\epsilon_0\epsilon}{2U}} \tag{5.3}$$

Replacing the acceptor density with the resistivity ρ in Eq. 5.4, where μ_p is the hole mobility in silicon, the depletion width is then given by Eq. 5.5 and the capacitance by Eq. 5.6.

$$\rho = \frac{1}{eN_A\mu_p} \quad N_A = \frac{1}{e\rho\mu_p} \tag{5.4}$$

$$w = \sqrt{2\epsilon_0\epsilon U\rho\mu_p} \tag{5.5}$$

$$C = A\sqrt{\frac{\epsilon_0\epsilon}{2U\rho\mu_p}} \tag{5.6}$$

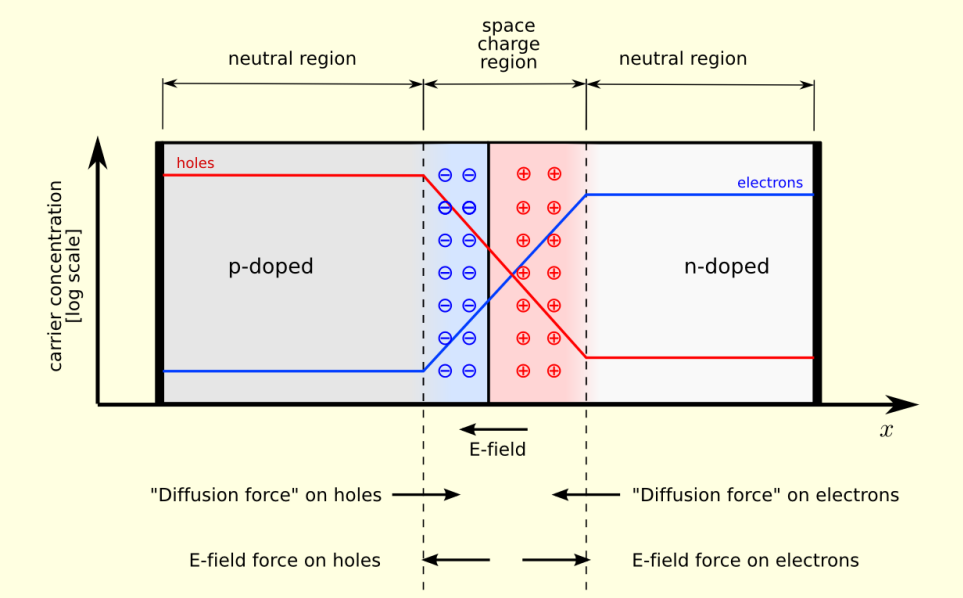

Figure 5.1: Illustration of the p-n-junction equilibrium from [25].

5.5 Signal Generation & Charge Collection

When a charged particle passes through material, it deposits energy via ionization as discussed in Sec. 4.1. In a semiconductor this energy transfer causes the formation of electron-hole pairs. If these pairs are created in a depletion zone, they are drifted to the electrodes due to the electric field. The drift velocity is given in Eq. 5.7 and only depends on the mobility of the charge carriers in the substrate and the electric field. The electrons and holes travel in opposite directions which creates a dipole moment. This dipole moment induces a current that can be measured as signal at the electrodes. A diffusion component is also remaining but can be neglected because it is much slower than the drift contribution. The smallness of the depletion zone for the characterized sensors also reduces the impact of diffusion orthogonal to the drift field.
Photons can also produce charges in the semiconductor, either via the photo-electric effect or by Compton scattering. In both cases a primary electron with enough energy is produced such that it can produce more secondary electron-hole pairs.

$$\vec{v}_{drift} = \vec{E} \times \mu_{p/e} \times Q_{p/e} \tag{5.7}$$

6 Semiconductor Detectors

6.1 Pixel Sensors

In an age of mobile communication devices, silicon pixel sensors are common place. They can not only be used for the detection of light as imaging sensors in cameras do but can also detect charged particles. Large particle physics experiments like ATLAS or CMS have silicon pixel trackers as core systems. These experiments use hybrid pixel sensors which are composed of a sensor chip, consisting of segmented diodes, and a readout chip. Each sensor diode is connected to a readout channel with a solder ball in a process called bump bonding. While this concept has a good performance, it is very expensive as the bump bonding process requires very high precision and many fabrication steps. The solder balls also consist of various heavy metals with have short radiation lengths which lead to increased multiple scattering.

6.1.1 Monolithic Active Pixel Sensors

Monolithic Active Pixel Sensors (MAPS) are an advancement of the Active Pixel Senors (APS) first developed for imaging applications. APS only have an amplification circuit integrated in the pixel. MAPS have the complete readout implemented on the chip. MAPS typically do collect charge via diffusion and not via drift. To achieve sufficient charge collection, a deep epitaxial layer forms a potential barrier with the substrate and the doping wells on top, confining the diffusion into the direction of the electrodes. This allows for a large fill factor and a low thickness as the majority of the substrate is inactive and can be thinned away. A recent example of this technology is the ALPIDE chip [26] which will be used in the upgrade of the ALICE inner tracking system. The charge collection by diffusion comes at the price of time resolution as diffusion has charge collection times in the order of µs while drift takes place in the order of ns.

6.1.2 High Voltage Monolithic Active Pixel Sensors

High-Voltage Monolithic Active Pixel Sensors (HV-MAPS) [27] merge the monolithic architecture of MAPS with the fast charge collection via drift. The concept is shown in Fig. 6.1. The contact of deep n-well in a p-substrate forms a diode while the pixel electronics can be safely implemented in the n-well. A commercial HV-CMOS process allows designs for high reverse bias voltages for the substrate to create a sufficiently large depletion zone. For example with a substrate resistivity of 80 Ω cm and an HV of 60 V, the depletion zone should be roughly 23 µm thick according to Eq. 5.5. This again allows to thin the chips to thicknesses of 50 µm.
This technology was chosen for the Mu3e experiment as it allows fast charge collection to cope with the high muon decay rate and low material budget. The HV-MAPS prototypes for Mu3e are called MuPix sensors.

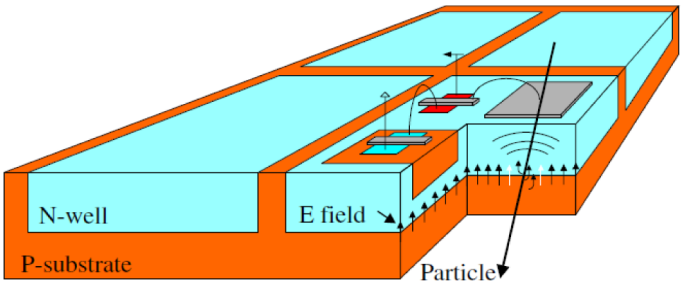

Figure 6.1: HV-MAPS concept [27].

6.2 Signal Shaping

Due to the low number of charges generated by the traversing particle, the signal has to be amplified before it can be digitized. In the case of the MuPix chips a charge sensitive amplifier is implemented in the pixel diode. Simplified, an amplifier can be treated as an CR-RC band-pass filter in his frequency behavior. Assuming a charge collection time much faster than the shaping time constants τ the output can be described with Eq. 6.1 [24], with U_0 as the input voltage.
More advanced amplification schemes include feedback loops, most commonly resistive or capacitive, which influence the shaping. For example resistive feedback smooths out the falling edge of the pulse while capacitive feedback increases steepness of the rising edge.

$$U(t) = U_0 \frac{\tau_{CR}}{\tau_{CR} - \tau_{RC}} \left(exp(\frac{-t}{\tau_{CR}}) - exp(\frac{-t}{\tau_{RC}}) \right) \tag{6.1}$$

6.3 Time-Walk

To decide if a signal is a hit or not, comparator circuits are usually employed. They compare a fixed input voltage called threshold with the output of the amplifier. The comparator output is the logic output of the comparison. Considering Eq. 6.1, it is clear that for smaller amounts of charge (U_0), the threshold will be passed later. This effect is called time-walk. A conceptual drawing can be found in Fig. 6.2 where Δt is the difference in time due to the difference in amplitude. If a better time resolution is desired, the impact of the time-walk has to be reduced. A simple handle on the delay due to time-walk is the Time-over-Threshold (ToT). Smaller pulses will also pass the threshold for a shorter time leading to a shorter ToT while large pulses have a long ToT. This dependence of latency to ToT can be used to reduce the time-walk.

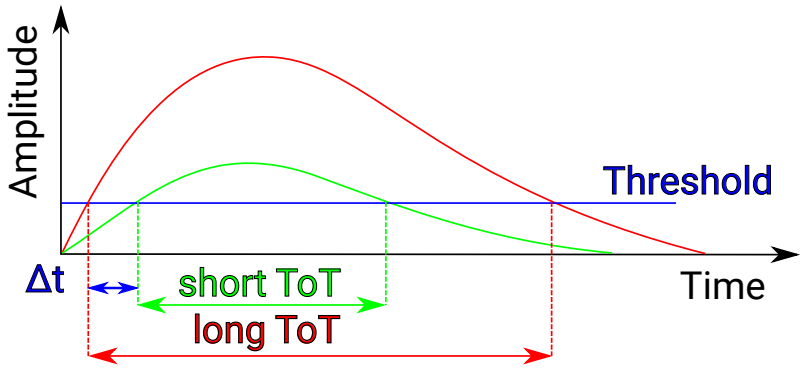

Figure 6.2: Concept of time-walk.

6.4 Silicon Photomultipliers

Silicon Photomultipliers (SiPM) are diode sensors used for light detection. A SiPM consists of a pixel diode with a quenching resistor in series. The diode is reverse biased above the breakdown voltage. If a photon creates electron-hole pairs in the depletion zone, an avalanche of charges is produced by the critical field. This current causes a voltage drop over the quenching resistor, reducing the diode bias below critical fields and stopping the avalance. Multiple diode-resistor pairs in parallel are called Multi-Pixel Photon Counter (MPPC). The pulse height is then proportional to the number of pixels hit.
SiPMs have sharp pulses that achieve below 100 ps time resolution. Unlike classical photomultiplier tubes, SiPMs can also be operated in magnetic fields. They are highly granular and only require operation voltages in the order of 50 V to 80 V.
In this thesis, a system composed of a scintillator and a SiPM is used as time reference.

Part II

Setup

7 Setup

7.1 The MuPix8

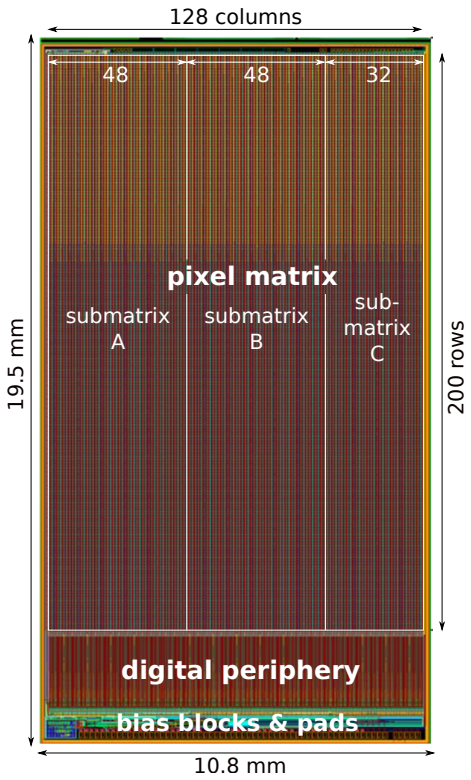

Figure 7.1: Layout of the MuPix8 prototype.

The MuPix chips are a series of HV-MAPS sensor prototypes for the Mu3e experiment. The MuPix8 (Fig. 7.1) is the first large scale prototype of the MuPix series with a chip size of $10.8 \times 19.5\,\mathrm{mm}^2$. Previous prototypes like the MuPix7 [28–32], with a size of $3.8 \times 4.1\,\mathrm{mm}^2$, were only small prototypes.
The MuPix8 combines all features required for the experiment in one chip This description is based on Ref. [33]. 128×200 sensitive pixel with a size of $81 \times 80\,\mu\mathrm{m}^2$ each are individually read out by corresponding digital cells in the periphery via a point-to-point connection. Three on-chip state machines, as seen in Fig 7.2, readout the digitized signals. The zero suppressed digital information is then serialized and sent out via four 1.25 Gbit/s Low-Voltage Differential Signaling (LVDS) links.

The chip is divided into three sub-matrices (A,B,C) along the column axis as seen in Fig. 7.1. Each of the sub-matrices has its own state machine and LVDS link. The 4th link (D) can be configured to be either a copy of one of the other 3 sub-matrices or a multiplex of all three.
The MuPix8 can generate all necessary reference voltages, the thresholds and baselines on-chip via dedicated voltage Digital to Analog Converters (DACs). To ensure a reliable operation of the chip with the correct references, these voltages are additionally supplied from outside.

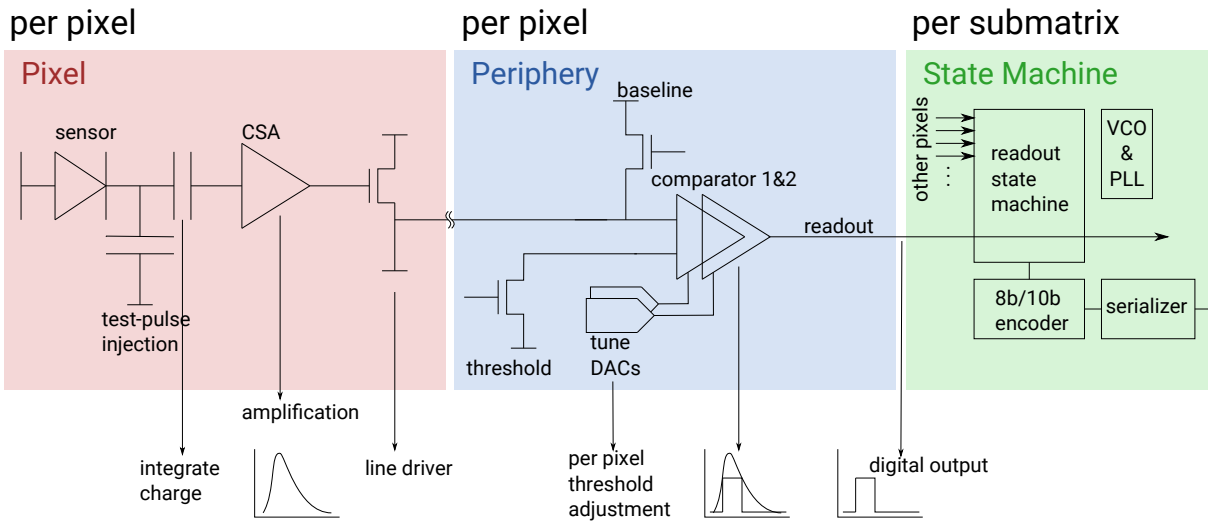

Figure 7.2: Schematic of the MuPix8 readout concept [34].

7.1.1 Analog Cell

The analog cell (Fig. 7.3) of the MuPix8 consists of a deep n-well which contains the pixel electronics. This n-well is implemented in a p-substrate such that the interface diode can be used as sensor diode while the logic inside is unaffected by the diode potential, so called "floating logic". The potentials of the p-substrate (called "substrate") and the logic in the pixel (VDDA and GNDA) are applied externally. The n-well has a dedicated circuit controlling the n-well potential and allows the amplification of the charge collected in the sensor diode.
The signal induced in the depletion zone of the sensor diode is collected at the feedback capacity C_{FB} and amplified by a Charge Sensitive Amplifier (CSA). To discharge the capacity, a resistive feedback is also implemented. A Source Follower (SF) stabilizes the feedback loop.

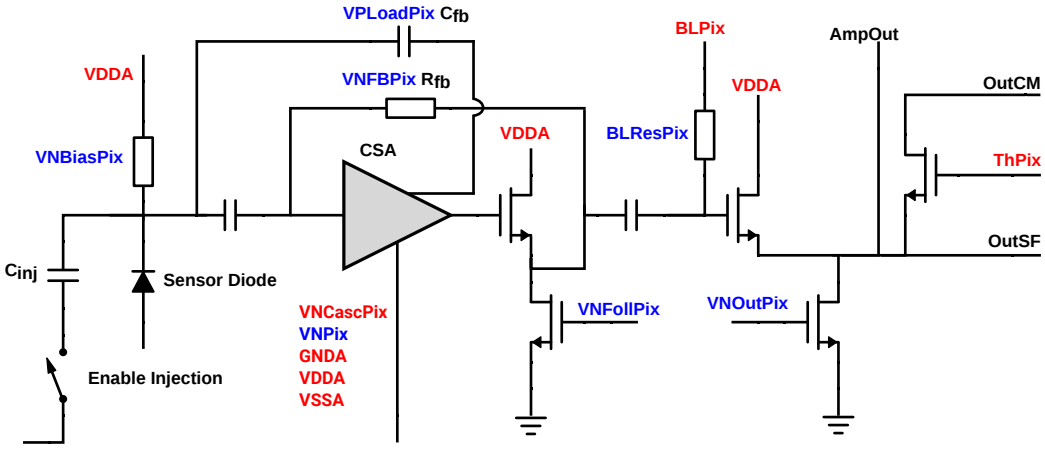

Figure 7.3: Schematic of the MuPix8 analog cell. Blue names indicate DACs, red indicate internal voltages. In matrix A OutSF is connected to the transmission line, for Matrix B and C OutCM is used.

The amplified signal is capacitively coupled to the baseline BLPix, which removes the DC component of the signal and, together with the baseline restoration, acts as a high pass. This AC signal is then driven to the digital cell by another source follower. The transmission mode depends on the submatrix of the chip. For matrix A, it is a SF which transmits a voltage signal. In matrix B & C, a Current Mode (CM) transmission is used. For this mode, the voltage ThPix acts as bias.
To test the behavior of the electronics, a test pulse can be injected. Each pixel has an injection capacity which can be charged by an external voltage. If the voltage is released, the capacitor discharges into the amplifier circuit. The injection can be enabled by the logical AND of a row and a column enable register. This allows for injections in to arbitrary single pixels or patterns allowed by the enable registers. As additional test feature, the amplifier output (AmpOut) of any pixel in column 0 can be multiplexed out to a pad on the chip. To drive this signal, an additional source follower driver is used (VPFoll). The pixel for the AmpOut can be set by a register. The AmpOut is a current signal, so it has to be terminated externally.
Most of the parameters of the amplifier and transmission circuit can be set by DACs or reference voltages. A list of all the bias voltages in the analog cell can be found in Tab. 7.1.

Bias Voltage	Source	Function	Effect
VNPix	DAC	Current Source	Current source for the amplifier
VCascPix	Internal (Fixed)	Voltage Divider	Amplifier cascode voltage
VPLoadPix	DAC	Capacitor	Feedback capacity C_{FB} and amplifier load
VNFBPix	DAC	Resistor	Resistive feedback
VNFollPix	DAC	Source Follower	Current source to stabilize the feedback
VNBiasPix	DAC	Resistor	n-well bias restoration
BLPix	Internal/External	Reference Voltage	Baseline for signal transmission (0.8 V)
BLResPix	DAC	Resistor	Baseline restoration
VNOutPix	DAC	Current Source	Current source for signal transmission
ThPix	Internal/External	Reference Voltage	Bias for current mode transmission

Table 7.1: Bias voltages for the analog cell

7.1.2 Digital Cell

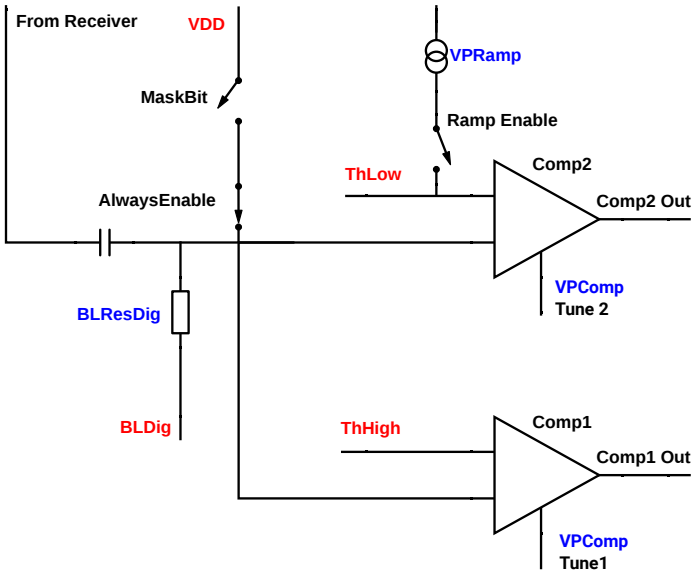

Figure 7.4: Schematic of the MuPix8 digital cell. Blue names indicate DACs, red indicate internal voltages.

The digital cell (Fig. 7.4) receives the signal from the analog cell and digitizes the signal. For the SF matrix no receiver is necessary. The CM matrices use a receiver cell to convert the current signal into a voltage signal. The received signal is then coupled capacitive to another baseline, BLDig, as reference for the comparators Comp1 and Comp2. The comparators convert the voltage signal into a logic signal which raise the hit flag and store the timestamp if the signal amplitude is higher than the threshold. The comparator signals are active low, which means that the higher voltage level corresponds to a logic 0 and the lower level to a logic 1. This logic signal is then latched by an edge detector which signals the readout that a hit has occurred.
To improve the time resolution of the MuPix8, the comparators can be used in different ways to reduce the time-walk of the signals or to correct for it, so called Time-Walk Correction (TWC). For this reason, the digital cell saves two timestamps, timestamp1 (TS1 or just TS) with 10 bits and timestamp2 (TS2) with 6 bits. The speed of each timestamp can be controlled by clock dividers from the base timestamp clock, ckdivend for the timestamp 1 and ckdivend2 for timestamp 2. The on-chip timestamps are represented in Gray code [35]. In Gray code only one bit switches per increment which reduces the power consumption. It also prevents ambiguities if a hit would happen at time of the bit transition.

As both timestamps are derived from the same base clock, the ToT is not TS2 but the difference between TS2 and TS1. The base clock of the MuPix8 is 125 MHz and ToTs can be of the order of several µs so that the speed of TS2 should be slower than the speed of TS1. To avoid ambiguities the clock dividers should set such that each TS2 bit has a corresponding bit in TS1 with the same speed. These values are derived by Eq. 7.1. Since a reduced speed of TS1 reduces the time resolution, ckdivend should be always 0, which allows only the following ckdivend2 values : 0,1,3,7,15. The ToT can than be calculated by using Eq. 7.2.

$$\log_2\left(\frac{ckdivend2+1}{ckdivend+1}\right) \in \mathbb{N}_0 \tag{7.1}$$

$$ToT = TS2 - TS1 \times \frac{ckdivend+1}{ckdivend2+1} \tag{7.2}$$

To take pixel to pixel variations into account, each digital cell has its own 6 bit RAM. 3 bits are used to individually adjust ThHigh and 2 bits for adjusting ThLow. This individual adjustment is called tuning. The range of the tuning is given by a global DAC. The last bit in the pixel RAM is the mask bit. If a pixel is too noisy to tune, its output can be switched off by this bit. A global enable bit can override all pixel masking. In the MuPix8, the masking is not implemented as logic gate but instead as analog circuit. Is the mask bit is set and not overwritten, the baseline in the digital cell is pulled up to its supply voltage VDD. That causes the comparator inputs to be always larger than the thresholds, so that the outputs are always active. The hit flag is set by an edge detector which would then never trigger.
Like in previous MuPix prototypes, a feature called hitbus is implemented. The hitbus is the comparator output of a chosen pixel. For the MuPix8, the hitbus is only available for Comp2 and not for Comp1, which means that the output that triggers the hit latch can not be accessed. It can only be set column-wise by a register and not in the row dimension. The output is the logical OR of the outputs of Comp2 of each pixel in the column. Is a pixel in that column masked, the output of that comparator is active, so the hitbus is also always active for this column.
The bias voltages for the digital cell are listed in Tab. 7.2.
During testing of the MuPix8, the line supplying the digital cell with power showed to be too thin which causes a voltage drop inside the digital matrix and limited power in the digital cell. This effect can be noticed for example in the VDDRAM level, necessary to write the pixel RAM cells. For previous prototypes this voltage could be set to 1.8 V which was the supply voltage level. In the MuPix8 this level has to be set lower than the supply voltage to write the pixel RAM correct. To compensate for the voltage drop the voltages for VDD and VDDA are chosen to be 1.9 V.

Bias Voltage	Source	Function	Effect
VPComp	DAC	Current Source	Current source for the comparators
BLDig	Internal/External	Reference Voltage	Baseline for the comparators (0.5 V)
BLResDig	DAC	Resistor	Baseline restoration
ThHigh	Internal/External	Reference Voltage	Threshold Comp1
ThLow	Internal/External	Reference Voltage	Threshold Comp2
VDel	DAC	Current Source	Current for the edge detector
VPDAC	Internal/External	Reference Voltage	Reference for tuning
VPRamp	DAC	Current Source	Ramp slope
VNRegCasc	DAC	Current Source	Receiver current mode
VPRegCasc	DAC	Current Source	Receiver current mode
VDDRAM	External	Reference Voltage	High level for pixel RAM cells

Table 7.2: Bias voltages for the digital cell

7.1.3 Time-Walk Corection Methods

Three different modes of TWC can be used in the MuPix8. As mentioned in Sec. 7.1.2, the comparator outputs are active low. The TWC modes are described by the way, the comparator outputs are interpreted by the logic.
The first mode, the Time-over-Threshold (ToT) mode, sets both thresholds to the same value. The timestamp and the hit latch are set by Comp1. Timestamp 2 is latched by the rising edge of Comp2. The ToT can than be calculated according to Eq. 7.2. For this feature no second comparator would be required in a different implementation.
The 2 Threshold mode (2Thr) uses Comp2 to latch both timestamps. The hit flag however is set by Comp1 as seen in Fig. 7.5a. This allows to set the threshold of Comp2 closer to the baseline as noise, which might pass this threshold, doesn't pass the threshold of Comp1. For this reason, the threshold of Comp1 is named Threshold High (ThHigh) and the threshold of Comp2 is labeled Threshold Low (ThLow). The closer ThLow is to the baseline, the less effect time-walk has on TS1. TS2 can still be used to improve the resolution even further. In this case the ToT only depends on ThLow.
The third mode is called Ramp mode. Here, the timestamp and the hit flag are again latched by Comp1. TS2 is latched by Comp2. The crossing of ThHigh triggers an internal signal which adds a constant current to ThLow, which results in a linear rising threshold. The crossing of this dynamic threshold than latches TS2 as seen in Fig. 7.5b. For this setup, TS2 is latched by the rising edge instead of the falling one. The dynamic threshold effectively cuts the pulse at an angle. The noise component should be reduced depending on this angle since the noise spectrum is expected to be symmetrical around the baseline. The TS2 information in this mode is also referred to as ToT. The ToT in this mode is shorter and should be less distorted by noise.

Calculations on the ToT and Ramp methods can be found in [32]. The dependence of the timestamps on the TWC mode is summarized in Tab. 7.3. The hit flag is always raised by Comp1 regardless of the TWC mode.

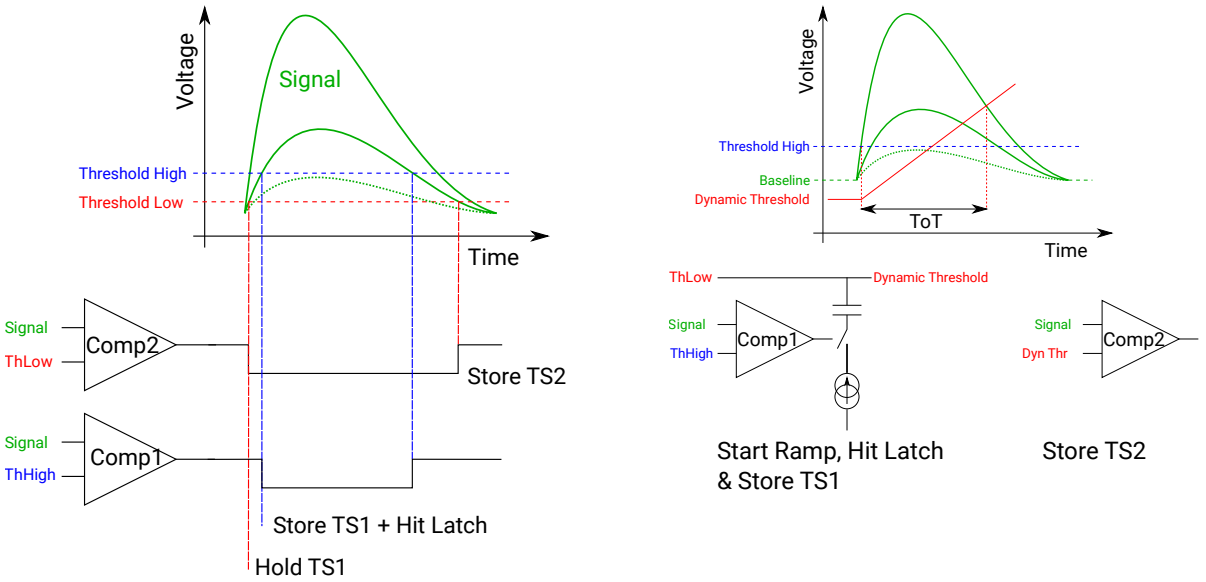

(a) 2 Thresholds concept.

(b) Ramp concept.

Figure 7.5: Time-walk correction concepts. Modified from [34].

Mode	Timestamp 1	Timestamp2
ToT Mode	Falling Edge Comp1	Rising Edge Comp2
2 Threshold Mode	Falling Edge Comp2	Rising Edge Comp2
Ramp Mode	Falling Edge Comp1	Falling Edge Comp2

Table 7.3: Timestamp latching depending on TWC mode.

7.1.4 State Machine

The state machine governs the internal readout of the MuPix8. Each of the three sub-matrices has its own state machine and readout link. It is discussed in detail in Refs. [33, 36–38] and is only summarized here.
As soon as a digital cell registers a hit, a signal is sent to the end-of-column (EOC) cell. This cell is shared for all pixel in one column, so matrix A & B have 48 EOC-cells and matrix C has 32. If this hit signal is present, the hit with the lowest row address in each column is loaded into the EOC cell. Then, each EOC is scanned if it contains hit data which is then sent to the serializer. As result of this logic, each readout cycle can only contain one hit from each column. Chronology is not preserved. The state machine clock frequency is given by half the reference clock frequency for the phase-locked loop (PLL) which generates the clock for the chip and is the base frequency of the timestamps.

In this work, the reference clock has a frequency of 125 MHz.
The state machine is additionally slowed down by the register value of the clock divider *timerend*. The frequency is then given by Eq. 7.3. At $timerend = 0$, the readout produces hits with wrong addresses, likely due to an issue in the power distribution. Therefore, the state machine is always slowed down to at least half the maximum frequency by $timerend \geq 1$.

$$f_{\text{State Machine}} = \frac{f_{\text{ref}}}{2 \times (1 + timerend)} \tag{7.3}$$

7.1.5 Production

The MuPix8 has been produced in the aH18 process by ams [39]. Due to production problems, the delivery was delayed. However, some wafers of a preproduction have been delivered in August 2017 to test these chips.
The final production has arrived in June 2018. Chips of both batches are characterized in this thesis. The MuPix8 has been produced with 4 different substrate resistivities: 20 Ω cm, 80 Ω cm, 200 Ω cm and 1 kΩ cm.
In both productions, numerous problems and low yield were observed. The most commonly encountered failures are:

- shorts between power, ground or HV nets
- broken registers, which prevented configuring
- large inefficiencies in the center of the chip
- bad LVDS links

Fully functioning chips show large variations in efficiency and time resolution. Where wafer tracking is available, a strong correlation between performance and chips of the same wafer and their performance is observed [40]. This makes difficult to disentangle issues from problems in the substrate, in the process, in the design or even in the method of cutting the chips.

7.1.6 Matrix B & C

Matrices B & C use a current driven signal transmission as mentioned in 7.1.1 and 7.1.2. This is a change from the previous MuPix prototypes which used a source follower like matrix A. The basic concept is a current generated in the digital cell that flows into the analog cell. The pulse in the analog cell is then modulated on to this current and induces a voltage signal in the digital cell. In a simplified way this can be imagined as current source in the digital cell and a load in the analog cell. Depending on the signal, the analog cell changes the load which is transformed into a voltage signal by the current source. The transmission of a current signal has the advantage that it has a low voltage amplitude. This causes almost no loss of signal to the capacitive coupling of neighboring lines, which depends on the voltage. As the MuPix8 and the final chip for the Mu3e experiment require dense lines between all the analog and digital cells, this concept which allows smaller line spacing, would be favorable.
However, with the default setup, the current mode matrices showed a worse performance than the source follower matrix. For example, the current mode matrices showed a much worse time resolution than the source follower matrix, as seen in Fig. 7.6. Here, the difference between the timestamp of a hit and the timestamp of a timing reference scintillator called Trigger is plotted. Lab measurements showed that the delay between pixels in one column was already about 1 µs between e.g. row 20 and row 100, which is unsuitable for online correction.
Also tests with a Sr90 showed a significant efficiency drop in the center of the matrices as shown in Fig. 7.7a, where the source was pointed at top center of the matrix. By changing the settings of the receiver DACs the gradients from top to bottom and from the sides to the center can be reduced. With improved settings in Fig. 7.7b a large fluctuation remains as seen near the center of the spot in the top part.
For these reasons it was decided to postpone the characterization of Matrix B & C. In this thesis only matrix A is characterized and discussed.

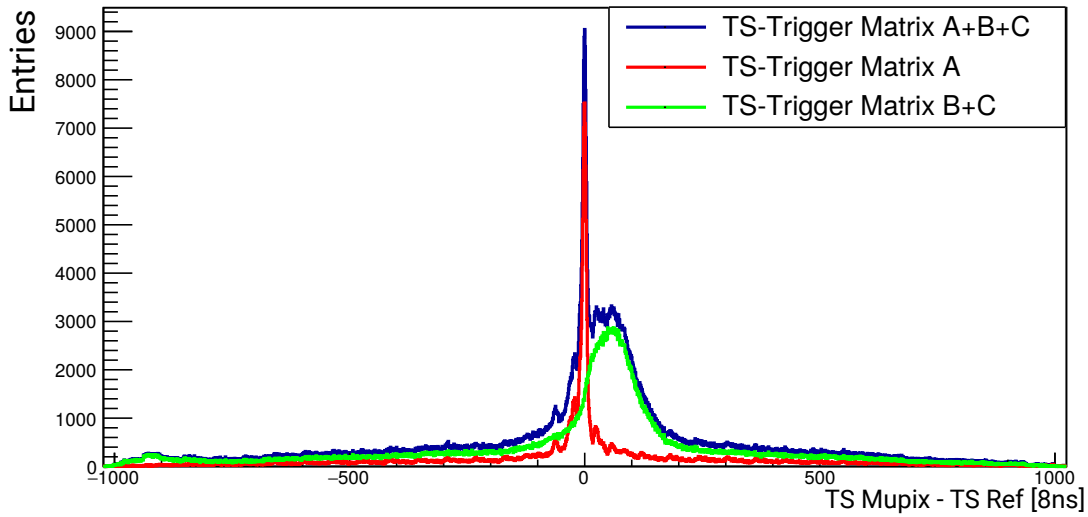

Figure 7.6: Uncorrected time resolution for the different matrices from the October 2017 testbeam at DESY.

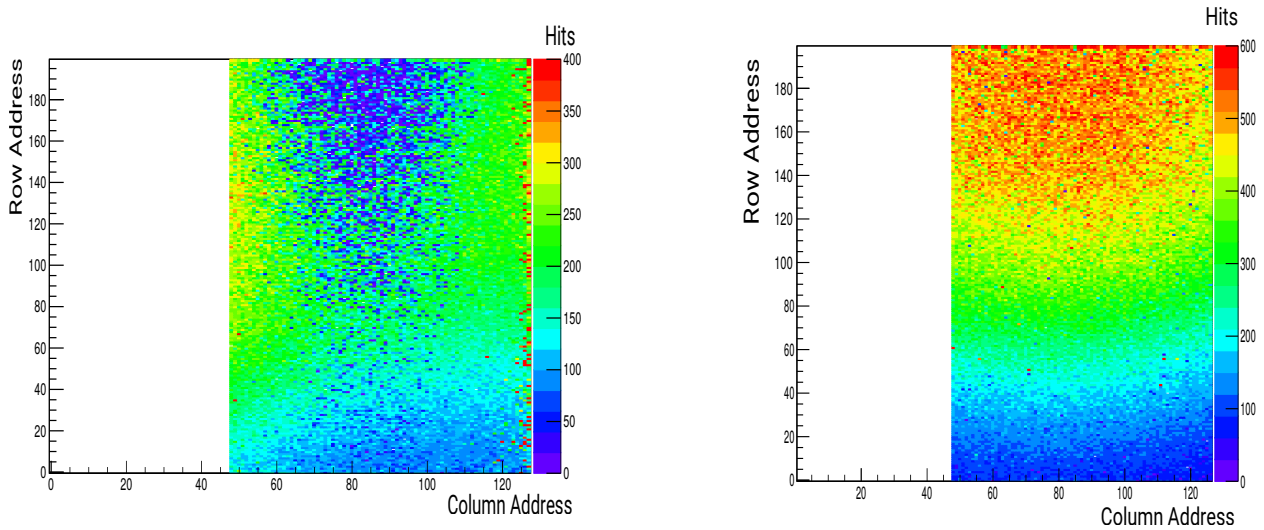

(a) Default Settings.

(b) Improved settings.

Figure 7.7: Hit maps for Matrix B & C with a Sr90 source in the top of the hit map.

7.2 MuPix8 PCB

The MuPix8 PCB [41] shown in Fig. 7.8 is a Printed Circuit Board (PCB) which was developed to supply the MuPix8 with all necessary voltages, currents, clocks and other signals. The MuPix8 chip can be directly glued and bonded to the PCB or it can be connected to the PCB via an edge connector and a daughter PCB called insert on which the chip is glued and bonded. The PCB generates the supply voltage and the necessary current to power the chip. The reference voltages for the baselines and VDDRAM are controlled by adjustable voltage dividers and the thresholds are generated by on-board DACs with amplifiers. To reduce the impact of ripples in the voltage distribution all voltages, including the HV for the sensor diodes, are filtered by capacitors. The injection is generated on-board by a DAC and a switch. The injection and the Hitbus can be probed by LEMO® connectors. To ensure the analog quality of the data links of the MuPix, an LVDS repeater drives the links from the PCB to the DAQ system.

Figure 7.8: MuPix8 PCB V2

7.3 MuPix8 Insert

The MuPix insert (Fig. 7.9a) [36] is an entirely passive PCB on which only resistors and capacitors are mounted. Its main purpose is to allow easier change of sensors in case of sensor failure or comparison measurements. It also gives access to test points to measure voltages from dedicated test pads of the chip which can not be connected to the mother PCB due to the limitation of traces in the edge connector. The AmpOut has to be tapped here for example. To protect the chip from dust and mechanical damage, custom 3D-printed frames have been produced which are sealed by polyimide tape, seen in Fig 7.9b.

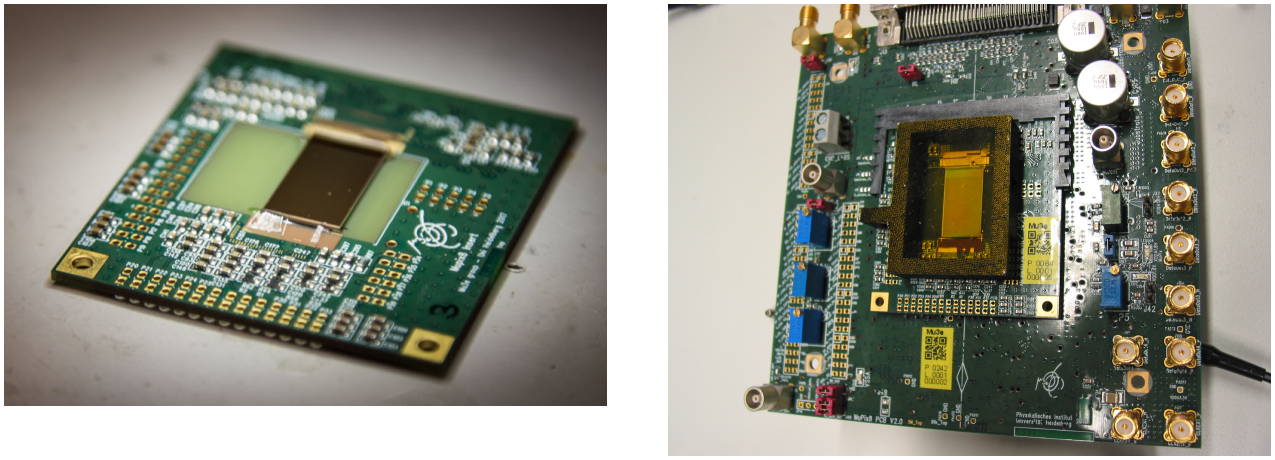

(a) MuPix8 insert.

(b) Chip on insert in the mother PCB.

Figure 7.9: MuPix8 insert with chip and in the mother PCB.

7.4 FPGA

The term Field-Programmable Gate Array (FPGA) describes an integrated circuit (IC) which consists configurable logic elements. Instead of a fixed application, it can be programmed and reprogrammed for different uses. The FPGA used for the MuPix8 readout is a Stratix IV GX FPGA Development Board [42]. The firmware of the FPGA is extensively discussed in Ref. [38]. The FPGA supplies the MuPix8 with the reference clock as well as the configuration and processes the data from the LVDS links. The data is then sent to the DAQ PC via PCIe [43].

7.5 DAQ

The data acquisition software is uses the code base of the MuPix Telescope [44]. It is adapted to the MuPix8 and can readout multiple sensors at once. For a detailed discussion see Ref. [40]. The version used in this thesis has been modified to operate only a single chip.

7.6 Radioactive Sources

Two different radioactive sources were used in this thesis, iron-55 and strontium-90.
Iron-55 (Fe55) [45] decays via electron capture to manganese-55 with a decay half-life of 2.737 years. After the electron capture the electron shells adapt to the different charge in the nucleus. An electron of a higher shell fills the vacancy of the captured electron. The energy released by this transition is emitted by an Auger electron of 5.19 keV 60% of the time. This electron has so low energy that the probability of it leaving the source is negligible. Next in probability are the $K_{\alpha 1}$ and $K_{\alpha 2}$ lines with a probability of 16.2% and 8.2% respectively. These transitions are photon emissions due to a electron from a higher shell filling the vacancy of a captured K-shell electron. Since the energies of both transitions (5.898 75 keV and 5.887 65 keV) are very close to each other they are treated as mono-energetic line of 5.9 keV. The K_{β} transition with 6.490 45 keV has only a probability of 2.85% which is a magnitude less likely than the K_{α} lines. In the other cases the energy is released via rare transitions and Auger electrons with less energy than the most probable decay electron. For this work, it is assumed to be a monochromatic 5.9 keV x-ray source.
Strontium-90 (Sr90) [46] has two relevant decays. First, Sr90 decays to yttrium-90 via β^- decay with an energy of 0.546 MeV and a half-life of 28.79 years. The yttrium then decays to the stable zirconium-90 again by β^- decay with a half-life of 64 hours and 2.28 MeV decay energy.

7.7 Timing Reference

The timing reference for the MuPix8, developed in the scope of this thesis, consist of scintillating tiles with SiPMs, which are read out by a PCB. The scintillator material BC-408® [47] by Saint-Gobain Crystals® which is cut into 20 mm × 20 mm × 4 mm tiles. This means that the tile is bigger than the MuPix8 but has the right scale for a final Mu3e sensor [18]. The used SiPMs are MPPC S13360-3050CS® [48] from Hamamatsu Photonics K.K.® with a sensitive area of 3 mm × 3 mm and a pixel pitch of 50 µm. To prevent the loss of light due to the size difference, the tile is wrapped in a mantle of an aluminum polyimide laminate which reflects the light from all surfaces except the interface of the SiPM. The mechanical frame is custom 3D-printed and made out of black material to shield more light. The light tightness is further improved by black vinyl tape and black acrylic paint.
For testbeam measurements at beams with a hadronic component also tiles with acrylic light guides were fabricated. For this thesis only tiles without light guide were used. In Fig. 7.10a, a fully assembled tile with rectangular light guide is shown next to the components for a tile with trapezoidal light guide, the aluminum polyimide laminate reflective mantle, the quadratic tile with the light guide and the 3D-printed frame.

The tile PCB [49] allows to connect one tile for direct analog output or up to two tiles with a logic output. The PCB has two comparator channels with individual thresholds and NIM outputs. If desired they can also be set in coincidence by a fast AND on the board. For this thesis only one tile per PCB was used. Fig. 7.10b shows a tile without light guide attached to the back of a tile PCB.
To test the time resolution of this reference system, two tile boards, each equipped with a tile, are mounted on top of each other and are exposed to a Sr90 source. The delay between the channels is measured and histogrammed by an oscilloscope (Tektronix DPO 7254C [50]). The standard deviation of this histogram is the time resolution. This measurement is done at two bias voltages for the SiPMs at comparator thresholds of 30 mV to 35 mV. The result is summarized in Tab. 7.4. The resolution of a single tile, assuming that both tiles have roughly the same resolution, is then given by Eq. 7.4 which is roughly 1.4 ns. This is consistent with results in Ref. [51] for scintillator strips of a similar material and SiPMs of the same type.

Tile HV [V]	Coincidence Time Resolution [ps]
54.5	2185.9 ± 3.9
55	2006.8 ± 4.3

Table 7.4: Time resolution for two tiles in coincidence

$$\begin{aligned} \sigma_{total}^2 &= \sigma_1^2 + \sigma_2^2 \\ \sigma_1 &\approx \sigma_2 \\ \sigma &\approx \sqrt{2} \cdot \sigma_{tot} \end{aligned} \tag{7.4}$$

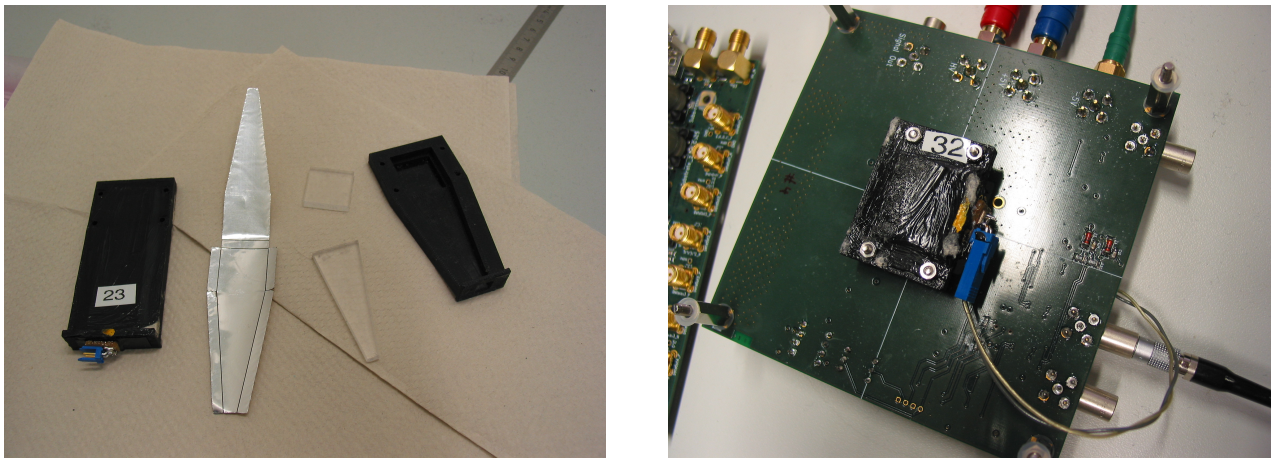

(a) Fully assembled tile with light guide and components.

(b) Tile without light guide mounted to the back of the tile PCB.

Figure 7.10: Tile components and fully assembled tile.

Part III

Measurements

8 Analog Measurements

In this chapter the analog performance of the MuPix8 amplifier cell, Sec. 7.1.1, is measured and discussed. The impact of the multiple DACs which steer the amplification and shaping is investigated.

8.1 Setup

The measurements in the following have been made using an oscilloscope (Tektronix MSO 4104 [52] and Tektronix DPO 7254C [50]) and the analog outputs of the MuPix8 and the PCB. The trigger is given by the falling edge of the injection. It is generated on the PCB and terminated by 1 MΩ, otherwise the current charging the capacity would flow into the oscilloscope instead of the pixel. The hitbus is also tapped on the PCB and is terminated by 50 Ω. The AmpOut can only be measured at test points on the insert. It is measured with an active probe and a termination resistor of 1 kΩ. The bandwidth of the probe is set to 20 MHz to reduce the impairments of high frequency noise. As the AmpOut level depends on the selected pixel and the setting of the DACs and reference voltages, the amplitude is measured as difference between the maximum and the low level of the waveform. The minimum is not used because of noise and an undershoot at the end of the pulse. Rise and fall time are either measured as time difference between the 10% and the 90% points of the waveform or as time difference between the crossing of fixed voltages. All values are transformed into slew rates in mV/ns. The measured ToT is defined by the 50% crossings of the hitbus. An example of an Fe55 pulse is found in Fig 8.1a where the measurement variables of the AmpOut are annotated. An injection gauged to a Fe55 signal can be seen in Fig. 8.1b.
At least 2000 samples are taken for all measurement points which gives a statistical error of 2.2% or less. Errors given for a measurement point in this section, are either the standard deviation of the measurement of the oscilloscope or derived from it. Since both the AmpOut and the hitbus have driving circuits which influence the output, the data is investigated with respect to relative changes rather than absolute ones.

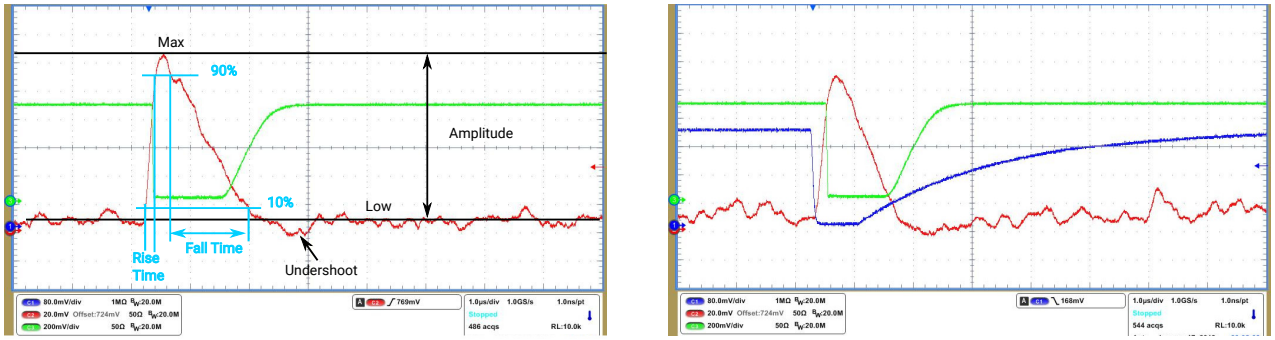

(a) Fe55 pulse.

(b) Fe55 gauged injection.

Figure 8.1: Examples of measured waveforms. The AmpOut is shown in red, the hitbus in green and the injection in blue.

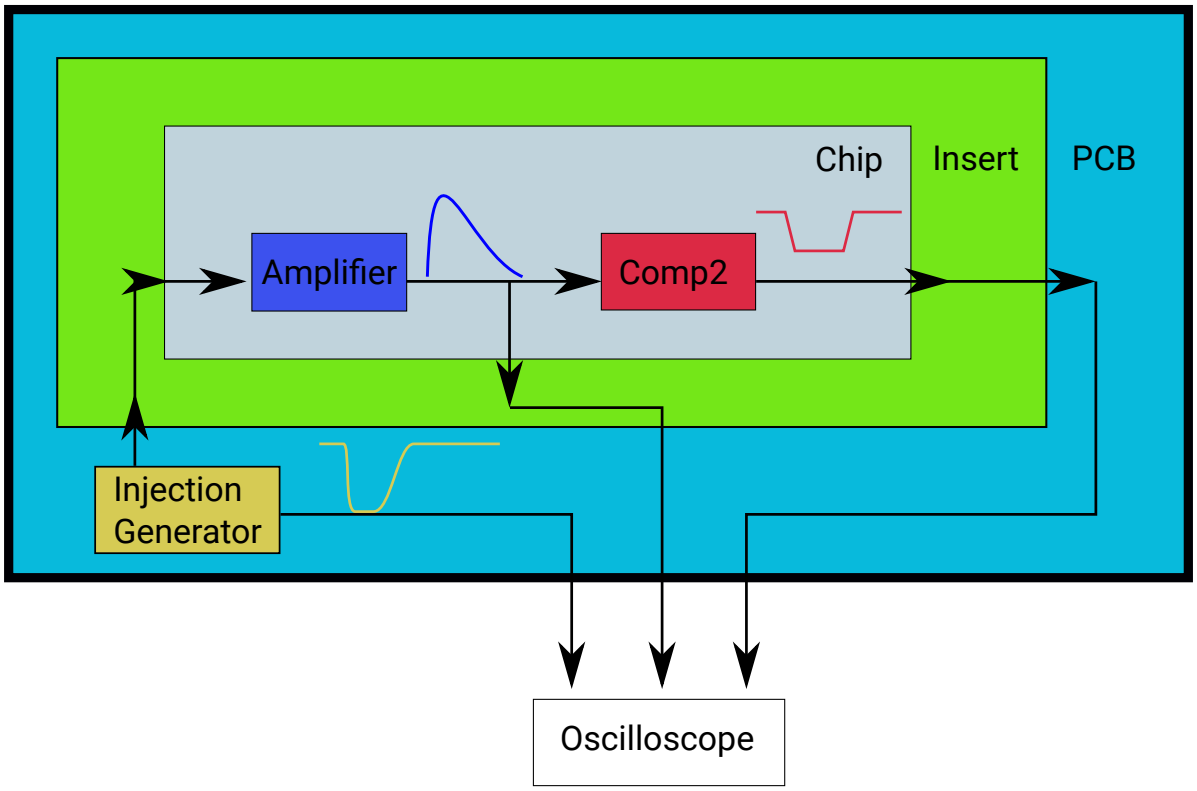

Figure 8.2: Block diagram of the measurement setup.

8.2 Proof of Principle Measurements

The first measurements to test the AmpOut and hitbus are done with chip 84-2-6 and the settings used are found in the appendix in Tab. B.1. From measurements with the Fe55 source an AmpOut pulse height U of about 100 mV was determined. Given the monochromatic nature of the Fe55 source and the assumption that the AmpOut acts as an amplifier with a gain of 1, the feedback capacity C_{FB} can be estimated. From Tab. A.1 the average number of electron-hole pairs generated per deposited energy is known, the energy of the Fe55 source is given in Sec. 7.6. On average, about $n = 1600$ electron-hole pairs are created, so the total charge is $Q = 1600\,e$. From $Q = C \times U$, $C_{FB} \approx 2.56\,\text{fF}$ is derived. The result is in good agreement with the 2.5 fF given by the documentation [33]. The injection voltage required to create a pulse of the same height is roughly 250 mV which gives an estimate for the injection capacity $C_{inj} \approx 1\,\text{fF}$.
To test the linearity of the amplifier, the AmpOut and the hitbus ToT are measured for different injection voltages. The result is seen in Fig. 8.3a. The AmpOut pulse starts to saturate around 1 V to 1.2 V injection voltage, while the ToT stays linear for a longer range. This effect can also be seen in Fig. 8.3b where a large pulse caused by a Sr90 source is shown. The pulse is no longer triangular as in Fig. 8.1, instead it takes a trapezoidal shape since its amplitude is limited by the circuit. Since the pulse is still longer than pulses with less signal the ToT still grows.

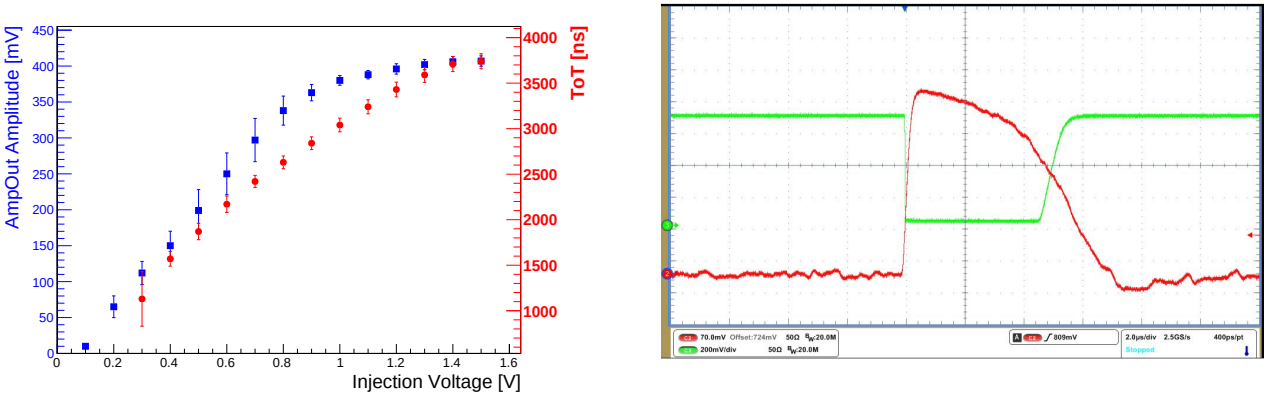

(a) Injection and ToT vs injected voltage.

(b) Large Sr90 pulse.

Figure 8.3: Measurement of the AmpOut saturation.

8.2.1 Spatial Dependence

The AmpOut is only available in column 0 as shown in Fig. 8.4, the spatial dependence along the column address can not be gauged by this tool. The dependence on the row axis is measured in Fig. 8.5a. Here for each pixel in column 0, the average AmpOut pulse amplitude for Fe55 is measured. No dependence on the row can be seen and pixel-to-pixel fluctuations are large.
The measurement points are histogrammed in Fig. 8.5b which shows a Gaussian like distribution. The mean is at 120 mV instead of 100 mV because the oscilloscope includes the undershoot (Fig. 8.1a), which is about 20 mV in this measurement.
For each pixel also a gauge to the Fe55 source is performed which is shown in Fig. 8.6. Here, a clear trend to higher required injection voltages can be seen above row 120. This could be due to the increased injection line length, such that the line capacity becomes significant.

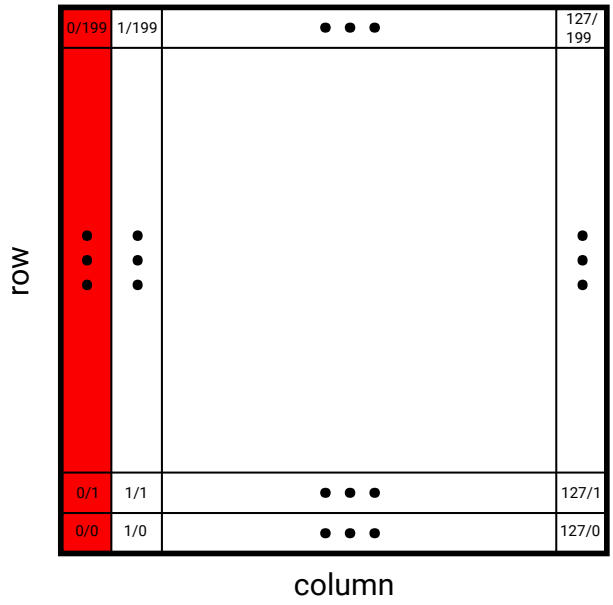

Figure 8.4: Coordinate system of the MuPix8. Pixel in red are available for AmpOut selection.

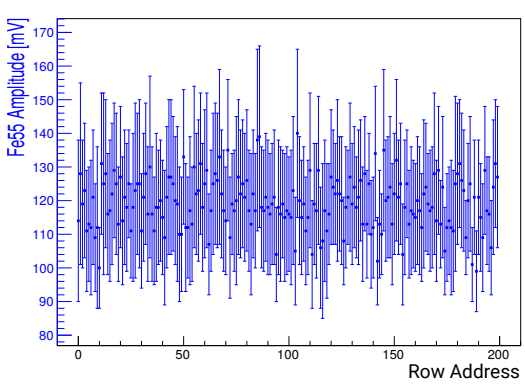

(a) Average Fe55 AmpOut pulse height along the row.

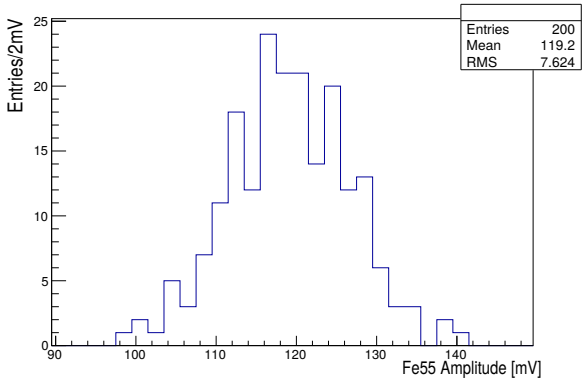

(b) Histogram of the average Fe55 AmpOut pulse height.

Figure 8.5: Row dependence of the average Fe55 AmpOut pulseheight.

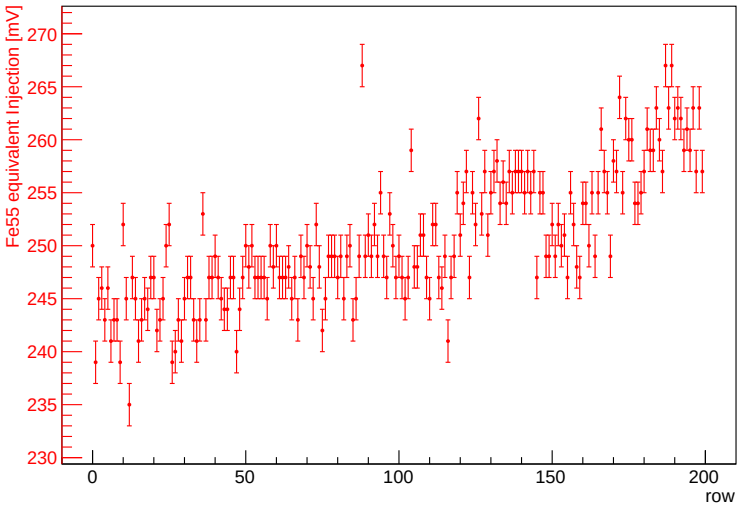

Figure 8.6: Injection voltage for Fe55 equivalent amplitude.

8.2.2 HV-Dependence

For previous MuPix prototypes an HV dependence for injection and Fe55 signals was observed [53]. These signals are monochromatic, so they should not depend on the HV, excluding cases where the depletion zone is smaller than the charge cloud from an Fe55 photon. The charge collection is much faster than the shaping time constants so a lower drift speed can not be measured. To test if the HV dependence of the injection is still present in the MuPix8 the dependence on the HV is measured for Fe55 and injection which is shown in Fig. 8.7. Fig. 8.7a shows the ToT and the approximate hit rate from the DAQ for Fe55. While the hit rate grows in a square root proportional to teh depletion zone, the ToT only grows only for the first few volts and stays then constant. The rise in Fe55 equivalent injection voltage is likely due an increased fraction of partial collected charge and a the decrease in noise due to the increase of the pixel capacity. For the injection in Fig. 8.7b no dependence can be observed.
A twofold change in capacities is likely the reason for the injection to not depend significantly on the HV. First is the implementation of the injection capacity. For previous prototypes, the injection was implemented as a metal layer above the n-well which formed a capacitance, that was dependent on the HV. For the MuPix8, the injection is implemented as capacity between two metal layers which is directly fed into the amplifier. Second, the feedback capacity is changed such that it is much smaller than the pixel capacity. Since the feedback and pixel capacity are in series the smaller capacity dominates. The pixel capacity is about 33 fF according to Eq. 5.6 which is much larger than the 2.5 fF of the feedback capacity. This calculation assumes 60 V HV and a substrate resistivity of 80 Ω cm.

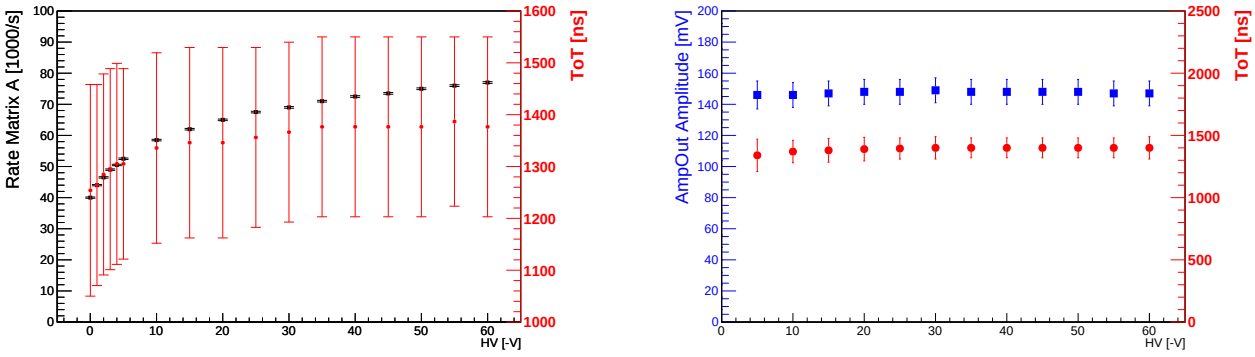

(a) HV dependence for Fe55.

(b) HV dependence for injection.

Figure 8.7: HV dependence for Fe55 and injection.

8.3 Crosstalk

In the MuPix8, the signals transmitted from the analog pixel to the digital partner cell are analog voltage signals. As the line spacing is limited, crosstalk due to capacitive coupling between the signal lines is expected to be an issue. Crosstalk was already found to be significant in the previous prototype [54] where the lines were shorter than 3 mm while the MuPix8 has lines up to 2 cm long. The crosstalk signal is coincident with the primary pulse and its ToT is shorter than the ToT of the primary signal which is why the crosstalk can not be seen on the hitbus due to the column bus structure. The AmpOut is multiplexed in the analog cell so the loss of signal can not be measured directly. The induced voltage signal on the transmission line couples back into the analog cell and can be observed on the AmpOut for pixel in the row below or above. This is measured for Chip 84-2-3 (Settings B.2) and is shown in Fig. 8.8. Fig. 8.8a shows that the crosstalk is limited by the amplifier saturation. This issue has been simulated in [55] and the results agree well.
A more detailed study has been made for sensors 84-2-3 and 84-1-5 (Settings B.4) in Fig. 8.9 and Fig. 8.10 respectively. Here, the charge is injected into the pixel in row n with 1.3 V injection, so that the amplifier saturates, and the AmpOut amplitude is measured. For all pixel from row n-2 to n+2 the ratios between the induced and the injected signal amplitudes (Fig. 8.9a and Fig. 8.10a) and with absolute amplitudes (Fig. 8.9b and Fig. 8.10b) are shown. The growth in crosstalk with the increasing line length is visible such that it in the highest rows it is large enough to induce signal even in the next neighboring line.
Crosstalk for the MuPix8 is discussed in detail in Ref. [40].

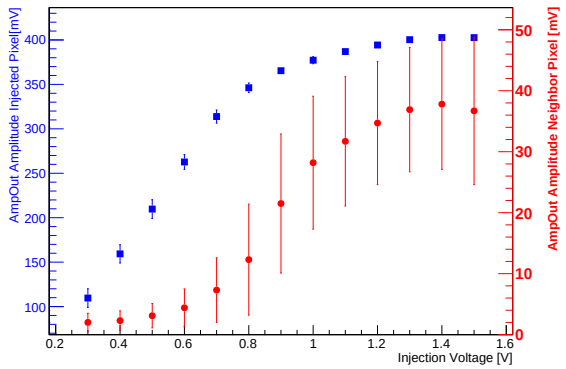

(a) Amplitude of the injected signal in pixel 100 and induced amplitude in pixel 101.

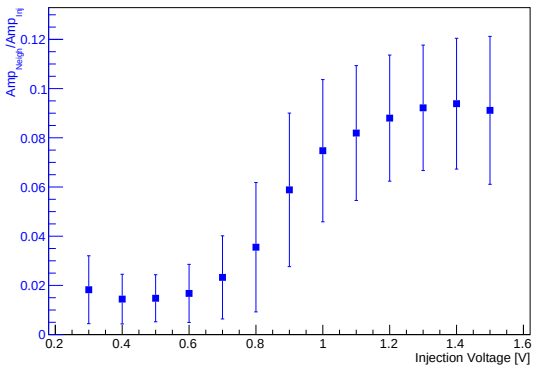

(b) Ratio between induced and injected signal.

Figure 8.8: Crosstalk for Chip 84-2-3 from pixel 100 to pixel 101.

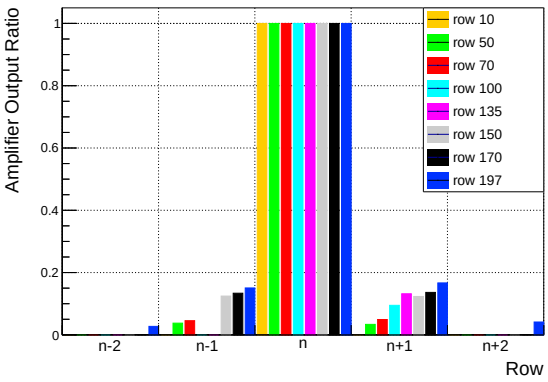

(a) Ratio between injected and induced signal.

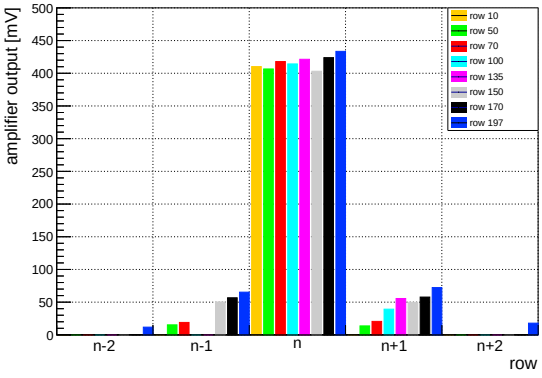

(b) Absolute signal amplitudes.

Figure 8.9: Crosstalk for Chip 84-2-3 as function of the row position.

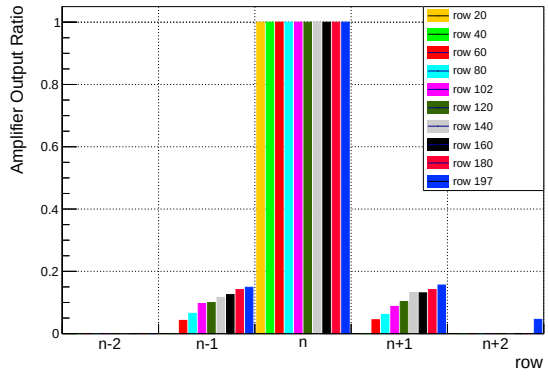

(a) Ratio between injected and induced signal.

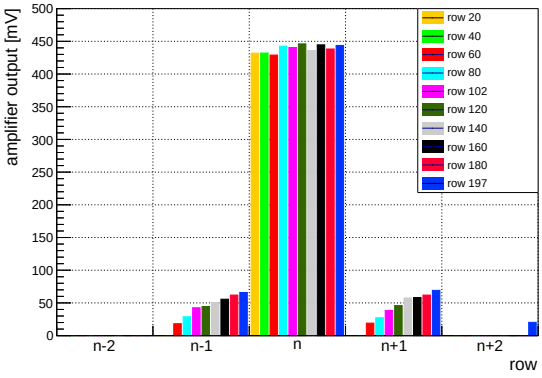

(b) Absolute signal amplitudes.

Figure 8.10: Crosstalk for Chip 84-1-5 as function of the row position.

8.4 DAC Dependence

The pulse shape of the MuPix8 amplifier can be approximated as triangle signal shown in Fig. 8.1b. In this approximation the pulse can be paremetrized by the amplitude and the slew rates of the rising and falling edge. Amplitude and slew rates are referred to as pulse parameters. To test the influence of the DACs on the shaping, the amplitude and slew rates are measured with the AmpOut for chip 84-3-25 (Settings B.3). A 0.75 V injection ($\approx$ 4800 electron equivalent) is chosen as the pulse is then large enough that the noise contribution is negligible. Each DAC for the analog cell was varied while the other ones are set to the default values in Tab. B.3. This assumes that the influence of the DACs is independent of the setting of the other DACs.
If the influence of the DACs is known, the settings can be optimized. Higher amplitudes can be either used to increase the efficiency for very small signals or to increase the threshold and reduce the noise rate. If the slew rate of the rising edge is large, time-walk is reduced, which results in a better time resolution. The dead time of the analog circuit is dominated by the longer falling edge so that an increased slew rate of the falling edge could be desired for very high rates.
After these measurements were performed, it was found that the capacitive decoupling of the voltages generated by the DACs on the insert has an influence on the performance. For example if VNFBPix was changed the AmpOut showed changing pulses until the new configuration had stabilized which took several seconds or until the decoupling capacitor was discharged. It can not be excluded that this issue has an impact on the measurements presented in this section. The general influence of each DAC on the pulse shaping should, however, stay the same.

8.4.1 Injection

By changing the injection voltage, different charge depositions can be mimicked. To first order, the pulse shape parameters should depend linearly on the injected charge as discussed in Sec. 6.2. Fig. 8.11 shows the amplitude and rising edge slew rate in Fig. 8.11a and the falling edge slew rate in Fig 8.11b. As seen in Fig. 8.3 before, all parameters grows linearly until the saturation starts to become significant.

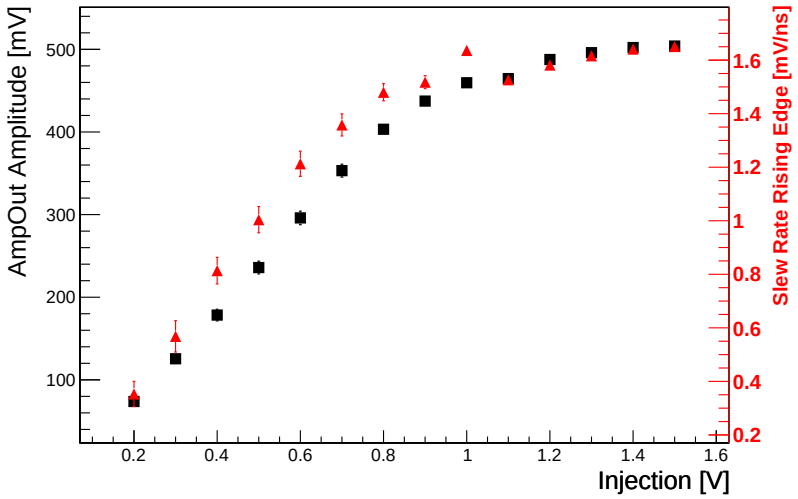

(a) Amplitude and rising edge slew rate.

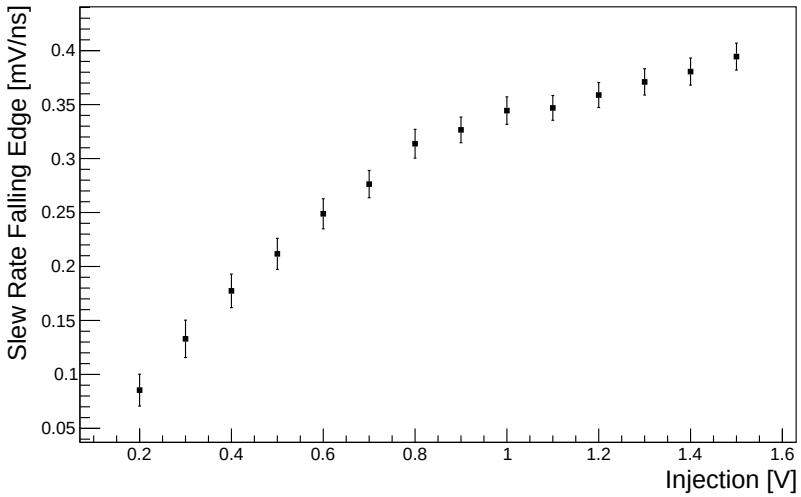

(b) Falling edge slew rate.

Figure 8.11: Pulse parameter dependence on the injected signal. The kink between 1 V and 1.1 V injection voltage is due to an error in the setup.

8.4.2 Hitbus DACs

The two DACs that control the performance of the hitbus, are VNBiasReg and VPBiasReg. The influence of these DACs on the rise time and the hitbus ToT is shown in Fig. 8.12. The comparator output and with it the hitbus are active low so the rising edge is later in time. The different scales on the rise time measurements (Fig. 8.12a and 8.12c) display a larger influence for VPBiasReg than for VNBiasReg. The opposite is true for the hitbus ToT (Fig. 8.12b and 8.12d), which demonstrates a bigger dependence on VNBiasReg than on VPBiasReg. The large dependence on these DACs indicates that the shaping of the hitbus DACs is too dominant to recover the comparator output.
Previous measurements were done with both DACs set to 0x1E.

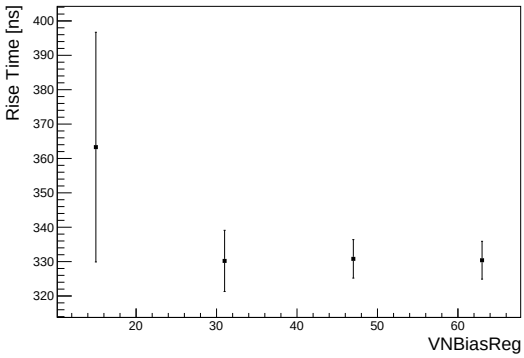

(a) Rise time dependence of VNBiasReg with VPBiasReg=0x3F.

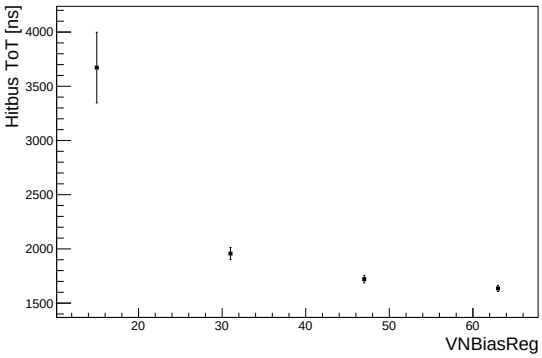

(b) ToT dependence of VNBiasReg with VPBiasReg=0x3F.

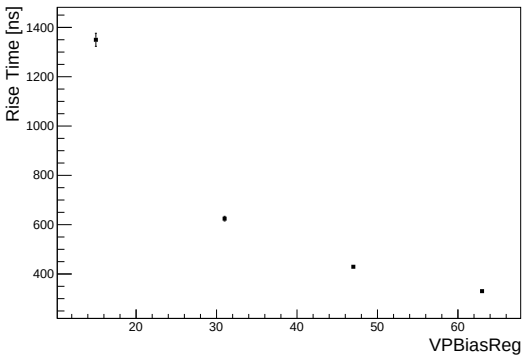

(c) Rise time dependence of VPBiasReg with VNBiasReg=0x3F.

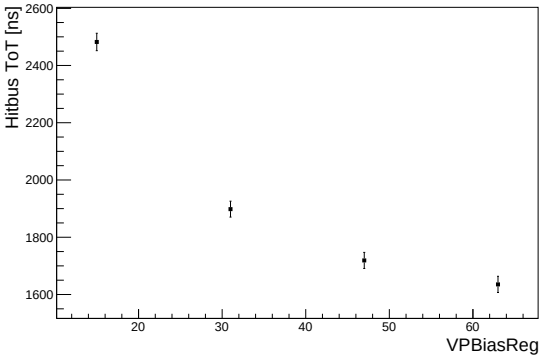

(d) ToT dependence of VPBiasReg with VNBiasReg=0x3F.

Figure 8.12: Rise time and ToT dependence on VNBiasReg and VPBiasReg.

8.4.3 VPFoll

The line driver of the AmpOut is controlled by the DAC VPFoll. The influence of this DAC is shown in Fig. 8.13. While the rising edge slew rate is growing until it saturates, the amplitude rises steeply and then starts to fall off again. This due to the low level of the AmpOut which rises with VPFoll. As the circuit has a limited operation range, the maximum can not increase any further. The falling edge slew rate stays constant with in the uncertainties.
The feedback capacity calculation was done with VPFoll = 10 and agrees well with the design parameter, so it can be assumed that the closest representation of the pulse of the amplifier lies around VPFoll = 10. Due to the change in rising edge slew rate, it is likely that the AmpOut has a shaping influence which keeps the amplitude constant but has a different shaping time constant. It seems that relative changes in the rising edge slew rate can be seen with the AmpOut, however, the absolute rise time can probably not be measured with this feature. This should be kept in mind for the following measurements.

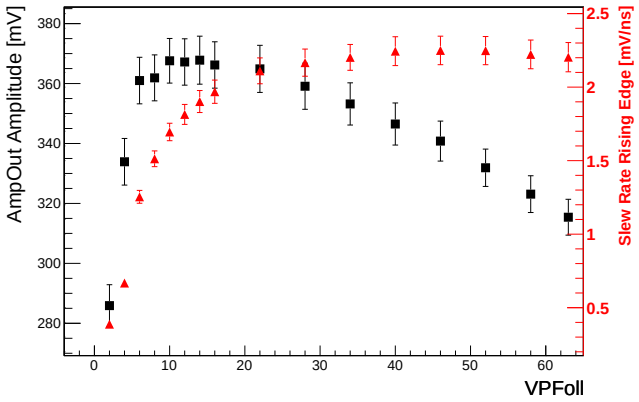

(a) Amplitude and rising edge slew rate.

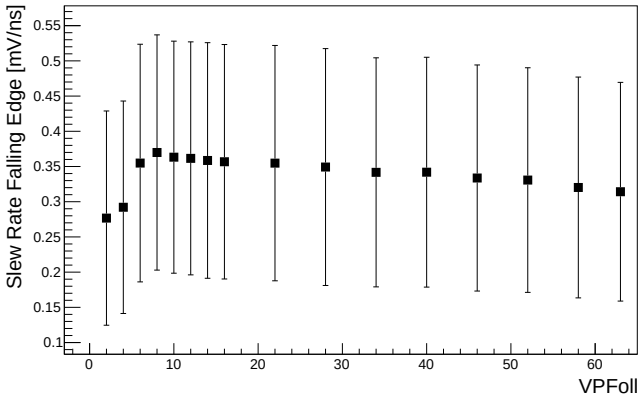

(b) Falling edge slew rate.

Figure 8.13: Pulse parameter dependence on VPFoll.

8.4.4 VNPix

VNPix, the current source for the amplifier, has a large impact on the rising edge and the amplitude, depicted in Fig. 8.14. Starting from low values the performance increases first, but decreases significantly for large values. As the rising edge slew rate and the amplitude do not peak in the same range, 10 to 14 for the amplitude and 14 to 16 for the rising edge slew rate, the most optimal point for time resolution and for efficiency are potentially not the same. The default value of 20 seems acceptable but a lower value appears to be better.

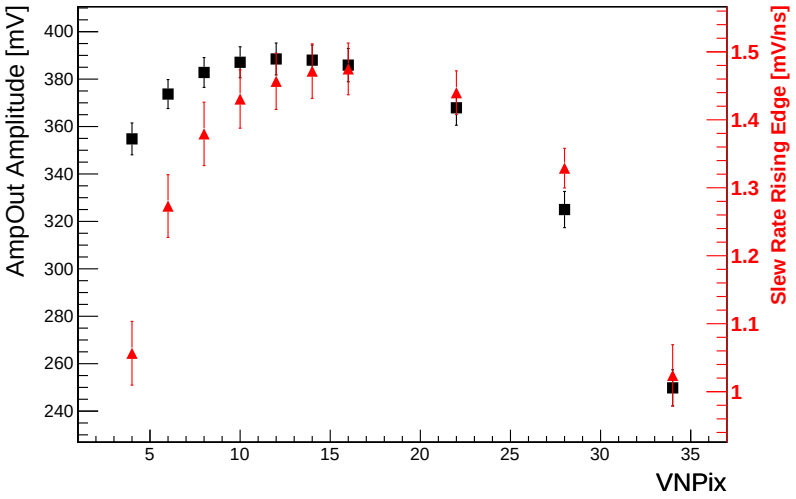

(a) Amplitude and rising edge slew rate.

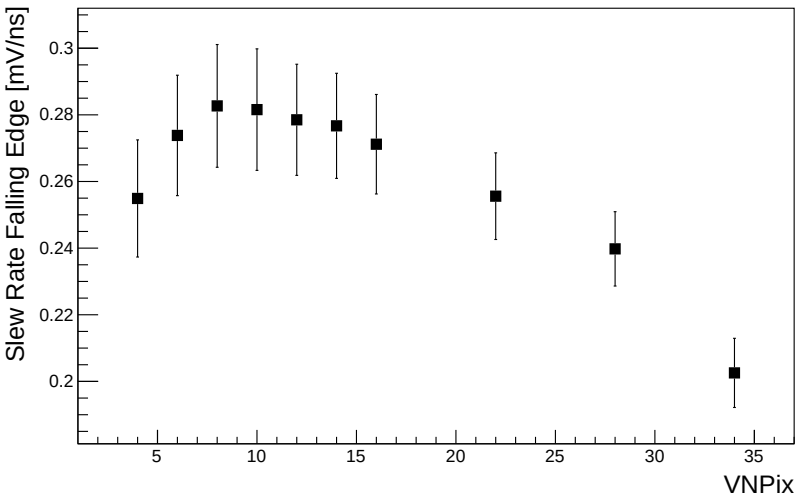

(b) Falling edge slew rate.

Figure 8.14: Pulse parameter dependence on VNPix.

8.4.5 VNFBPix

The main effect of VNFBPix is the linear feedback which shortens the pulse by increasing the falling edge slew rate as seen in Fig. 8.15b. This however reduces the amplitude and rising edge slew rate which can be seen in Fig. 8.15a. The default value of 10 shows an outlier in the rise time which is likely due to the mentioned decoupling capacity, otherwise it seems that a very low value of about 4 is desirable for maximum efficiency and time resolution. However, long pulses induce a higher dead time because no new pulse can be accepted if the amplifier is still shaping the previous signal.

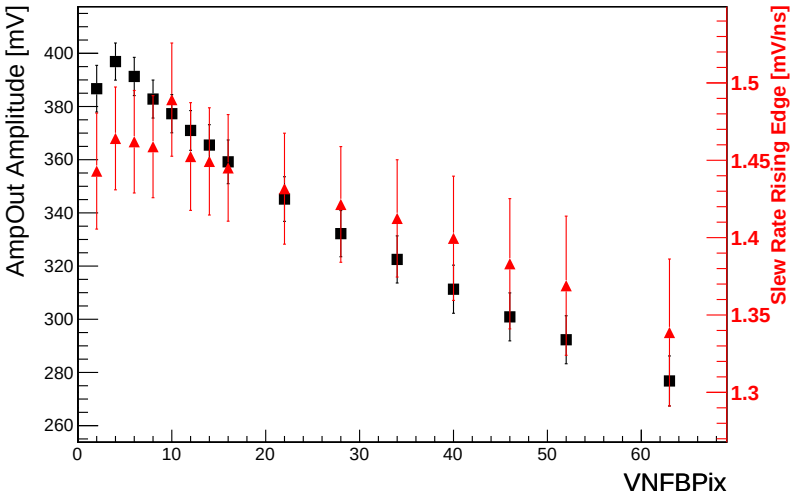

(a) Amplitude and rising edge slew rate.

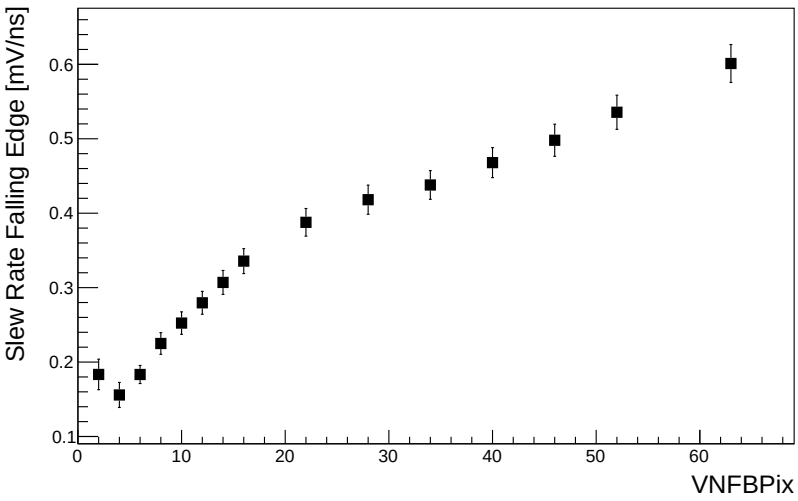

(b) Falling edge slew rate.

Figure 8.15: Pulse parameter dependence on VNFBPix.

8.4.6 VNFollPix

For VNFollPix, the internal feedback driver, the optimal working point is unclear as the rising edge slew rate and the amplitude do not peak at the same point, pictured in Fig. 8.16. The falling edge slew rate seems to be unaffected. As the source follower circuit of VNFollPix requires a lot of power, a lower value is favored for the power consumption if the performance impact is negligible. The AmpOut can not show the signal transmission to the digital cell which could be affected. The default of 10 is performing well so not much improvement is expected here.

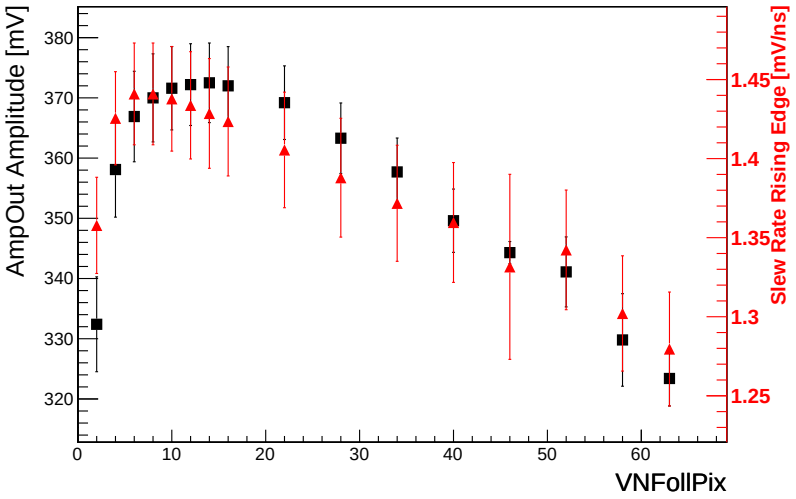

(a) Amplitude and rising edge slew rate.

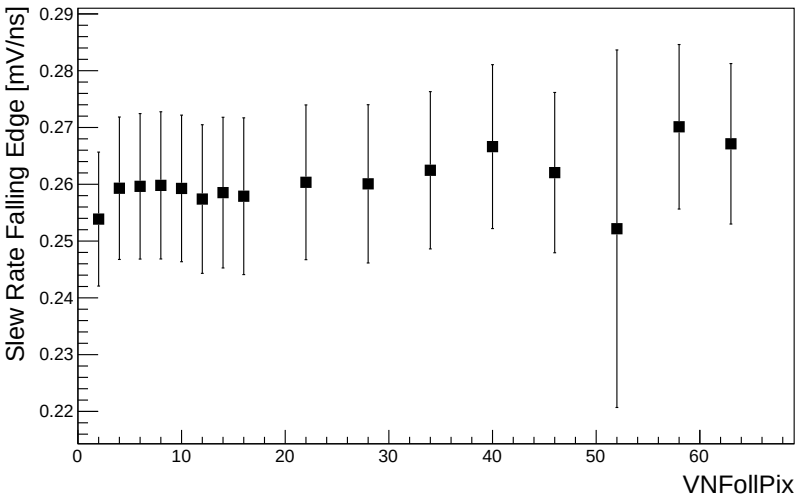

(b) Falling edge slew rate.

Figure 8.16: Pulse parameter dependence on VNFollPix.

8.4.7 VPLoadPix

VPLoadPix, the feedback capacity, shows the largest influence in rise time, see Fig. 8.17a. Here, a larger value than the default 5 seems to be better. For too high values the amplitude is falling as the charging up of the capacity takes too long so that the full pulse height can not be reached. The region between 5 and 10 (default is 5) seems to be a the optimal region. The impact on the fall time as shown in Fig. 8.17b is only significant at high values, which are disfavored.

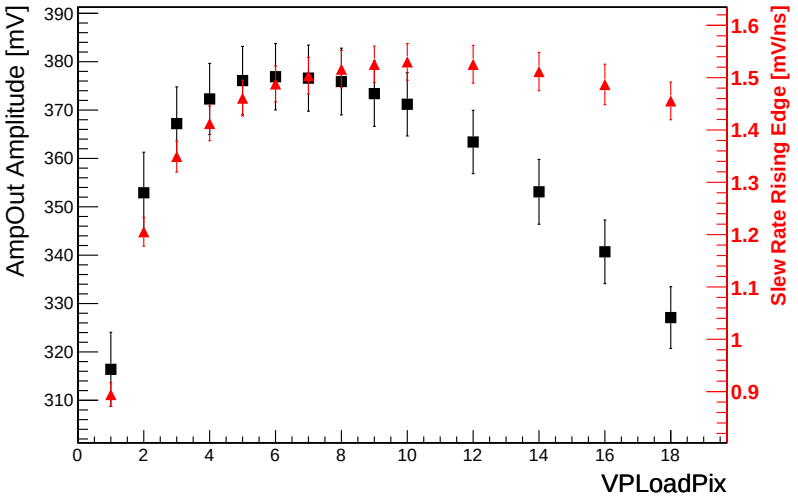

(a) Amplitude and rising edge slew rate.

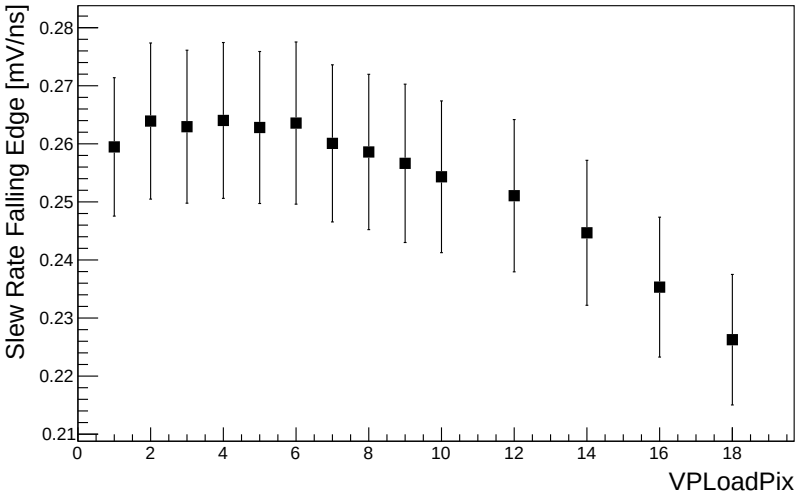

(b) Falling edge slew rate.

Figure 8.17: Pulse parameter dependence on VPLoadPix.

8.4.8 VNBiasPix

Beside a slight decrease in amplitude the influence of VNBiasPix (Fig. 8.18), the bias resistor of the sensor diode, seems negligible. A slight increase in the standard deviation of the pulse parameters, could be interpreted as an increase in noise. Given these results, there seems to be no reason to change the value from the default 0.

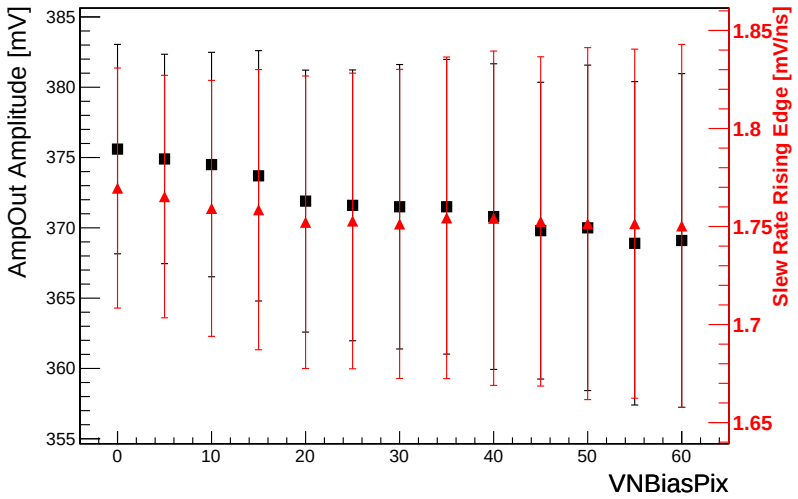

(a) Amplitude and rising edge slew rate.

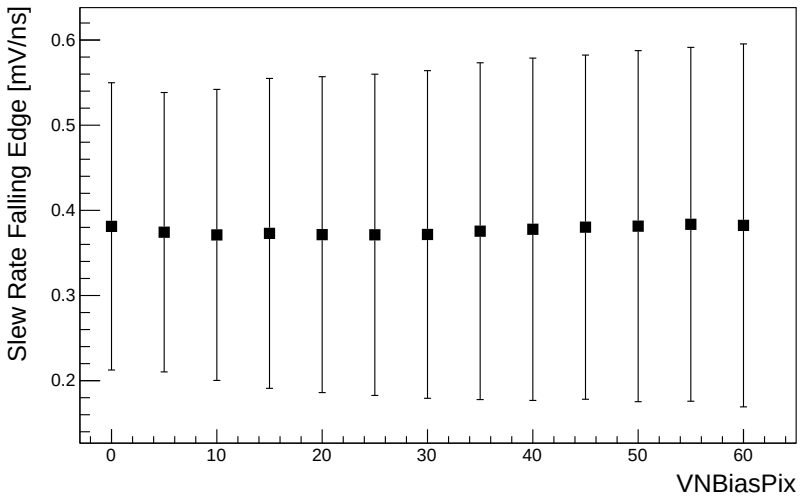

(b) Falling edge slew rate.

Figure 8.18: Pulse parameter dependence on VNBiasPix.

8.4.9 VNOutPix

The main effect of VNOutPix, the bias of the transmission line, is a downwards level shift of the AmpOut. It seems that the high level falls steeper than the low level which induces the decrease in amplitude seen in Fig. 8.19a. The rising and falling edges stay rather constant, as visible in Fig. 8.19a and Fig. 8.19b. VNOutPix influences the signal transmission, so the optimal working point can not be determined via the AmpOut, but has to be found in the analysis of hit data. The difference in line lengths has most likely a big impact on this parameter. The default value of 10 appears to be the optimum value. Since the circuit uses a significant amount of power a low value is desirable.

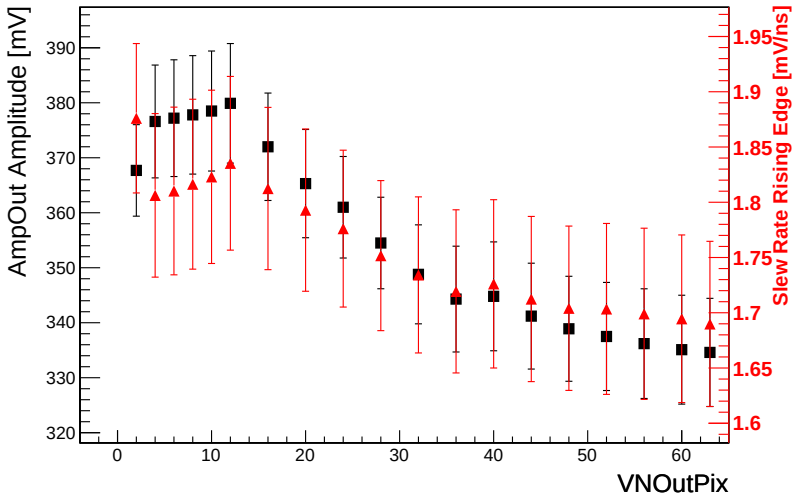

(a) Amplitude and rising edge slew rate.

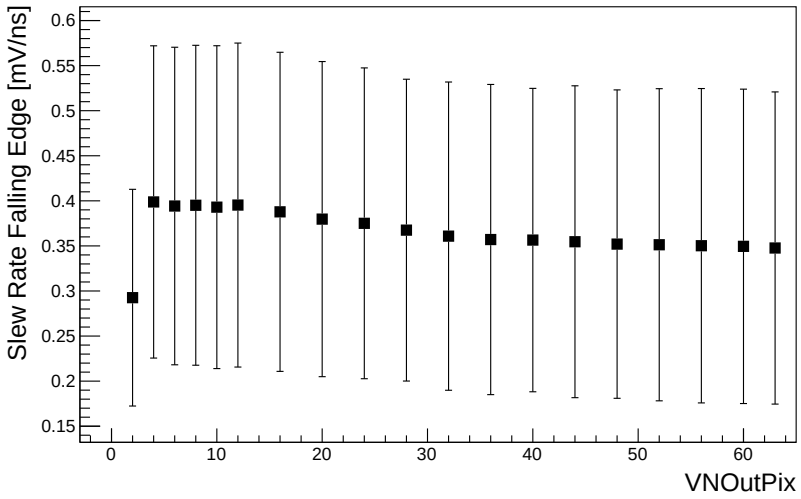

(b) Falling edge slew rate.

Figure 8.19: Pulse parameter dependence on VNOutPix.

8.4.10 BlResPix

For BLResPix, which is the resistor for the high pass of the base line coupling in the pixel, the impact lies in the falling edge. The amplitude is slightly shrinking as seen in Fig. 8.20a while the rising edge slew rate stays the same. The falling edge slew in Fig. 8.20b increases which is expected. This DAC can be used to reduce the dead time or the ToT while only reducing the amplitude slightly.

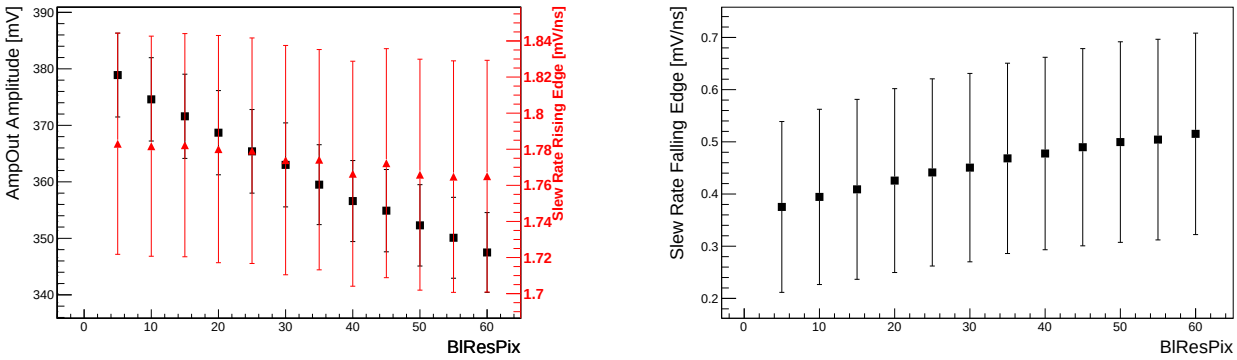

(a) Amplitude and rising edge slew rate.

(b) Fall rising edge slew rate.

Figure 8.20: Pulse parameters dependence on BlResPix.

8.4.11 DAC Optimization

From the previous measurements, a new set of DACs, see Tab. 8.1, is compiled by selecting the most optimal point for amplitude and rising edge slew rate for each measured DAC. This approach is very simplified as all elements in the amplification circuit are very dependent on each other. The new set is compared with the old set in Fig. 8.21, which shows an improvement for the new set. All DACs excluding BLResPix are then varied around the new set to check if the new set is the optimal operation point. Most variations perform worse or equal to the new set, indicating a convergence to the optimum, although the power consumption is reduced with the new set compared to the old one. The variation of VNFollPix and VPLoadPix display slightly better performance, so the optimum is not reached with the new set but close in performance. Nonetheless, more detailed studies on the amplifier DACs, which were done for the previous prototype in Ref. [56] should be repeated.

DAC	New Value [hex]	Default Value [hex]
VNPix	F	14
VNFBPix	4	A
VNFollPix	C	A
VPLoadPix	A	5
VNBiasPix	0	0
VNOutPix	A	A
BlResPix	5	5

Table 8.1: New DAC set and defaults for the analog DACs.

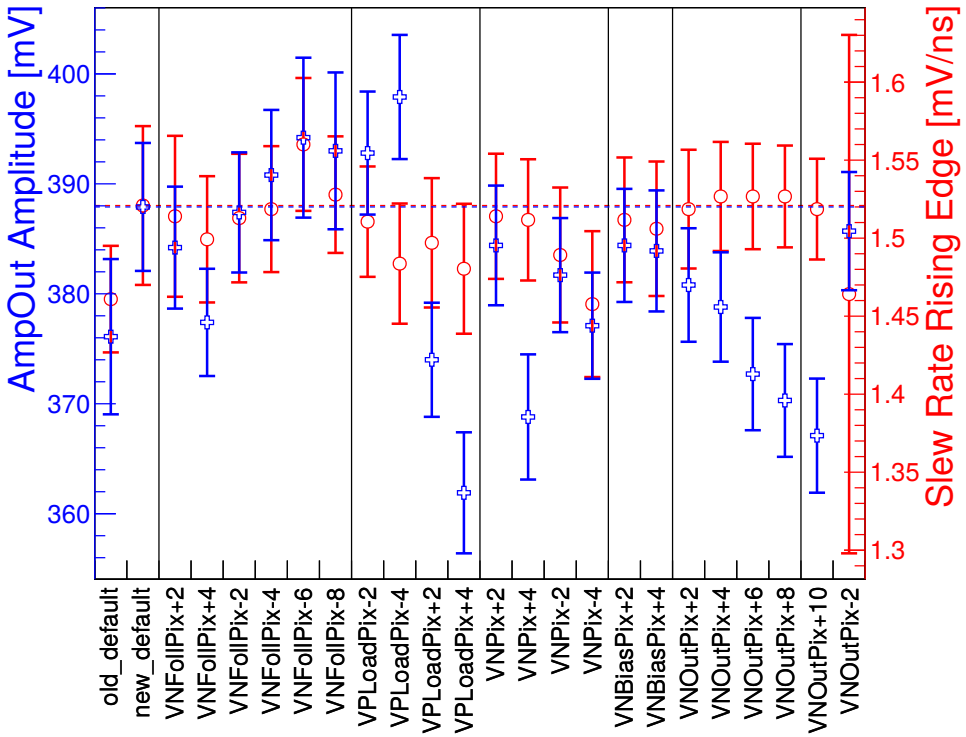

Figure 8.21: Amplitude and rising edge slew rates for different DAC sets. Dashed lines mark the value of the new set in Tab. 8.1, old default refers to the DACs in B.3. The other points mark the deviation of the new set of the named DAC by the value behind the name.

9 Time Resolution

For the previous MuPix prototype, the MuPix7, a time resolution of 13.5 ns [57] was measured for a power consumption which is within the constraints of the cooling for the Mu3e experiment. One of the limiting factors was found to be time-walk, which is the reason for the TWC features implemented in the MuPix8. In the following, lab measurements of the time resolution and TWC are presented.
As reference system, a scintillating tile with a tile PCB as described in Sec. 7.7 is mounted behind a MuPix8 in the PCB. The NIM output of the tile PCB is connected to the FPGA adapter card, where it is sampled with 500 MHz and referred to as trigger. Since the MuPix8 has 8 ns time binning, the last two bits of the trigger timestamp are discarded for synchronization. The time resolution is determined by the sigma of a Gaussian fit to the central part of the latency distribution. The intrinsic contribution due to the binning of $8/\sqrt{12}$ ns is not subtracted but is connstant for all measurements. The ToT is calculated by Eq. 7.2 as described in Sec. 7.1.2. Hits with Gray TS2 = 0x3F are excluded, which is the value after reset. Stuck timestamps will always have this value, although it is also a valid timestamp otherwise. To prevent a distortion due to stuck timestamps, hits with this TS2 are discarded.
Only one hit of each column can be readout at once, so hits can migrate in the next readout cycle, called frame, if there is a hit in the same column but in a lower row. Triggers are added to the next readout cycle after they are registered. Consecutive readout cycles are merged together until an empty frame is found to prevent the loss of correlation. Empty cycles are removed. Since no track information is available in this setup, clusters from charge sharing and crosstalk are removed for the timing analysis and only single hits are taken into account. As shown in Sec. 8.3, crosstalk is row dependent, requiring a dedicated correction for the signal loss. Triple crosstalk evens, three adjacent hits in the same column, are a clear crosstalk pattern, however, if one of the crosstalk induced signal doesn't pass the threshold, the pattern can not be distinguished from charge sharing. In some rows, due to metal layer transitions or larger line spacing, no triple crosstalk can be induced. Adjacent hits in the same row can not be due to crosstalk and are caused by charge sharing. To prevent a bias from unresolved ambiguities from crosstalk and charge sharing, merged frames are scanned for clusters in both dimensions. If two adjacent hits, in column or row, are within a merged frame, both are ignored. If more than one hit or more than one trigger are within one merged readout frame, all triggers are correlated with all hits.
This introduces a bias on higher rows, since there, large signals produce more crosstalk, so preferably smaller pulses not causing crosstalk are selected as seen in Fig. 9.1. Intrinsically, these signals have a worse timing.
ToT spectra are normalized to an integral of 1 while row and column projections are normalized for each row or column separately such that all entries for a row or column have an integral of 1. No thresholds are tuned in the studies in this chapter.

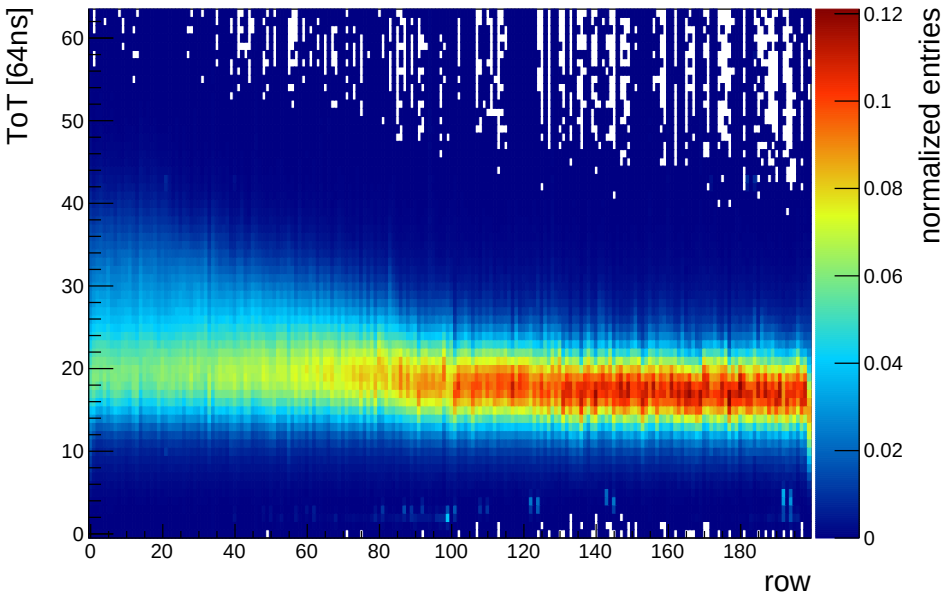

Figure 9.1: ToT row projection of a Sr90 source after cluster removal.

9.1 ToT Measurement and Readout Speed

First results unexpectedly showed no correlation between ToT and latency. An example is shown in Fig. 9.2. It was found that the ToT measurement depends on the speed of the readout state machine. An example is shown in Fig. 9.3 for Fe55. This is caused by the logic of the digital cell (Sec. 7.1.2) and the state machine (Sec. 7.1.4). As soon as the hit latch is set, the hit can be read out. TS2, however, can still be updated. If the second timestamp has latched and stored is not checked. That means the TS2 is the time the hit is read out so that the ToT corresponds to the time between the hit and the readout of the hit. To reduce the impact of this feature, the state machine speed is reduced by a factor 8 (*timerend* changed from 0x1 to 0xF). The register *slowdownend* is also set to 0xF to gain additional time. If no hits are found in a readout cycle, the state machine waits (1 + *slowdownend*) clocks before it starts a new cycle. The duration between cycles depending on the number of hits in the previous cycle is plotted in Fig. 9.4. The more hits are readout in a cycle, the longer it takes before the next cycle can start. As mentioned in Sec. 7.1.4, one cycle can not contain more than one hit in one column. Decreasing the state machine clock frequency also increases the number of hits per cycle due to the increased integration time. With this slowdown the probability of corrupted ToT data is only reduced.
This feature also complicates the treatment of clusters of any origin along the column. Hits in the higher rows can have a longer ToTs for evenly split charge. The ToT of the lower hit can be cut off if the hit happens close to a new readout cycle while the upper hit is read out a full cycle later. At this time, TS2 will be most likely sampled correctly.

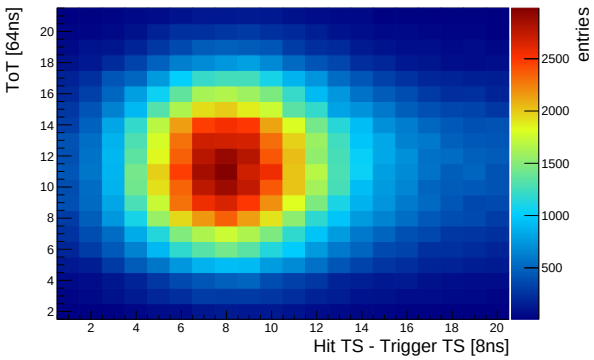

(a) Zoom in of the latency (Hit TS - Trigger) vs ToT.

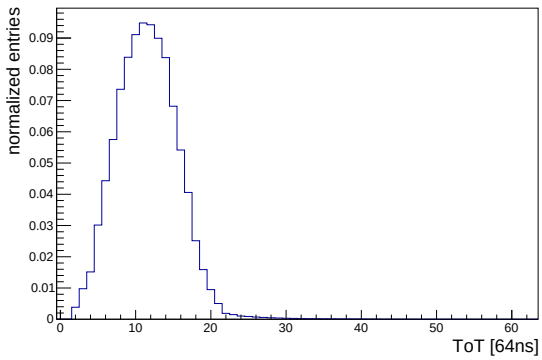

(b) ToT spectrum.

Figure 9.2: Latency vs ToT and ToT spectrum for an Sr90 source at full readout speed.

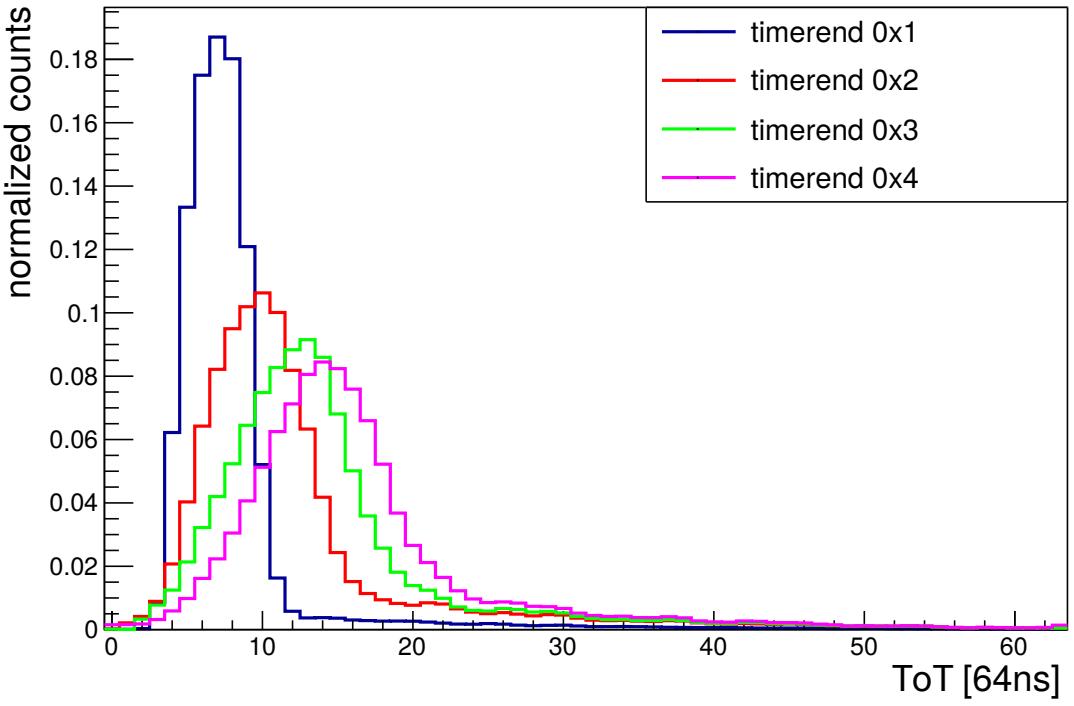

Figure 9.3: ToT for Fe55 depending on timerend.

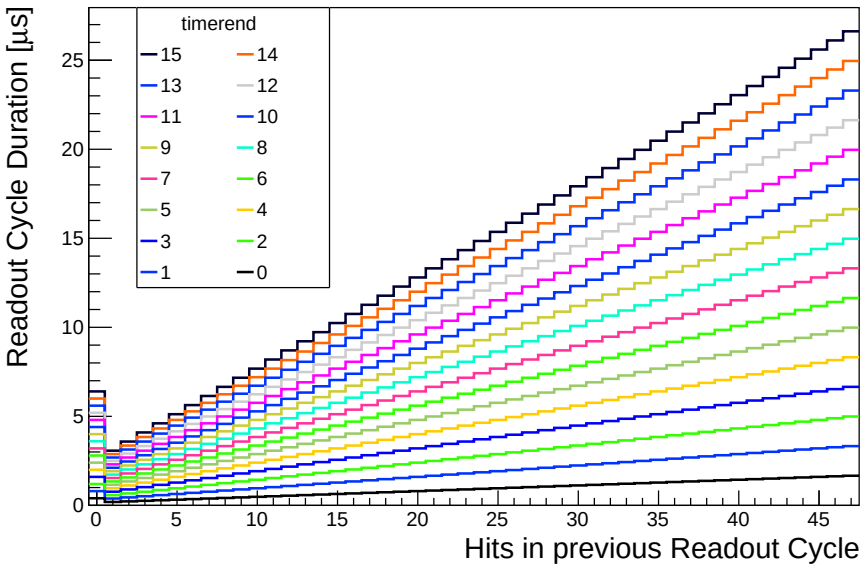

Figure 9.4: Duration between readout cycles depending on *timerend* and the number of columns with a hit. Reference clock speed is 125 MHz and *slowdownend*=0xf.

9.2 Signal Delay

Another feature which manifested up during the first tests is in the following referred to as "delay". Pixel with a higher column or row address have a larger latency as shown in Fig. 9.5 where pixel are grouped to gather statistics. The magnitude of this effect is unexpected since the columns are identical copies of each other and the signal propagation time from pixel with high row numbers to the digital cell should be less than 8 ns. A linear correction along both axes according to Eq. 9.1 is fitted to the latency averaged mean of the maximum plus 3 bins in both directions and used for delay correction. To increase statistics and compensate pixel variations, pixel are grouped in blocks of 6 columns by 8 rows. The resulting correction is the rounded to the nearest integer bin.

$$\text{Delay}(column, row) = \text{Offset} + \text{slope}_{column} \times column + \text{slope}_{row} timesrow \tag{9.1}$$

This effect is expected to be related to the voltage drop along the matrix which is suggested by Fig. 9.5 which shows a map of the block delays for different supply voltages. For 1.9 V the overall delay spread is reduced and the dependence on the column is decreased.

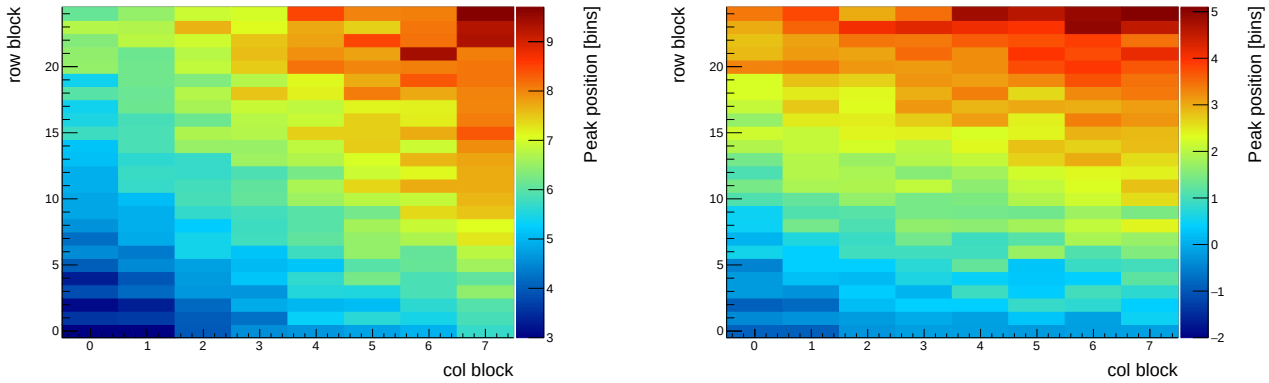

(a) VDD = VDDA = 1.8 V. (b) VDD = VDDA = 1.9 V.

Figure 9.5: Delay maps for different supply voltages in timestamp bins of 8 ns.

9.3 Time-Walk Correction

To correct the time-walk, a simple approach is used. All correlations of hits and triggers are histogrammed corresponding to their ToT. If a ToT bin has less 1000 entries, it is ignored due to the low significance and precision. Otherwise the maximum of the latency distribution is defined from the weighted average of the maximum bin and three bins to both sides of the maximum bin. This value is used to correct the latency, again rounded to the nearest integer bin after applying the delay correction. In total, the data is processed three times: once to calculate the delay correction, once for the TWC and the last time to apply both corrections. With this method the time resolution can be measured directly in the lab with a minimal setup and can be easily implemented on a frontend FPGA. The TWC is only calculated for the lower part of the chip where no crosstalk is visible to exclude the effect of the signal loss. It is then applied to the whole chip. The region with no significant crosstalk is defined for each chip and each setting. An example is shown in Fig. 9.6. While the ToT spectrum stays the same for all columns, the row projection reveals that the crosstalk sets in around row 40. The stripes in the row projection Fig. 9.6b are caused by a change in metal layers for the signal lines or different line spacing between two lines. Here, no triple crosstalk is possible which reduces the amount of short ToTs from crosstalk. Due to the normalization along the row, the crosstalk is less pronounced for these rows.
For each setting two analyses are performed. The first only includes the pixels which are used for the calculation of the TWC. The second is the result of applying the calculated TWC to the complete chip.
In total a very small lookup table with $1_{\text{delay offset}} + \#Rows + \#Columns + \#ToTs(64)$ entries are required for this correction method and the correction could be performed online. For matrix A of the MuPix8 only 313 entries are required using this scheme.
All of the measurements presented in this section are measured in the lab with a Sr90 source. An example of the correction steps is given in Fig. 9.7, where time-walk is shown as function of the latency versus the ToT before corrections in Fig. 9.7a, after delay correction in Fig. 9.7b and after time-walk correction in Fig. 9.7c.

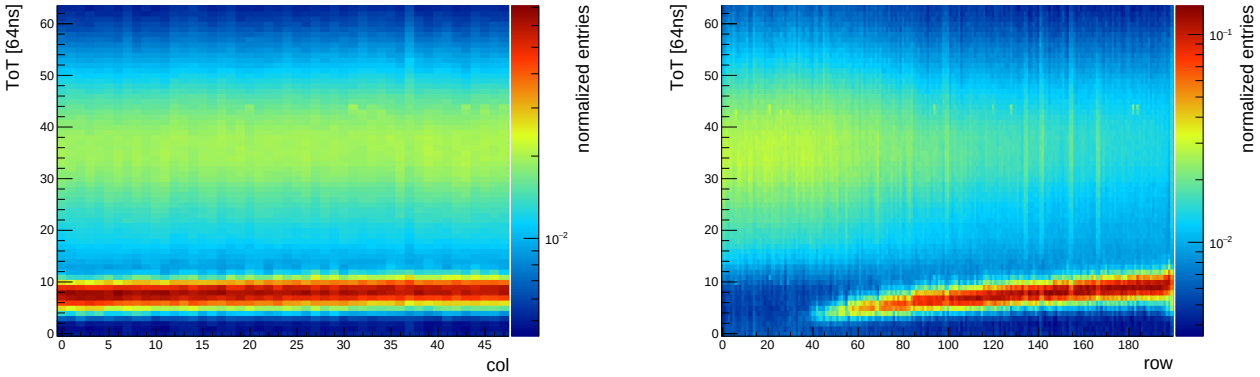

(a) ToT column projection.

(b) ToT row projection.

Figure 9.6: ToT projections for a Sr90 source without cluster removal.

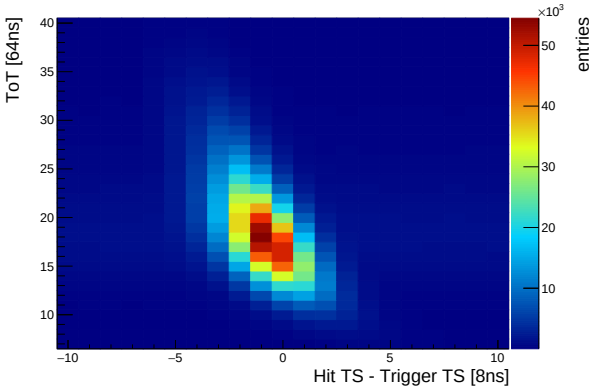

(a) Latency vs. ToT without corrections.

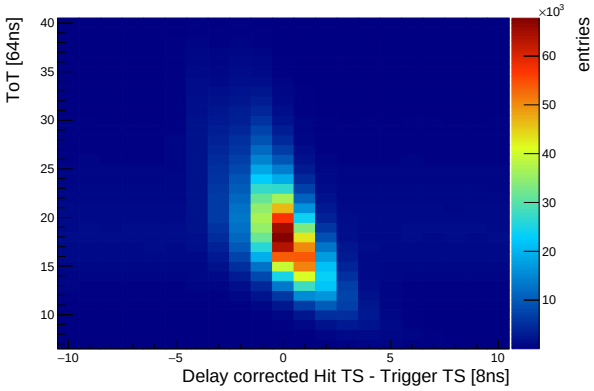

(b) Latency vs. ToT after delay correction.

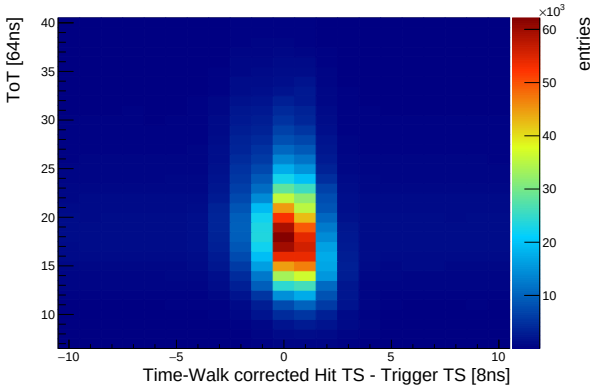

(c) Latency vs. ToT after delay and time-walk correction

Figure 9.7: Latency vs. ToT before and after corrections.

9.3.1 Background

The information of all single clusters and all triggers in a merged frame are correlated in this analysis. That means that a significant part of the latency distribution will be the correlation of random hits and triggers which do not originate from the same physical event. This creates a background given by two random variables of the same range (0 to 1023 or 10 bit). The distribution can be described by a triangle function, see Eq. 9.2, which only has one free scaling parameter A. An example of the correlated latency peak on on top of the random coincidences is show in Fig. 9.8. The fit function to obtain the time resolution, Eq. 9.3 is the sum of a Gaussian and and this background function.

$$f(x) = A \times (1023 - |x|) \tag{9.2}$$

$$f(x) = A \times (1023 - |x|) + B \times exp\left(\frac{-(x-\mu)^2}{2\sigma^2}\right) \tag{9.3}$$

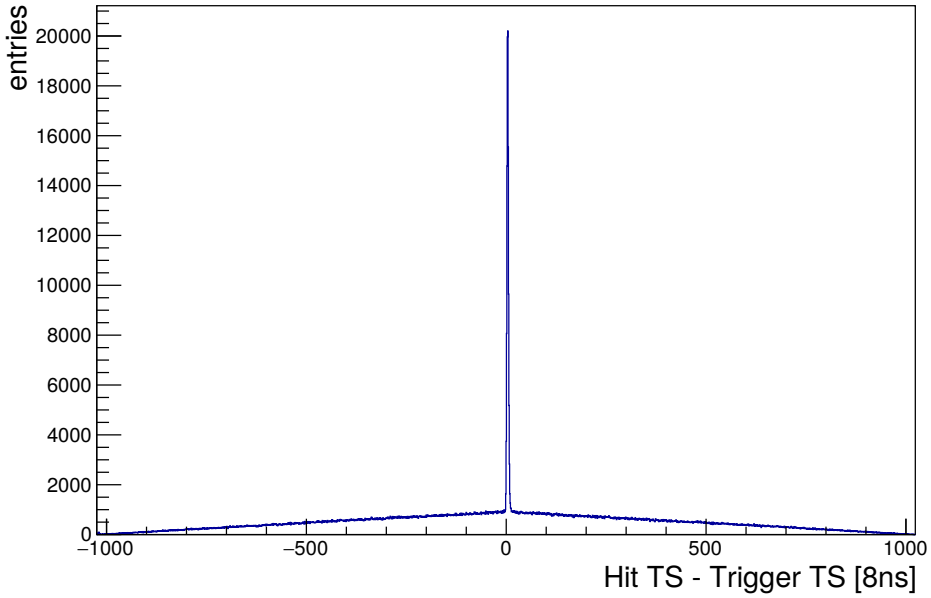

Figure 9.8: Typical histogram of the latency distribution.

9.4 Ramp Mode

During tests with the ramp mode TWC multiple issues with the implementation of this feature became apparent. Due to the current flowing into ThLow from the ramp circuit, the internal threshold is raised. To compensate this effect, the external ThLow has to be decreased. For calibration, one pixel is injected with an Fe55 gauged injection (0.25 V) and the hitbus is observed for different ThLow values. Two ThLow values were recorded for each VPRamp value, the threshold at which the injection can not be seen anymore and the threshold at which most of the injections are seen. Above a certain VPRamp value, not all injections are seen at any ThLow. The result of this measurement is shown in Fig. 9.9. The increased current is also dependent on the pixel address. While the ToT depends naturally on the row due to crosstalk, the column projections should be unaffected. However, the column projection in Fig. 9.10a shows both a drift and a dispersion of the ToT along the column. The row projection in Fig. 9.10b has a kink between row 80 and 120. Another spatial dependent effect is the fraction of hits which have TS2 0x3F, which means that they are most likely stuck and the input is most of the time above the threshold. This is shown in Fig. 9.11 where a clear gradient from top left to bottom right is visible. This means only small ramp values are usable as the dispersion can not be corrected.
In principle the ramp still works as can be seen in Fig. 9.12. The peak at small ToTs is caused by crosstalk, the peak at longer ToTs is due to the most probable energy deposition of the source. The ToT spectrum is more and more compressed as the ramp gets steeper.
For the measurements in this section no clusters are removed.

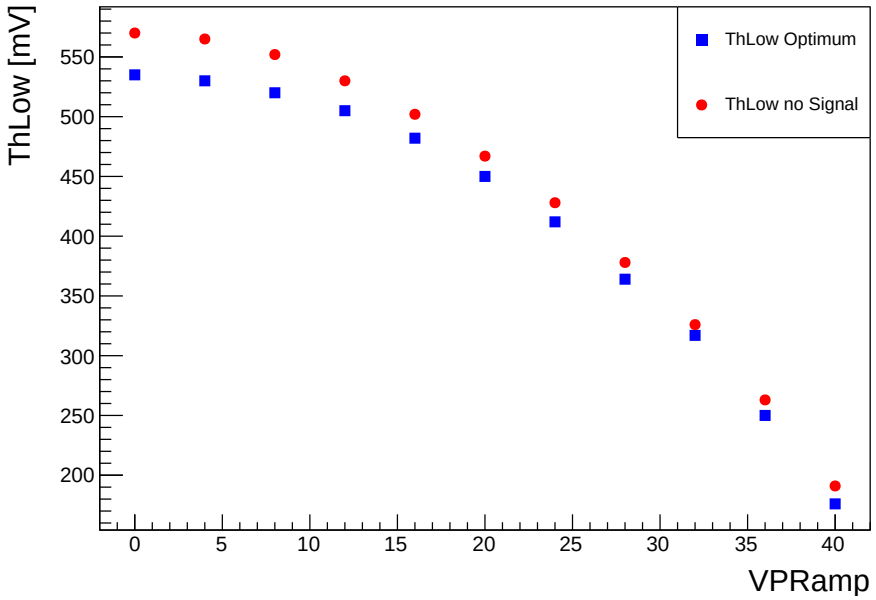

Figure 9.9: ThLow setting at which an Fe55 like injection can not be seen anymore (no Signal) and ThLow for which the most Fe55 like injections can be seen (Optimum) depending on VPRamp. For VPRamp greater than 20 not all injections can be seen at any ThLow.

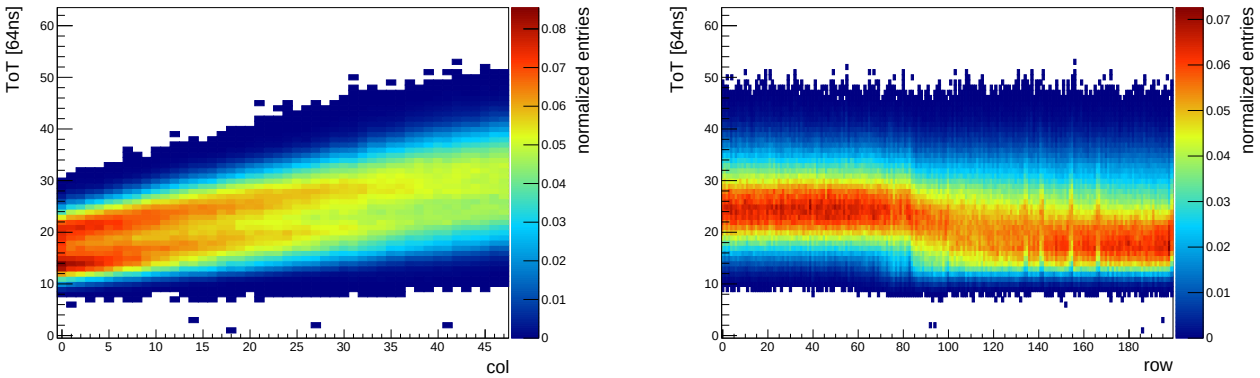

(a) ToT column projection for VPRamp 0x22.

(b) ToT row projection for VPRamp 0x22.

Figure 9.10: ToT projections for VPRamp 0x22.

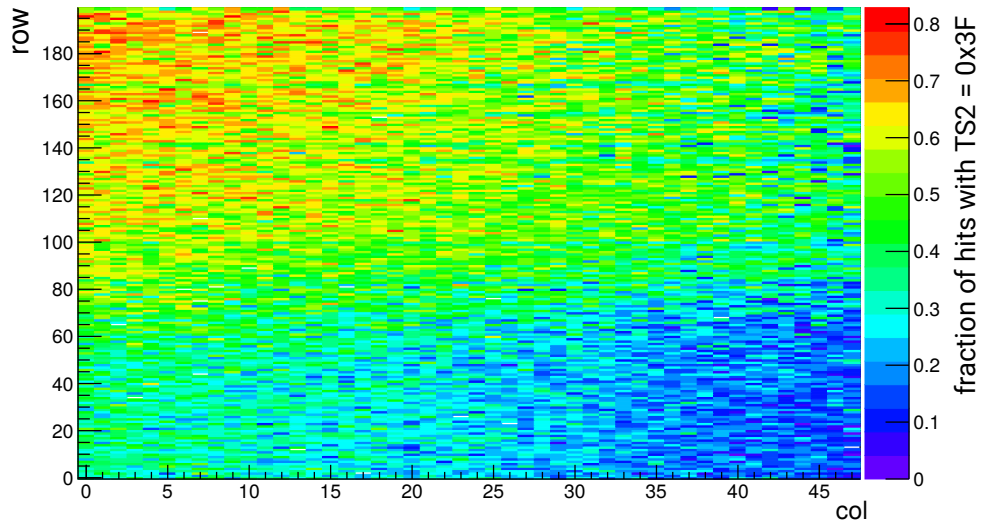

Figure 9.11: Map of the fraction of hits which had TS2 = 0x3F for VPRamp 0x20.

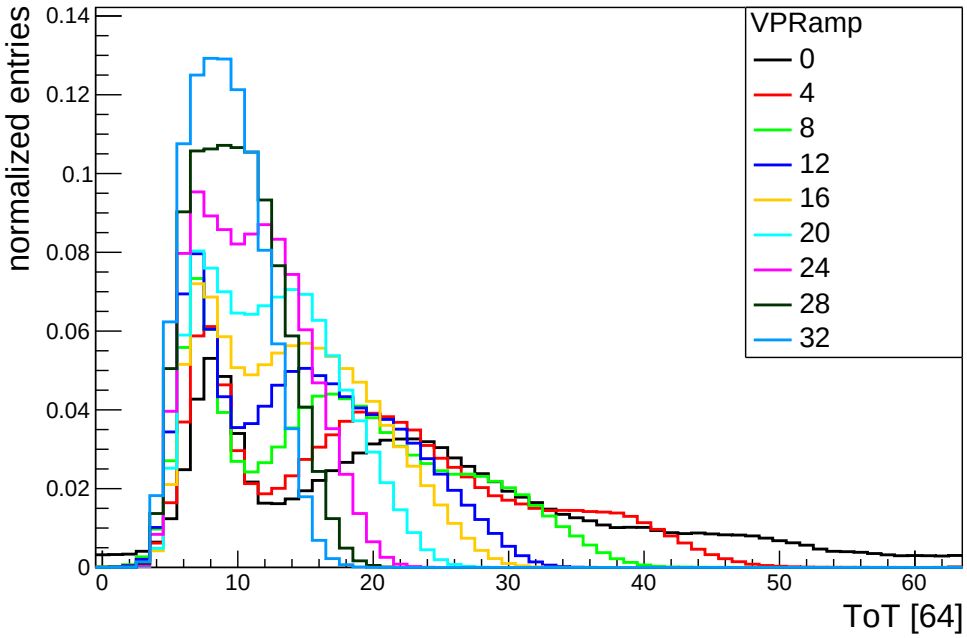

Figure 9.12: ToT spectrum of a Sr90 source for different VPRamp values. No clusters are removed.

9.5 VPComp Study

As described in Sec. 7.1.2, VPComp is the bias DAC for both comparators. The default value is 0x5 which allows for tuning and showed good performance for 1.8 V supply voltage [40]. The range of the tuning is reduced if VPComp is increased. For higher values the circuit showed a ringing behavior with some timestamp bits being on more often than others. This is likely a feature of the comparator as the TS bits are stored by a latch and not by the direct comparator output like the TS2 bits. However, higher values of VPComp showed that the time resolution could improve.
To test the VPComp dependence for 1.9 V supply voltage, is scanned for sensor 84-1-5 with the DAC values in Tab. B.3 at 60 V HV in the 2 Threshold mode with ThHigh = 550 mV and ThLow = 530 mV. The digital baseline is at 500 mV so the ThHigh is equivalent to half an Fe55 signal or roughly 800 electrons. The maximum row for the TWC is chosen at 35 since for this setting the crosstalk starts slightly before row 40, which can be seen in Fig. 9.13.
The time resolutions derived from the VPComp study are plotted in Fig. 9.14. A significant improvement of the time resolution from 11.5 ns to about 8.5 ns for the whole chip and from 10.5 ns to slightly below 8 ns for the lower part is shown. Even without a time-walk correction, 10 ns for the whole matrix is achieved. For the lower part, the time resolution after delay correction is sometimes slightly worse than the uncorrected distribution. This is due to the fact that with increasing VPComp value, the column dependence of the delay decreases non-linearly along the row. As example of the decreased column delay, the delay maps used for the correction of two VPComp values are shown Fig. 9.15. The delay correction for each measurement is derived from a fit the complete matrix which does not include the non-linearity.
The bit rates, the fraction of hits in which this bit is 1, for the VPComp values is plotted for TS1 in Fig. 9.16 and for TS2 in Fig. 9.17 from most significant bit (MSB) to least significant bit (LSB) as function of VPComp. Here, irregularities manifest for higher values which indicate that some part of the circuit oscillates which modulates the timestamps. For TS2 in Fig. 9.17 the rates never reach the expected 0.5. The reason for this is unknown but it could be related to the fact that the output of Comp2 has to drive the latches for the 6 RAM cells of TS2 and the hitbus. Unlike Fig. 9.14, which suggests a large plateau region for the time resolution, the bit distributions indicate a smaller range of viable values. From these considerations 18 (0x12) was chosen as new default value. This DAC value should also be scanned in a testbeam to search for influences on the efficiency. The effect on the tuning range should also be investigated as an increased VPComp value decreases the range of the tuning.

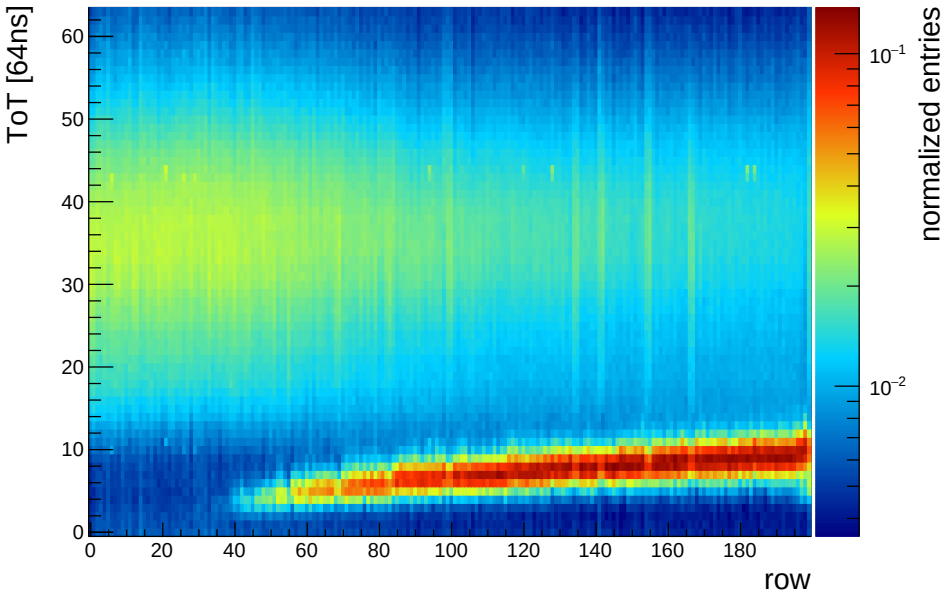

Figure 9.13: ToT row projection

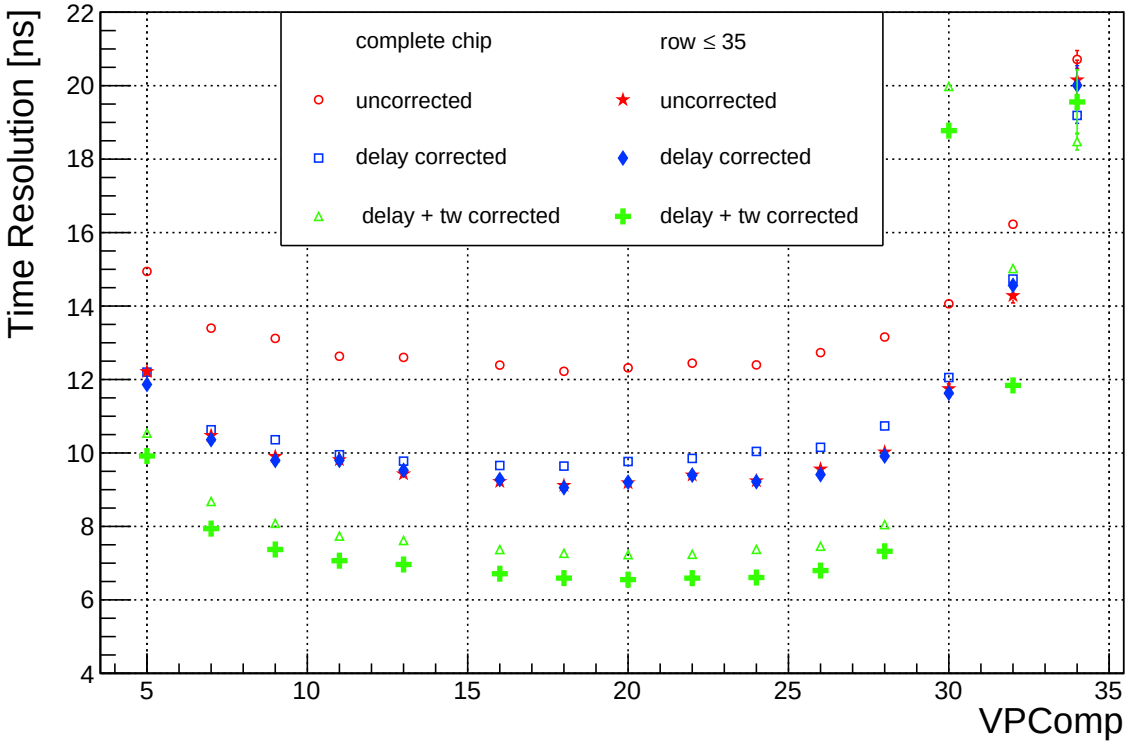

Figure 9.14: Time resolution depending on VPComp.

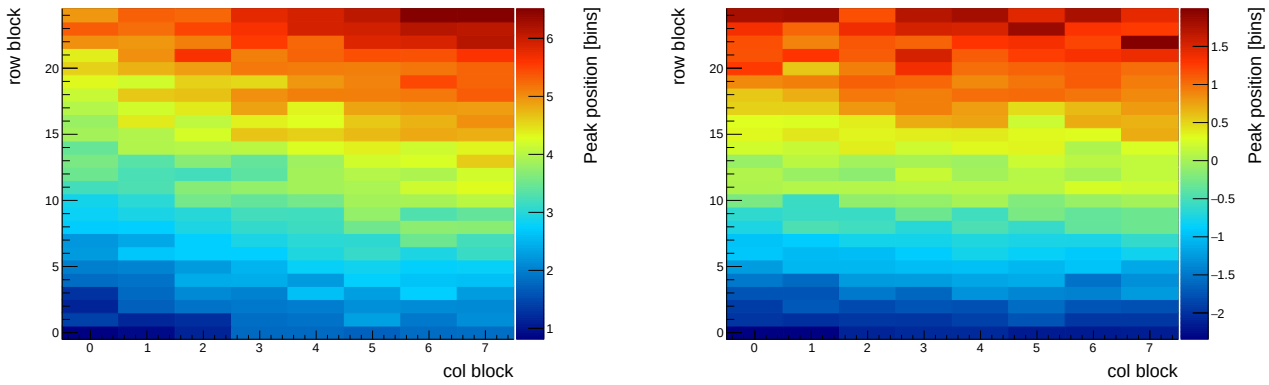

(a) VPComp = 5. (b) VPComp = 24.

Figure 9.15: Delay maps for different VPComp in bins of 8 ns.

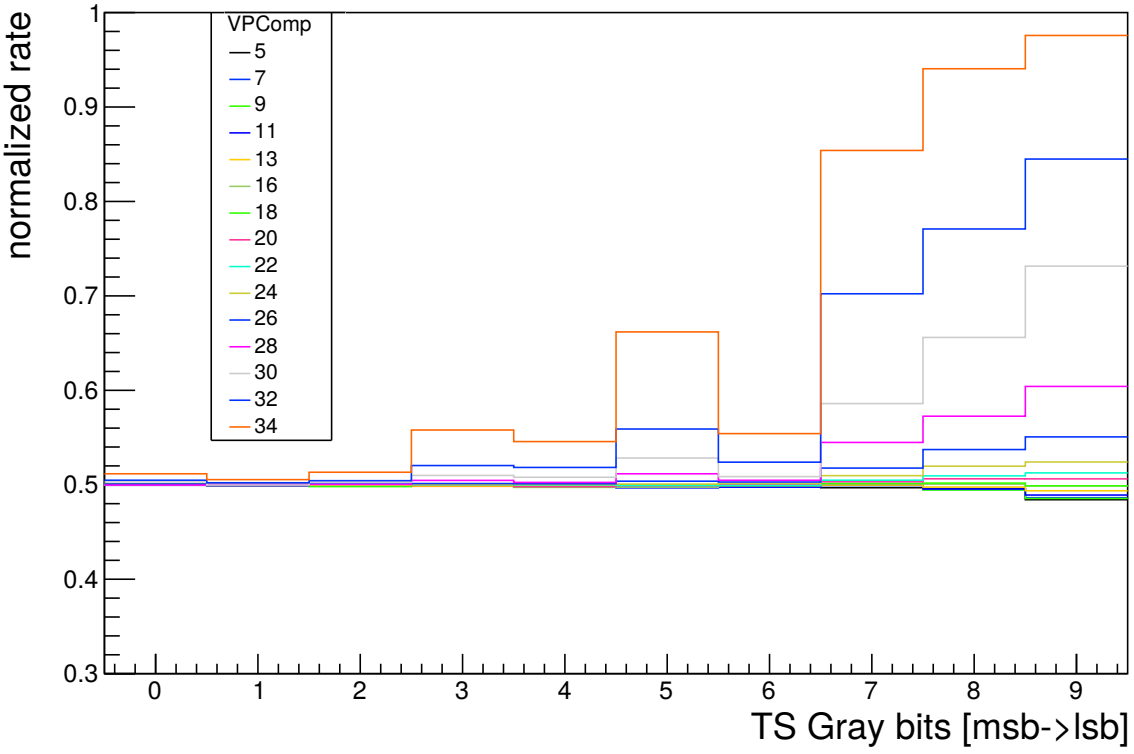

Figure 9.16: Bit frequencies of TS depending on VPComp.

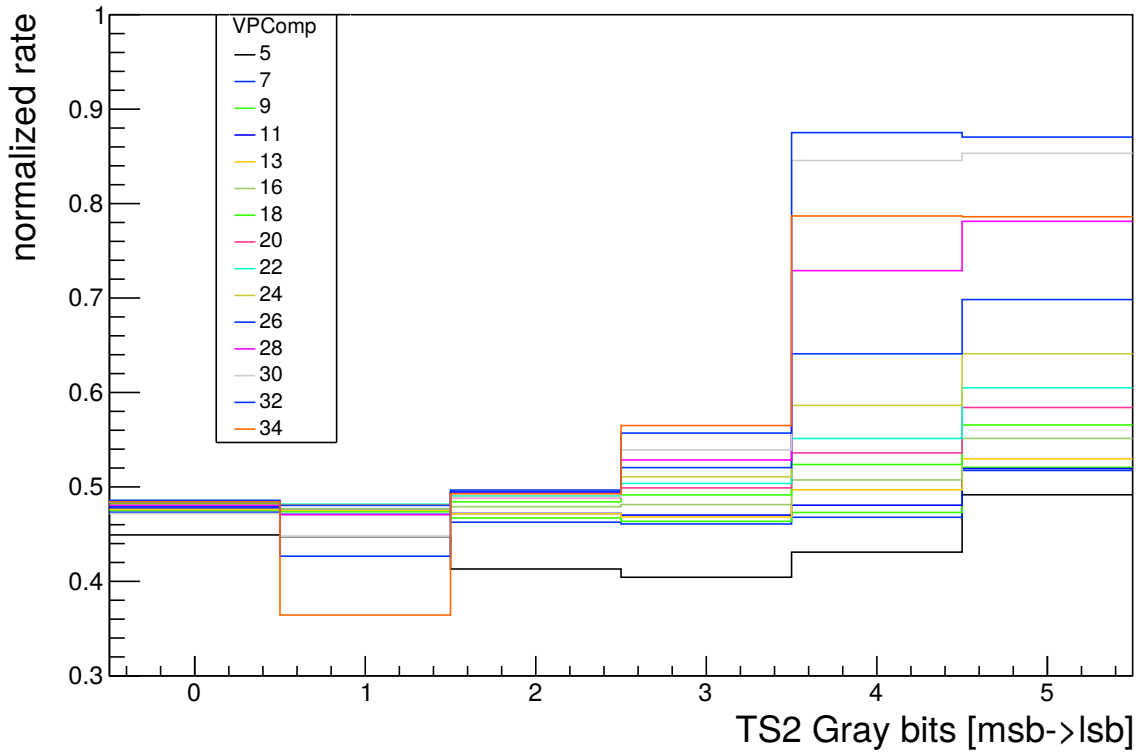

Figure 9.17: Bit frequencies of TS2 depending on VPComp.

9.6 VPLoadPix Study

In Sec. 8.4.7 VPLoadPix was found to significantly affect the rising edge of the signal pulse. This DAC is also scanned in the same way as VPComp in 9.5, sensor 84-1-5 with the DAC values in Tab. B.3 at 60 V HV in the 2Threshold mode with ThHigh = 550 mV and ThLow = 530 mV, with VPComp = 18 (0x12). The time resolutions derived in the VPLoadPix study is shown in Fig. 9.18. For this measurement, the maximum row for the time-walk corretion was chosen at 18 as for higher VPLoadPix values the crosstalk increases and starts to set in at lower rows as seen in Fig. 9.19. This is not surprising since neighboring signal lines have an approximate high pass characteristic so that faster rising signals also induce more voltage in the other signal line. Time resolutions for the complete chip of 7.5 ns and for the lower region sub 6 ns are achieved by applying both corrections. With just delay corrections resolutions below 9 ns are obtained for the full chip and below 8 ns for the bottom part.
Since Fig. 9.18 shows a large plateau of high time resolution, a lower value should be chosen considering that in Sec. 8.4.7 a drop in signal height is observed for larger values. Therefore VPLoadPix = 9 is chosen.
For this new setting (Tab. B.5) the chip has a power consumption of 199 mW cm^{-2} which is 10% larger than the power consumption of the default DACs (Tab. B.3) with 181 mW cm^{-2}. The maximum allowed heat dissipation of the pixel sensors for Mu3e is 400 mW cm^{-2}.

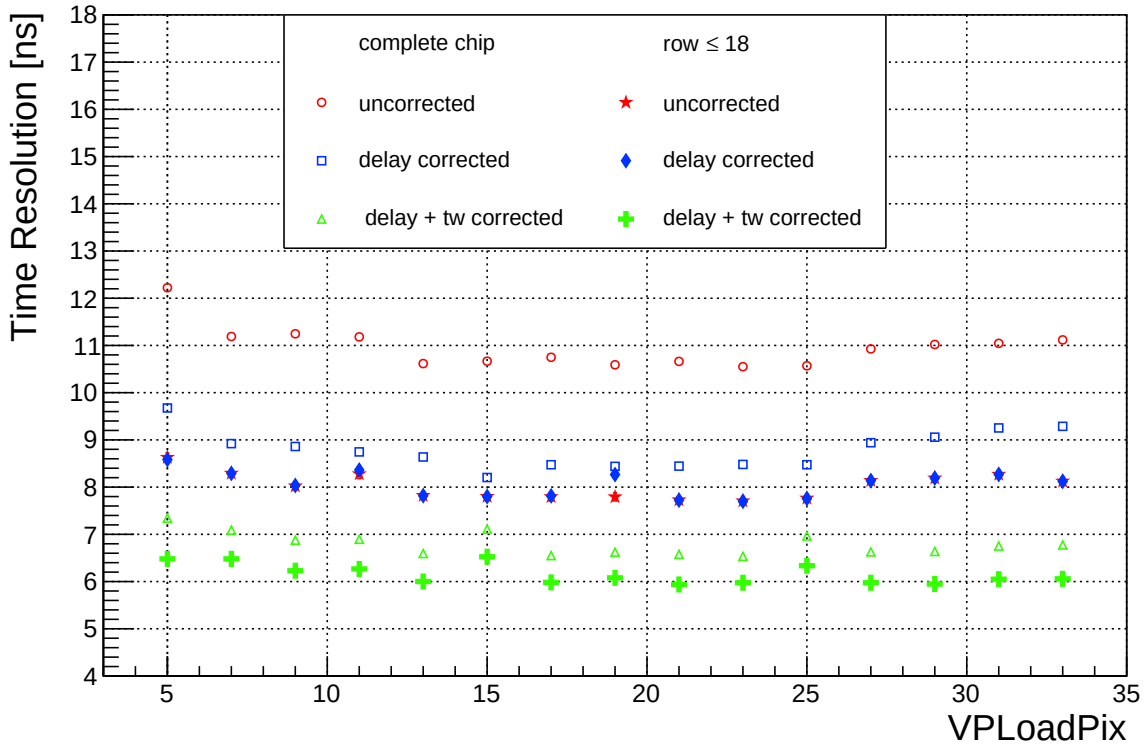

Figure 9.18: Time resolution depending on VPLoadPix.

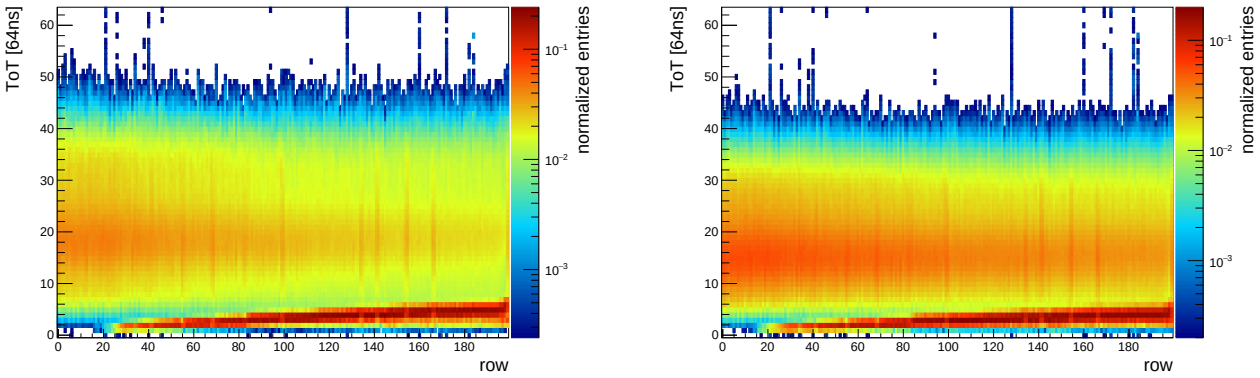

(a) VPLoadPix = 9.

(b) VPLoadPix = 31.

Figure 9.19: ToT row projections for different VPLoadPix.

9.7 DAC Optimization

As result of the measurements in Sec. 8.4 a new set of DACs (Tab. 8.1) was found to be a promising candidate for improving the time resolution. This new set is further optimized with the results of the VPComp and VPLoadPix optimization from the previous sections in Tab. 9.1. The settings are compared in Fig. 9.20 for sensor 84-1-5 at 60 V HV in the 2 Threshold mode with ThHigh = 550 mV and ThLow = 530 mV. Also VNFollPix is scanned, based on the indication of further improvement from Sec. 8.4. While the new DAC set performs better for the whole chip after TWC, the lower part performs worse. The decrease of VNFollPix however shows much better performance after TWC for the whole chip and a similar resolution for the lower part. Since these settings are far from what has been validated in testbeams they are not considered in the further sections but should be tested in the testbeam since they could decrease power consumption.

DAC	New Value [hex]	Default Value [hex]
VNPix	F	14
VNFBPix	4	A
VNFollPix	C	A
VPLoadPix	9	9
VNBiasPix	0	0
VNOutPix	A	A
BlResPix	5	5
VPComp	12	12

Table 9.1: New DAC set and defaults used for comparison.

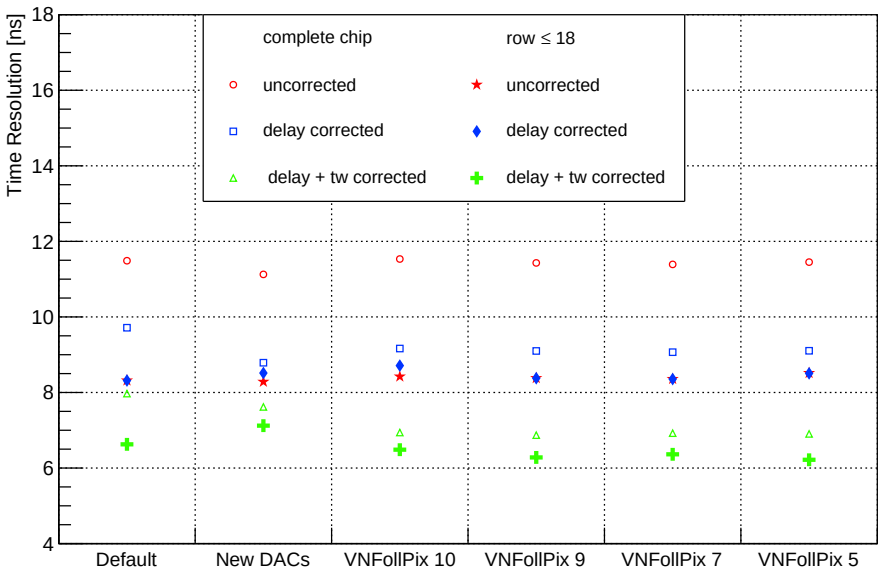

Figure 9.20: Time resolution for different DAC sets.

9.8 Comparison of different TWC Methods

For the previous measurements, only the 2 Threshold mode was used at fixed thresholds. ThLow has to be scanned for the optimal value for the time resolution. Is ThLow too close to the baseline timestamps from noise are stored. In Fig. 9.21 the time resolutions of sensor 84-1-5 at 60 V HV with ThHigh = 550 mV different ThLow values for the 2 Threshold method, ToT correction and the ramp method with different steepness are compared. This ThHigh value has shown high efficiency in testbeam measurements [40] and for ThHigh $<$ 550 mV most sensors start to get very noisy.
For the 2Thr method, a lower ThLow improves the uncorrected and delay corrected resolution minimally while the TWC does not improve much and gets even worse for a too low threshold. Here, the ToT is most likely too washed out by noise. The ToT method with a single threshold performs worse, initially and after delay correction, but is almost as good as the 2Thr method for the lower part of the sensor and as good for the whole chip. The best result for the lower rows after TWC is obtained for the 2Thr method at ThLow = 535 mV. The numbers are summarized in Tab. 9.2.
The ramp method behaves rather unexpected. Since the timestamp is saved by Comp1 for the ToT mode and the ramp mode, the uncorrected resolutions should be the same. While this is true for the lower part, the uncorrected resolution fluctuates for the whole chip. After delay correction the values are more compatible with each other. Due to the dispersion effects mentioned in Sec. 9.4, the TWC using the ramp method is worse for the whole chip than just a delay correction and the bottom region can not compete with the TWC results of the other methods. Possibly, the ramp takes too much power in the digital cell especially for higher rows, so that the other circuits are affected.

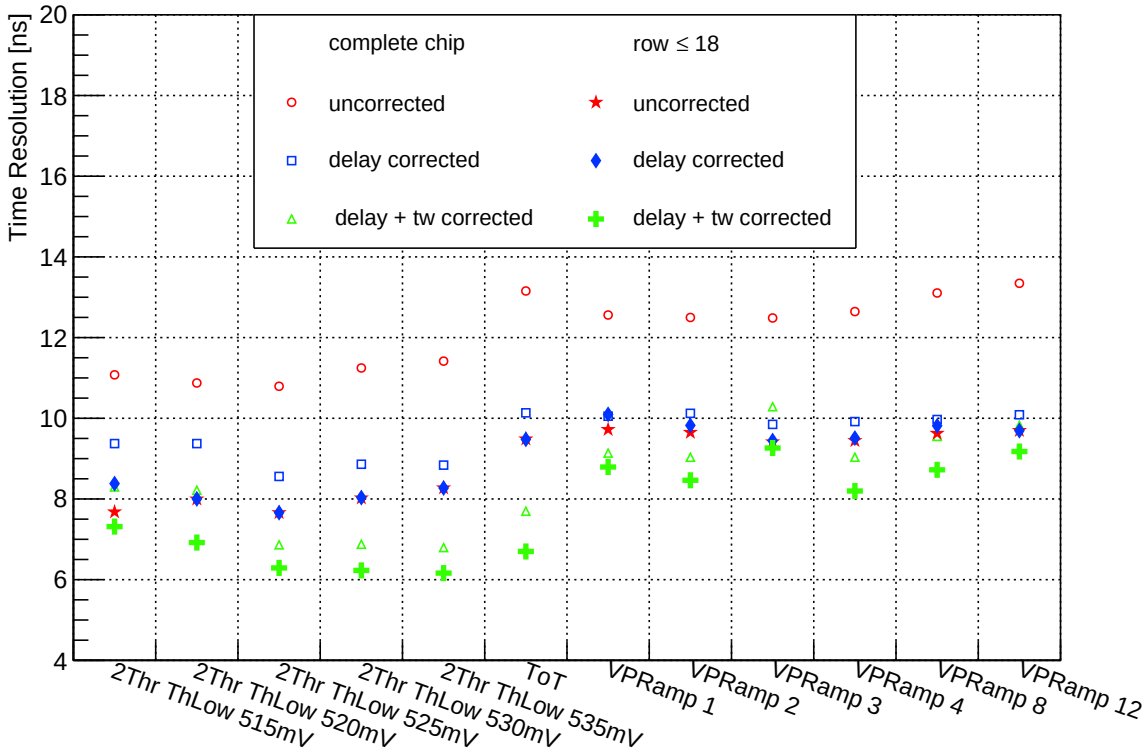

Figure 9.21: Time resolution for different TWC methods.

Correction	Time Resolution Complete Chip ns	Time Resolution Row $\leq$ 18 ns
uncorrected	11.42 ± 0.04	8.27 ± 0.09
delay	8.84 ± 0.03	8.27 ± 0.09
delay + time-walk	6.80 ± 0.02	6.16 ± 0.06

Table 9.2: Time Resolution for 2Thr ThLow 535 mV.

9.9 Single Pixel Resolution

For sensor 84-1-5 a large sample was taken at 60 with the DACs of the previous sections (DAC Set in Tab. B.5) in the 2 Threshold mode with ThHigh = 550 mV and ThLow = 525 mV. Single pixel latency distributions are fitted to determine the resolution after delay and time-walk correction. It should be noted that multiple files are combined for this study and the delay offset might vary slightly from file to file. Arrays of 4 by 4 pixel are used for the delay correction. Fig. 9.22a shows the result of a fit to pixel 0/0 which is (7.023 ± 0.628) ns while pixel 0/1 in Fig. 9.22b has (6.042 ± 0.544) ns resolution. Since the fits are automatized, not all fits converge. A χ^2_{red} cut and a cut on the number of the peak entries is performed. All passing fits are histogrammed in Fig. 9.23b where a Gaussian fit to the central part of the distribution shows an average time resolution of (6.381 ± 0.016) ns with a σ of (0.692 ± 0.015) ns. The long tail to worse time resolutions is likely due to the bias introduced by the cluster removal and low statistics for pixel with high crosstalk. The corrected resolutions are a significant improvement over the uncorrected case in Fig. 9.23a with (7.620 ± 0.020) ns and a σ of (1.072 ± 0.020) ns. The map of the corrected pixel time resolution in Fig. 9.24 shows a trend along the row direction but is also affected by large variations. After cluster removal not enough hits remain for the upper rows to fit.
Also, the quality of the delay correction can be tested. Fig. 9.25a shows the mean of the Gaussian contribution in the fits before delay correction but with TWC. The gradient from top to bottom is clearly visible despite the variations. In Fig. 9.25b the deviation of the fitted latency mean and the correction is shown which is mostly dominated by pixel variations even though there is a hint of a remaining small gradient. These corrected means are histogrammed in Fig. 9.26 to which a Gaussian fit is performed. With a mean of 3.2 ns the correction seems to work very well taking the 8 ns bin size into account. Since the Gaussian fits very well to the shape of the histogram, the deviations are most likely caused by pixel-to-pixel variations which are small with 3.9 ns. However, pixel-to-pixel variations make a sizable contribution to the overall time resolution. The correlation between the residual delay and the time resolution of the pixel is plotted in Fig. 9.27. Although it is smeared out, a slight correlation between the post correction delay and the time resolution is visible. This correlation indicates that the delay is a comparator feature as pixel with a higher latency have a worse time resolution.
The imperfect delay correction can not be the only explanation for the overall worse time resolution compared to the result for the same setting in Sec. 9.7. Assuming the delay variance and the intrinsic pixel time resolution add quadratically the overall time resolution should be 7.5 ns:

$$\sigma \approx \sqrt{6.4\,\mathrm{ns}^2 + 3.9\,\mathrm{ns}^2} \approx 7.5\,\mathrm{ns} \tag{9.4}$$

Fig. 9.28 shows a time resolution of (8.312 ± 0.008) ns which shows that the tails of the distributions still have a significant impact. This result is also worse than for other measurements with the same settings but less statistics. This is likely due to the mentioned effect that for each new run of data tacking the chip is reset and and may have a new phase to the reference clock. Other effects could be due the measurement duration, like a change in temperature of the sensor. With this in mind, the single pixel time resolution could be actually better the average time resolution of (6.381 ± 0.016) ns.

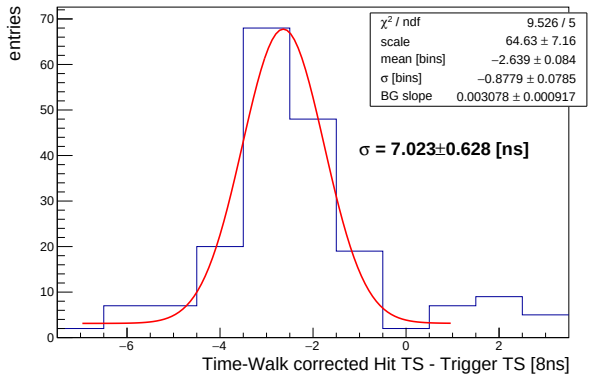

(a) Time resolution for pixel 0/0.

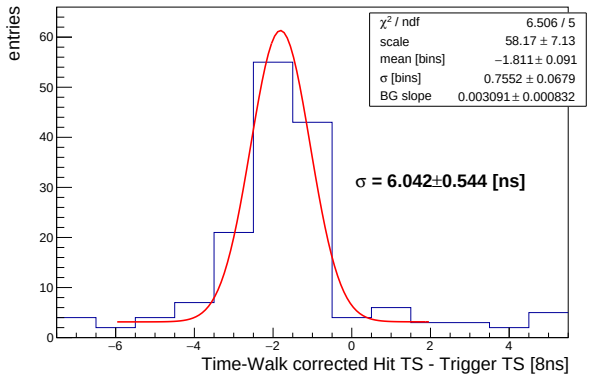

(b) Time resolution for pixel 0/1.

Figure 9.22: Time resolution for single pixel.

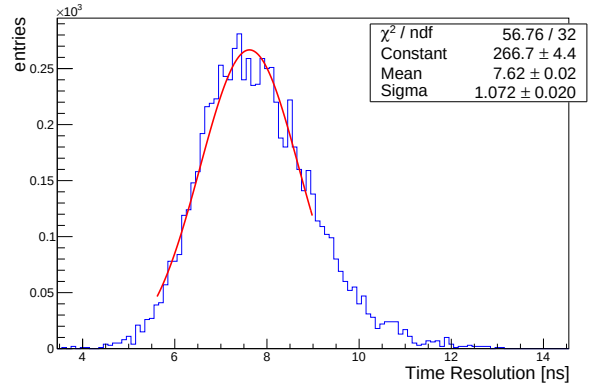

(a) Time resolution distribution before TWC.

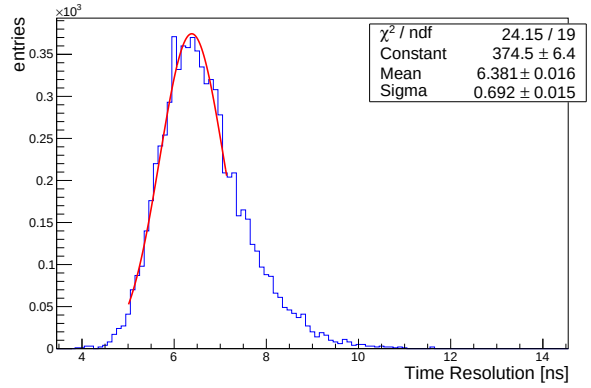

(b) Time resolution distribution after TWC.

Figure 9.23: Time resolution distributions before and after TWC.

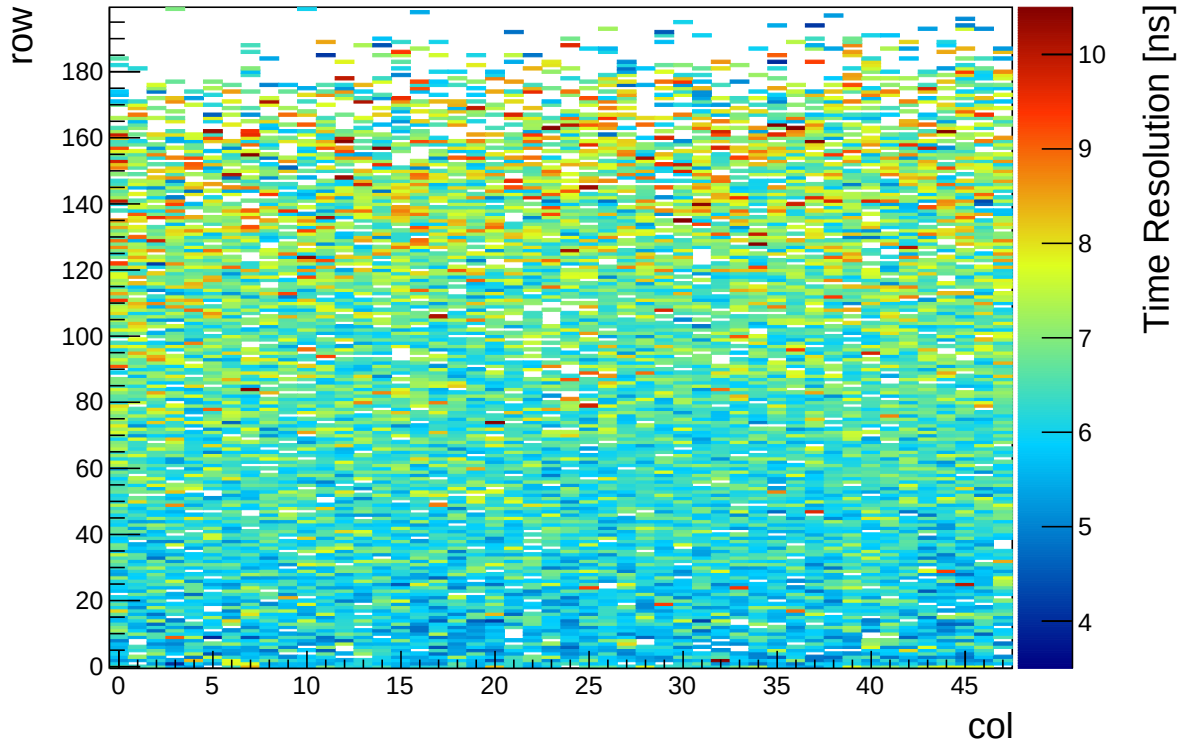

Figure 9.24: Time resolution map.

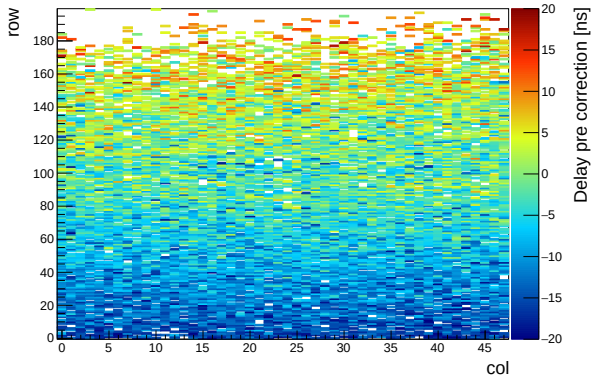

(a) Fitted latency mean before delay correction.

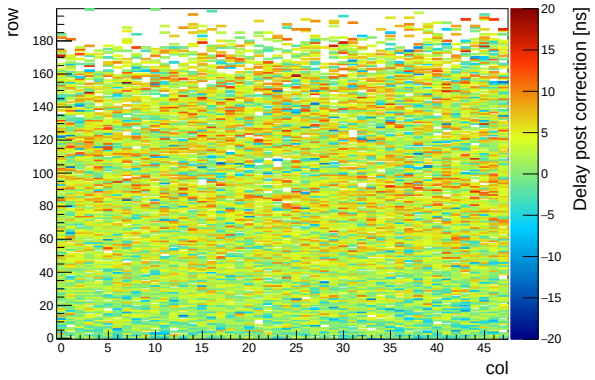

(b) Difference between fitted latency mean and delay correction.

Figure 9.25: Maps of the fitted latency mean of single pixel without and with delay correction.

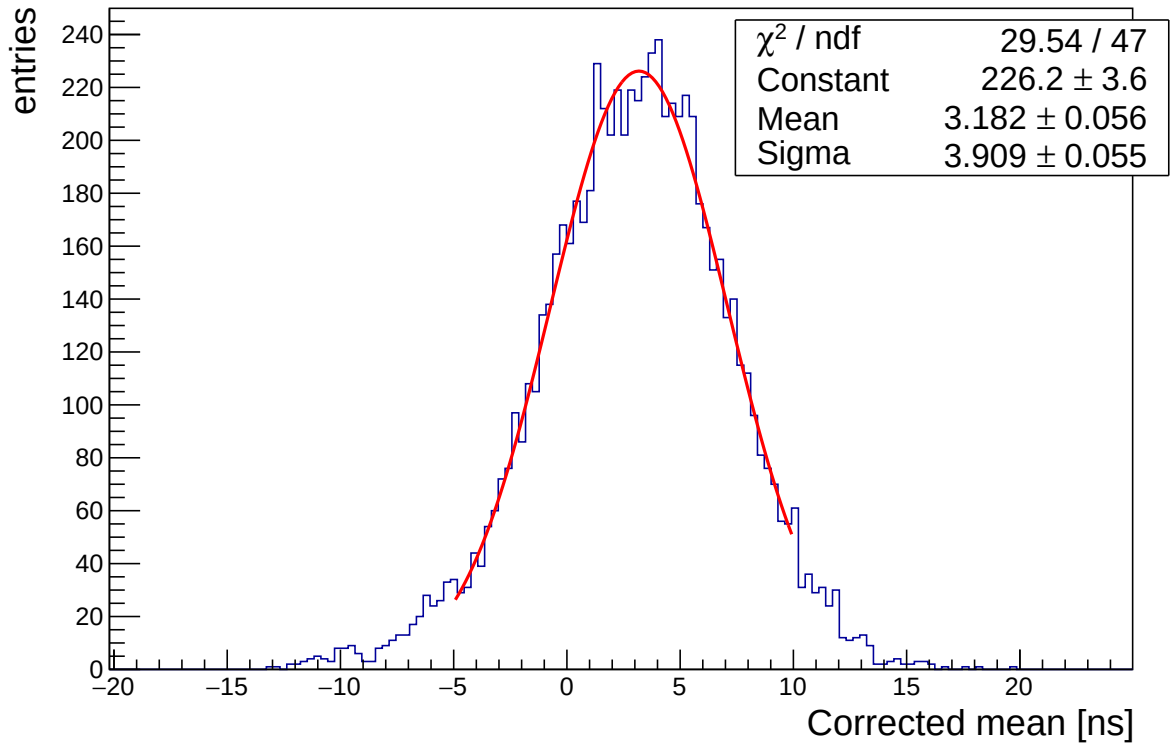

Figure 9.26: Histogram of the latency means after correction.

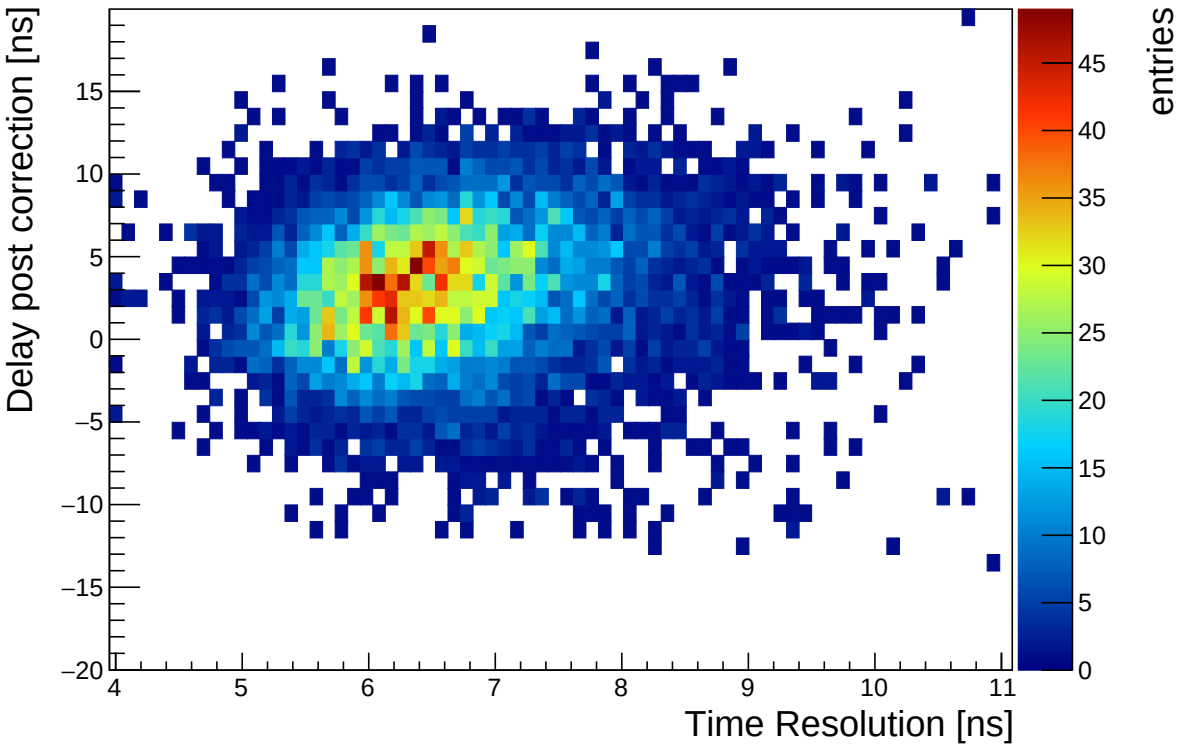

Figure 9.27: Histogram of the latency means after correction vs. time resolution.

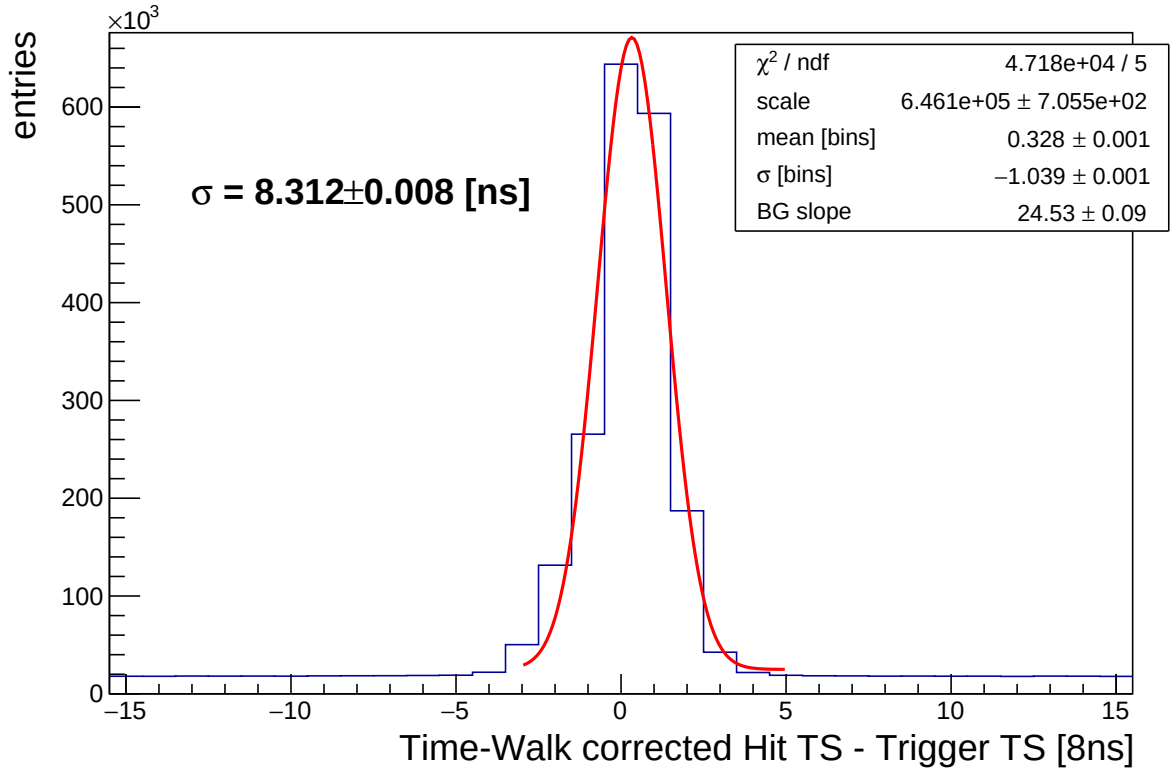

Figure 9.28: Latency distribution for the whole chip after delay and time-walk correction.

9.10 200 Ω cm Substrate Study

In the previous measurements only 80 Ω cm sensors were discussed. Since also sensors with an 200 Ω cm substrate were produced, the effect of an increased substrate resistivity which produces a higher signal due to larger depletion zone can be tested. For the change of 80 Ω cm to 200 Ω cm the signal is expected to be $\sqrt{200/80} \approx 1.6$ times larger. As sample, sensor 84-3-25 was chosen which is a final production sensor thinned to 100 µm. This sensor draws more current on the HV at 60 V than other sensors of both substrates, so the HV is set to 55 V where the current is comparable to other sensors. A study of this sensor with the same DAC settings as in Sec. 9.7 (Tab. B.5) is shown in Fig. 9.29 where different ThLow settings are used for the 2Thr method at ThHigh = 550 mV.
These results are very similar to the 80 Ω cm results of the previous sections. It seems that the limiting factor on the time resolution is not the signal but rather a limitation of the circuitry.
After TWC the whole chip has a time resolution of almost 7 ns which is the same as for the 80 Ω cm sensor in Fig. 9.21.
If thinning to 50 µm shows no negative impact on the performance for a 200 Ω cm substrate, this substrate could also be used for the next large prototype.

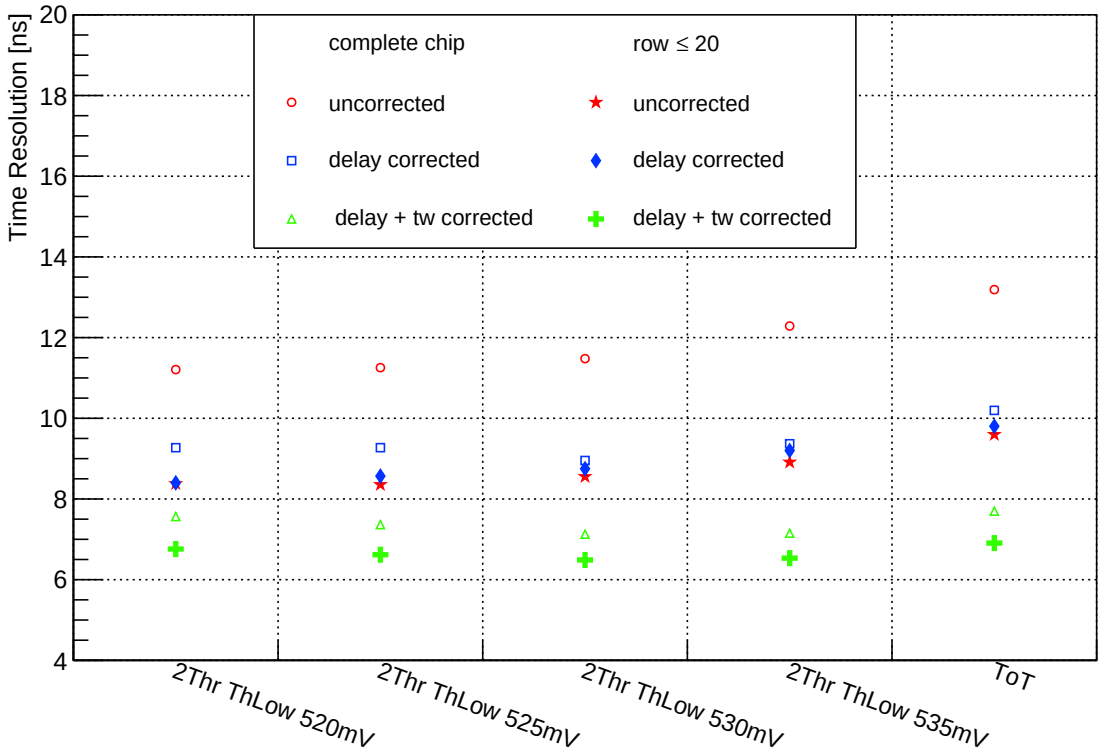

Figure 9.29: Time resolution for different ThLow settings of sensor 84-3-25.

Part IV

Discussion and Outlook

10 Summary & Conclusion

In this thesis the first large HV-MAPS prototype for the Mu3e experiment, the MuPix8, is characterized using test pulses and radioactive sources.
Beside the $10.8 \times 19.5\,\mathrm{mm}^2$ size compared to the previous small prototypes, this sensor contains a fully monolithic signal digitization and zero-suppressed readout. The MuPix8 is the first MuPix sensor to include circuits to reduce time-walk.
The analog response is studied as function of the bias settings and design parameters are validated. For the analog signal no dependence on the position in the matrix is found. The configuration settings are investigated with respect to the shaping parameters. Using these results first optimization of the settings is performed.
In the MuPix8, each pixel is connected to a digital partner cell. For pixel with long transmission lines, large crosstalk due to capacitive coupling is observed.
The Time-over-Threshold (ToT) measurement, which is implemented for each pixel, is used to correct the latency for varying pulses. A significant slowdown of the readout state machine is necessary to obtain correct ToTs. Three modes of ToT measurements implemented in this prototype are compared. The ramp mode is has only a moderate performance due to issues with the implementation. With the 2 Threshold mode, the comparator setting and an amplifier setting are optimized for time resolution. For the complete chip $(6.80 \pm 0.02)\,\mathrm{ns}$ are reached after time-walk correction using a simple lookup scheme. For the region of the chip without crosstalk $(6.16 \pm 0.06)\,\mathrm{ns}$ time resolution are achieved.
A large data sample is taken to investigate the time resolution of individual pixel. A Gaussian fit to the central part of the distribution shows a mean of $(6.38 \pm 0.02)\,\mathrm{ns}$ with a sigma of $(0.69 \pm 0.02)\,\mathrm{ns}$ after time-walk correction.
The intrinsic binning contribution of $8\,\mathrm{ns}/\sqrt{12}$ is not subtracted in these results.
The obtained time resolution agrees very well with the projected time resolution 5 ns.

11 Outlook

With the implementation of the MuPix8 most requirements of the Mu3e experiment are met. The power distribution and the signal transmission are critical and will be carefully addressed in the next design.
The implementation of the ToT measurement needs to be improved to allow reliable time-walk correction at fast readout speeds. Issues with the ramp mode implementation should be solved so that it can be reevaluated and compared to the other correction modes.
Individual adjustment of the thresholds can be used to compensate pixel variations and improve on the results obtained in this thesis.
The MuPix9 has been delivered, which is another small scale test chip. It contains circuits for serial powering and a new configuration scheme. For this chip also the amplifier was changed to allow even faster rising edges. Due to the smaller size, no power distribution issues are expected and an even better time resolution should be achievable.
From the delivered MuPix8 sensors, performance variation and yield issues were observed. To identify the issues, the MuPix7, a well characterized prototype, has been resubmitted to another vendor. Preliminary results of these recently delivered sensors agree well with the performance of the original submission.
Efforts on multiple fronts are made to converge in the production of the MuPix10. This sensor is planned to fulfill all requirements for phase I of the Mu3e experiment and can be used to fabricate first detector modules.

Part V

Appendix

A Silicon Properties

Property		Value	Unit
Atomic number	Z	14	
Nucleon number	28.09		
Density	ρ	2.33	g/cm^3
Crystal structure		Diamond	
Atom density		5.02×10^{22}	$1/cm^3$
Intrinsic charge density	n	1.5×10^{10}	$1/cm^3$
Dielectric constant	ϵ	11.9	
Band gap at 300K	indirect band gap	1.12	eV
	direct band gap	3.4	eV
Average creation energy for an electron-hole pair	ω	3.66	eV
Fano Factor	F	0.115	
Mobility	μ_n	1450	cm^2/sV
	μ_p	500	cm^2/sV

Table A.1: Important silicon properties [24, 58–62].

B DAC Values

DACs listed her only include the DACs which change the performance in the analog or digital cells. State machine DACs are explicitly stated if they are relevant in the context of the measurement.

B.1 84-2-6

80 Ω cm, preproduction, unthinned (≈ 725µm), AmpOut pixel 0/80, 1.8 V supply voltage

DAC	Value [hex]
VNPix	14
VNFBPix	10
VNFollPix	10
VPLoadPix	5
VNBiasPix	0
VNOutPix	10
BlResPix	5
VPComp	5
VNRegCasc	0
VPRegCasc	0
BlResDig	5
AlwaysEnable	1

Table B.1: DACs for chip 84-2-6.

B.2 84-2-3

80 Ω cm, preproduction, unthinned (≈ 725µm), 1.8 V supply voltage

DAC	Value [hex]
VNPix	14
VNFBPix	A
VNFollPix	A
VPLoadPix	5
VNBiasPix	0
VNOutPix	A
BlResPix	5
VPComp	5
VNRegCasc	0
VPRegCasc	0
BlResDig	A
AlwaysEnable	1

Table B.2: DACs for chip 84-2-3.

B.3 84-3-25

200 Ω cm, final production, thinned (≈ 100 µm), AmpOut pixel 0/100, 1.9 V supply voltage

DAC	Value [hex]
VNPix	14
VNFBPix	A
VNFollPix	A
VPLoadPix	5
VNBiasPix	0
VNOutPix	A
BlResPix	5
VPComp	5
VNRegCasc	0
VPRegCasc	0
BlResDig	5
AlwaysEnable	0

Table B.3: DACs for chip 84-3-25.

B.4 84-1-5

80 Ω cm, preproduction, unthinned (≈ 725µm), AmpOut pixel 0/100, 1.8 V supply voltage

DAC	Value [hex]
VNPix	14
VNFBPix	A
VNFollPix	A
VPLoadPix	5
VNBiasPix	0
VNOutPix	10
BlResPix	5
VPComp	5
VNRegCasc	14
VPRegCasc	14
BlResDig	A
AlwaysEnable	1

Table B.4: DACs for chip 84-1-5.

B.5 Time Resolution Comparison DACs

1.9 V supply voltage

DAC	Value [hex]
VNPix	14
VNFBPix	A
VNFollPix	A
VPLoadPix	9
VNBiasPix	0
VNOutPix	10
BlResPix	5
VPComp	12
VNRegCasc	0
VPRegCasc	0
BlResDig	5
AlwaysEnable	0

Table B.5: DACs for chip 84-1-5.

C Bibliography

[1] A. Blondel et al. "Research Proposal for an Experiment to Search for the Decay $\mu \to eee$". In: *ArXiv e-prints* (Jan. 2013). arXiv: 1301.6113 [physics.ins-det] (pp. 15, 21, 22).

[2] M. Tanabashi et al. "Review of Particle Physics". In: *Phys. Rev. D* 98 (3 Aug. 2018), p. 030001. DOI: 10.1103/PhysRevD.98.030001. URL: https://link.aps.org/doi/10.1103/PhysRevD.98.030001 (pp. 17, 19, 26, 28).

[3] S. L. Glashow. "Partial Symmetries of Weak Interactions". In: *Nucl. Phys.* 22 (1961), pp. 579–588 (p. 17).

[4] G. Aad et al. "Observation of a new particle in the search for the Standard Model Higgs boson with the ATLAS detector at the LHC". In: (2012). arXiv: 1207.7214 [hep-ex] (p. 17).

[5] S. Chatrchyan et al. "Observation of a new boson at a mass of 125 GeV with the CMS experiment at the LHC". In: *Phys.Lett.B* (2012). arXiv: 1207.7235 [hep-ex] (p. 17).

[6] Albert M Sirunyan et al. "Observation of Higgs boson decay to bottom quarks". In: *Phys. Rev. Lett.* 121.12 (2018), p. 121801. DOI: 10.1103/PhysRevLett.121.121801. arXiv: 1808.08242 [hep-ex] (p. 17).

[7] Tatsuya Masubuchi. "Measurements and Searches of Higgs boson decays to two fermions". In: 2018. arXiv: 1809.09011 [hep-ex] (p. 17).

[8] Q. R. Ahmad et al. "Measurement of the charged current interactions produced by B-8 solar neutrinos at the Sudbury Neutrino Observatory". In: *Phys. Rev. Lett.* 87 (2001), p. 071301. eprint: nucl-ex/0106015 (p. 18).

[9] Y. Fukuda et al. "Evidence for oscillation of atmospheric neutrinos". In: *Phys. Rev. Lett.* 81 (1998), pp. 1562–1567. eprint: hep-ex/9807003 (p. 18).

[10] F.P. An et al. "Observation of electron-antineutrino disappearance at Daya Bay". In: *Phys.Rev.Lett.* 108 (2012), p. 171803. DOI: 10.1103/PhysRevLett.108.171803. arXiv: 1203.1669 [hep-ex] (p. 18).

[11] G. Hernández-Tomé, G. López Castro, and P. Roig. "Flavor violating leptonic decays of τ and μ leptons in the Standard Model with massive neutrinos". In: (2018). arXiv: 1807.06050 [hep-ph] (pp. 18, 19).

[12] Wikimedia Commons. *Standard Model of Elementary Particles*. [Online; accessed 12-december-2014]. 2014. URL: http://upload.wikimedia.org/wikipedia/commons/0/00/Standard_Model_of_Elementary_Particles.svg (p. 18).

[13] Lorenzo Calibbi and Giovanni Signorelli. "Charged Lepton Flavour Violation: An Experimental and Theoretical Introduction". In: *Riv. Nuovo Cim.* 41.2 (2018), p. 1. DOI: 10.1393/ncr/i2018-10144-0. arXiv: 1709.00294 [hep-ph] (p. 20).

[14] J. Bernabeu, E. Nardi, and D. Tommasini. "μ - e conversion in nuclei and Z' physics". In: *Nucl. Phys.* B409 (1993), pp. 69–86. DOI: 10.1016/0550-3213(93)90446-V. arXiv: hep-ph/9306251 [hep-ph] (p. 20).

[15] Toshinori Mori. "Final Results of the MEG Experiment". In: *Nuovo Cim.* C39.4 (2017), p. 325. DOI: 10.1393/ncc/i2016-16325-7. arXiv: 1606.08168 [hep-ex] (p. 20).

[16] U. Bellgardt et al. "Search for the Decay $\mu^+ \to e^+e^+e^-$". In: *Nucl.Phys.* B299 (1988), p. 1. DOI: 10.1016/0550-3213(88)90462-2 (pp. 20, 21).

[17] William J. Marciano, Toshinori Mori, and J. Michael Roney. "Charged Lepton Flavor Violation Experiments". In: *Annual Review of Nuclear and Particle Science* 58.1 (2008), pp. 315–341. DOI: 10.1146/annurev.nucl.58.110707.171126. eprint: https://doi.org/10.1146/annurev.nucl.58.110707.171126. URL: https://doi.org/10.1146/annurev.nucl.58.110707.171126 (p. 21).

[18] Mu3e collaboration. "Mu3e Technical Design Report". In: (2017) (pp. 24, 54).

[19] F. Berg. "CMBL - A High-intensity Muon Beam Line & Scintillation Target with Monitoring System for Next-generation Charged Lepton Flavour Violation Experiments". PhD thesis. ETH Zürich, 2017 (p. 24).

[20] *Large Research Facilites.* [Online; accessed 30-september-2018]. 2018. URL: https://www.psi.ch/science/large-research-facilities (p. 24).

[21] J. Ashkin H. A. Bethe. "Passage of radiation through matter". In: *Nucl. P* 1 (1953), p. 253 (p. 25).

[22] S. M. Seltzer and M. J. Berger. "Improved Procedure for Calculating the Collision Stopping Power of Elements and Compounds for Electrons and Positrons". In: *The International Journal of Applied Radiation and Isotopes* 35 (1984) (p. 27).

[23] H.Augustin. "Characterization of a novel HV-MAPS Sensor with two Amplification Stages and first examination of thinned MuPix Sensors". Master Thesis. Heidelberg University, 2014 (p. 27).

[24] Helmuth Spieler. *Semiconductor detector systems.* eng. Repr. Series on semiconductor science and technology ; 12 ; Oxford science publications ; Series on semiconductor science and technology. Oxford [u.a.]: Oxford Univ. Press, 2008 (pp. 32, 36, 111).

[25] Wikimedia Commons. *PN-junction equilibrium.* accessed 10 July 2015. 2014. URL: https://upload.wikimedia.org/wikipedia/commons/d/d6/Pn-junction-equilibrium.png (p. 33).

[26] Gianluca Aglieri Rinella. "The ALPIDE pixel sensor chip for the upgrade of the ALICE Inner Tracking System". In: *Nuclear Instruments and Methods in Physics Research Section A: Accelerators, Spectrometers, Detectors and Associated Equipment* 845 (2017). Proceedings of the Vienna Conference on Instrumentation 2016, pp. 583 –587. DOI: https://doi.org/10.1016/j.nima.2016.05.016. URL: http://www.sciencedirect.com/science/article/pii/S0168900216303825 (p. 35).

[27] I. Perić. "A novel monolithic pixelated particle detector implemented in high-voltage CMOS technology". In: *Nucl.Instrum.Meth.* A582 (2007), p. 876. DOI: 10.1016/j.nima.2007.07.115 (p. 36).

[28] D. Immig. "Charakterisierung des VCO, der PLL und der Pulsform des MuPix7 in Abhängigkeit der Umgebungstemperatur". Bachelor Thesis. Heidelberg University, 2016 (p. 41).

[29] Martin Müller. "Effizienz eines HV-MAP Sensors auf niederenergetische Photonen". Bachelor Thesis. Mainz University, 2016 (p. 41).

[30] D. vom Bruch. "Pixel Sensor Evaluation and Online Event Selection for the Mu3e Experiment". PhD thesis. Heidelberg University, 2017 (p. 41).

[31] K. Simmoteit. "Development of an X-Ray based Energy Calibration Method for High Voltage Monolithic Active Pixel Sensors". Bachelor thesis. Heidelberg University, 2015 (p. 41).

[32] Johannes Grimm. "Measurements of the Signal to Noise Ratio of High Voltage Monolithic Active Pixel Sensors and Simulation Studies for Timewalk Correction". Bachelor Thesis. Department of Physics and Astronomy University of Heidelberg, 2017 (pp. 41, 48).

[33] I.Peric, A.Weber. *Documentation MuPix8*. Internal Document (pp. 41, 48, 61).

[34] Heiko Augustin. Private Communication (pp. 42, 48).

[35] F. Gray. *Pulse code communication*. US Patent 2,632,058. 1953. URL: http://www.google.com/patents/US2632058 (p. 45).

[36] J. Kroeger. "Readout Hardware for the MuPix8 Pixel Sensor Prototype and a Firmware-based MuPix8 Emulator". Master Thesis. Heidelberg University, 2017 (pp. 48, 52).

[37] N. Berger. *MUPIX8 Data Format*. Mu3e internal note 0024, Version 0.2. 2018 (p. 48).

[38] Sebastian Dittmeier. "Fast data acquisition for silicon tracking detectors at high rates". PhD thesis. Heidelberg University, 2018 (pp. 48, 53).

[39] *AMS AG, Tobelbader Strasse 30, 8141 Unterpremstaetten (Austria)* (p. 49).

[40] Lennart Huth. "A High Rate Testbeam Data Acquisition System and Characterization of High Voltage Monolithic Active Pixel Sensors". PhD thesis. Heidelberg University, 2018 (pp. 49, 53, 65, 89, 95).

[41] D. Wiedner. *The Mupix8 PCB*. Mu3e Internal Note 42 (p. 52).

[42] Altera Coropration. *Stratix IV GX FPGA Development Board - Refernce Manual*. 9.1.0. 2012 (p. 53).

[43] *PCI Express Base Specification*. Revision 3.1. PCI SIG, 2014 (p. 53).

[44] L. Huth. "Development of a Tracking Telescope for Low Momentum Particles and High Rates consisting of HV-MAPS". Master thesis. Heidelberg University, 2014 (p. 53).

[45] *Iron-55 on wikipedia*. Online - accessed 10.10.2018. URL: https://en.wikipedia.org/wiki/Iron-55 (p. 54).

[46] *Sr-90 on wikipedia*. Online - accessed 10.10.2018. URL: https://en.wikipedia.org/wiki/Strontium-90 (p. 54).

[47] Saint-Gobain Crystals. *BC-400,BC-404,BC-408,BC-412,BC-416 Datasheet*. [Online; accessed 15.09.2018]. URL: https://www.crystals.saint-gobain.com/sites/imdf.crystals.com/files/documents/bc400-404-408-412-416-data-sheet.pdf (p. 54).

[48] Hamamatsu Photonics K.K. *S13360 Series Datasheet*. [Online; accessed 14.09.2018]. URL: https://www.hamamatsu.com/resources/pdf/ssd/s13360_series_kapd1052e.pdf (p. 54).

[49] Sebastian Dittmeier. Private Communication (p. 55).

[50] Tektronix. *MSO70000C/DX Series Mixed Signal Oscilloscopes DPO70000C/DX Series Digital Phosphor Oscilloscopes DPO7000C Series Digital Phosphor Oscilloscopes MSO5000B and DPO5000B Series Oscilloscopes User Manual*. [Online; accessed 08.10.2018]. URL: https://www.tek.com/oscilloscope/dpo70000-mso70000-manual/mso70000dx-dpo70000dx-mso70000c-dpo70000c-dpo7000c-mso5000b-0 (pp. 55, 59).

[51] Dmitri Denisov, Valery Evdokimov, Strahinja Lukić, and Predrag Ujić. "Test beam studies of the light yield, time and coordinate resolutions of scintillator strips with WLS fibers and SiPM readout". In: *Nuclear Instruments and Methods in Physics Research Section A: Accelerators, Spectrometers, Detectors and Associated Equipment* 848 (2017), pp. 54 –59. DOI: https://doi.org/10.1016/j.nima.2016.12.043. URL: http://www.sciencedirect.com/science/article/pii/S0168900216313110 (p. 55).

[52] Tektronix. *MSO4000 and DPO4000 Series Digital Phosphor Oscilloscopes User Manual*. [Online; accessed 08.10.2018]. URL: https://www.tek.com/oscilloscope/dpo4054-manual/mso4000-and-dpo4000-series-0 (p. 59).

[53] H. Augustin. *The Path towards MuPix8: Lab Observations/Desired Features/Summary of the Design Status*. Mu3e Internal Note 25 (p. 64).

[54] H. Augustin et al. "MuPix7—A fast monolithic HV-CMOS pixel chip for Mu3e". In: *Journal of Instrumentation* 11.11 (2016), p. C11029. URL: http://stacks.iop.org/1748-0221/11/i=11/a=C11029 (p. 65).

[55] Alena Weber. “Entwurf eines Pixelsensorchips für die Teilchenphysik”. Master Thesis. Institut für Prozessdatenverarbeitung und Elektronik (IPE), Karlsruher Institut für Technologie (KIT), 2016 (p. 65).

[56] R. Hagdorn. “Performance Optimization of the MuPix7 Sensor Prototype”. Master thesis. Heidelberg University, 2017 (p. 77).

[57] Heiko Augustin et al. “Efficiency and timing performance of the MuPix7 high-voltage monolithic active pixel sensor”. In: *Nuclear Instruments and Methods in Physics Research Section A: Accelerators, Spectrometers, Detectors and Associated Equipment* 902 (2018), pp. 158 –163. DOI: https://doi.org/10.1016/j.nima.2018.06.049. URL: http://www.sciencedirect.com/science/article/pii/S016890021830771X (p. 79).

[58] J.C. Ashley. “Energy loss rate and inelastic mean free path of low-energy electrons and positrons in condensed matter”. In: *Journal of Electron Spectroscopy and Related Phenomena* 50.2 (1990), pp. 323 –334. DOI: http://dx.doi.org/10.1016/0368-2048(90)87075-Y. URL: http://www.sciencedirect.com/science/article/pii/036820489087075Y (p. 111).

[59] Martin A. Green. “Intrinsic concentration, effective densities of states, and effective mass in silicon”. In: *Journal of Applied Physics* 67.6 (1990), pp. 2944–2954. DOI: http://dx.doi.org/10.1063/1.345414. URL: http://scitation.aip.org/content/aip/journal/jap/67/6/10.1063/1.345414 (p. 111).

[60] B.G. Lowe and R.A. Sareen. “A measurement of the electron-hole pair creation energy and the Fano factor in silicon for 5.9keV X-rays and their temperature dependence in the range 80-270K”. In: *Nuclear Instruments and Methods in Physics Research Section A: Accelerators, Spectrometers, Detectors and Associated Equipment* 576 (2007), pp. 367 –370. DOI: http://dx.doi.org/10.1016/j.nima.2007.03.020. URL: http://www.sciencedirect.com/science/article/pii/S016890020700527X (p. 111).

[61] H. Philipp and E. Taft. “Optical Constants of Silicon in the Region 1 to 10 ev”. In: *Phys. Rev.* 120 (1 Oct. 1960), pp. 37–38. DOI: 10.1103/PhysRev.120.37. URL: http://link.aps.org/doi/10.1103/PhysRev.120.37 (p. 111).

[62] F. Scholze, H. Henneken, P. Kuschnerus, H. Rabus, M. Richter, and G. Ulm. “Determination of the electron-hole pair creation energy for semiconductors from the spectral responsivity of photodiodes”. In: *Nuclear Instruments and Methods in Physics Research Section A: Accelerators, Spectrometers, Detectors and Associated Equipment* 439.2-3 (2000), pp. 208 –215. DOI: http://dx.doi.org/10.1016/S0168-9002(99)00937-7. URL: http://www.sciencedirect.com/science/article/pii/S0168900299009377 (p. 111).

Acknowledgments

This page is dedicated to the people who helped me and supported me in the years it took me to get this far.

First, I want to thank Prof. André Schöning for giving me the opportunity to work in such an amazing group and for a fascinating experiment.

My sincerest thanks to the second examiner of my thesis.

A big thank you to Heiko Augustin and Lennart Huth for supervising and supporting me during this thesis and beyond.

I am deeply in debt to the people who reviewed my thesis:
Sebastian, David, Heiko, Adrian, Lennart, Frank and Dirk.
Without your support, this thesis would be even more confusing and diffuse.

My thanks also go to all the current and past member of the Mu3e group in Heidelberg for the amazing years since I joined.

I want to include the people of the workshop of the institute - mechanical, electrical and design & construction - for their help with various projects and problems.

Not forgotten are the people from the institute administration, who supported me in spending other people's money and filling out confusing forms.

My gratitude also belongs to the people who helped me in my time of sickness and pain.

To everyone who I've forgotten to mention in this text:
Sorry and feel free to consider yourself included.

Last I want to thank my family and friends for their unending support and love.

Erklärung:

Ich versichere, dass ich diese Arbeit selbstständig verfasst habe und keine anderen als die angegebenen Quellen und Hilfsmittel benutzt habe.

Heidelberg, den (Datum) .....